New Experimental Observables for the QCD Axion

by

Amalia Madden

A thesis
presented to the University of Waterloo
in fulfillment of the
thesis requirement for the degree of
Doctor of Philosophy
in
Physics

Waterloo, Ontario, Canada, 2024

© Amalia Madden 2024

Examining Committee Membership

The following served on the Examining Committee for this thesis. The decision of the Examining Committee is by majority vote.

External Examiner:	Anson Hook Professor, Dept. of Physics, University of Maryland
Supervisor(s):	Asimina Arvanitaki Professor, Perimeter Institute for Theoretical Physics Jaume Gomis Professor, Perimeter Institute for Theoretical Physics
Internal Member:	Brian McNamara Professor, Dept. of Physics, University of Waterloo
Internal-External Member:	Jonathan Baugh Professor, Dept. of Chemistry, University of Waterloo
Other Member(s):	Matthew Johnson Professor, Dept. of Physics, York University

Author's Declaration

This thesis consists of material all of which I authored or co-authored: see Statement of Contributions included in the thesis. This is a true copy of the thesis, including any required final revisions, as accepted by my examiners.

I understand that my thesis may be made electronically available to the public.

Statement of Contributions

The results in this thesis are from co-authored works towards which the author made a significant contribution.

Chapter 3 is based on the paper [1], co-authored with Asimina Arvanitaki and Ken Van Tilburg.

Chapter 4 is based on upcoming work with Asimina Arvanitaki, Jonathan Engel, Andrew Geraci, David Stilwell and Ken Van Tilburg.

Abstract

The QCD axion is one of the best motivated extensions to the Standard Model of particle physics that could also serve as the dark matter. The thesis will demonstrate new experimental observables that could be used to search for the axion. These observables are based on piezoelectric materials that spontaneously break parity symmetry, thereby enabling sensitivity to the axion's fundamental, model independent coupling to gluons.

The first observable explores how axion dark matter could generate an oscillating mechanical stress in a piezoelectric crystal. We call this new phenomenon "the piezoaxionic effect". When the frequency of axion DM matches the natural frequency of a bulk acoustic normal mode of the piezoelectric crystal, the piezoaxionic effect is resonantly enhanced and can be read out electrically via the piezoelectric effect. We also point out another, subdominant phenomenon present in all dielectrics, namely the "electroaxionic effect". An axion background can produce an electric displacement field in a crystal which in turn will give rise to a voltage across the crystal. We find that this model independent coupling of the QCD axion may be probed through the combination of the piezoaxionic and electroaxionic effects in piezoelectric crystals with aligned nuclear spins, with near-future experimental setups applicable for axion masses between 10^{-11}eV to 10^{-7}eV, a challenging range for most other detection concepts.

The second observable, the "piezoaxionic force" demonstrates how a piezoelectric crystal can be used to source virtual QCD axions in the laboratory, giving rise to a new axion-mediated force. The presence of parity violation in the piezoelectric crystal, combined with aligned nuclear spins, provides the necessary symmetry breaking to generate an effective in-medium scalar coupling of the axion to nucleons. We propose a detection scheme that uses the axion's model-dependent pseudoscalar coupling to nuclear spins, such that the new force can be detected by its effect on the precession of a sample of polarised nuclear spins. When the distance between the source crystal and the detector is modulated at the Larmor precession frequency of the nuclear spins, the signal is resonantly enhanced. We predict that near-future experimental setups should be sensitive to the axion in the unexplored mass range from 10^{-5}eV to 10^{-2}eV.

Acknowledgments

I am extremely grateful to my advisor Mina for providing me with the opportunity to tackle important questions about the universe every day, and for always pushing me to pursue the truth about nature even when the going gets extremely tough. It has been a privilege to learn from her exceptional intuition and broad knowledge of physics.

I would also like to extend a huge thank you to Ken Van Tilburg, who I consider my honorary co-advisor. Ken is an incredibly creative and insightful physicist, and his contributions were invaluable in producing the work in this thesis.

A special thank you to Junwu Huang, who has patiently listened to so many of my questions during my studies. Your knowledge and feedback have been a big part of my growth as a physicist. Thank you also to Matt Johnson and Jaume Gomis for their mentorship during my PhD.

I am very appreciative of all my wonderful collaborators: Davide Racco, Mario Reig, Jon Engel, Andy Geraci, Kendrick Smith and Selim Hotinli.

I am grateful for all of the people at PI who have been a part of my journey here: my PSI classmates who stayed on with me, Kasia, Aiden, Francisco, Sara and Ramiro, my officemates past and present: Finn, Taillte and Raquel, all of the bistro staff and my friends at the PI orchestra, especially Dan and Gang.

Finally, a big thank you to Alexandre for your unwavering support over these past five years. You have made my time at PI very special.

Table of Contents

Examining Committee Membership ii

Author's Declaration iii

Statement of Contributions iv

Abstract v

Acknowledgments vi

List of Figures x

List of Tables xii

1 Introduction 1

2 Axion Theory 8

2.1 The Strong CP Problem 8

2.1.1 The Axion Solution 9

2.2 Axion Dark Matter 11

2.2.1 The Misalignment Mechanism 12

2.3 Couplings of the Axion to the Standard Model 16

2.3.1 Axion-Gluon Coupling 16

2.3.2 Axion-Photon Coupling . . . 18
2.3.3 Axion-Fermion Couplings . . . 20

3 The Piezoaxionic Effect for Dark Matter 25
3.1 Theory . . . 28
3.1.1 Nucleus . . . 29
3.1.2 Atom . . . 35
3.1.3 Crystal . . . 38
3.2 Experiment . . . 42
3.2.1 Setup . . . 43
3.2.2 Signal . . . 47
3.2.3 Backgrounds . . . 53
3.2.4 Sensitivity . . . 59
3.3 Other Axion Couplings . . . 63
3.4 Discussion . . . 66

4 The Piezoaxionic Force 68
4.1 Theory . . . 69
4.2 Setup . . . 72
4.3 Sensitivity . . . 74
4.4 Systematics and Noise sources . . . 74
4.5 Conclusions . . . 80

5 Summary and Outlook 83

References 86

APPENDICES 104

A Appendices for the Piezoaxionic Effect **105**

A.1 Atomic Matrix Elements 105

A.2 Long-wavelength Reduction 107

A.3 Piezoelectric Equivalent Circuit Components 110

A.4 More Modes 111

B Appendices for the Piezoaxionic Force **117**

B.1 MQM and Rotational Invariance 117

B.2 Nuclear Spin Polarization Via Hyperfine Interactions 118

B.3 Magnetic Quadrupole Moment Matrix Elements 119

List of Figures

1.1 The QCD axion landscape 5
1.2 An example unit cell of a piezoelectric crystal 6

2.1 Basic setup of the CASPER experiment 17
2.2 Setup for the ARIADNE experiment 22

3.1 The relativistic enhancement factor as a function of proton number 37
3.2 A simplified illustration of the proposed experimental setup for the piezoaxionic effect. 43
3.3 Equivalent electric circuit of the experimental set-up for the piezoaxionic effect. 44
3.4 Axion induced voltage and crystal quality factor as a function of frequency. 50
3.5 Total impedance of input circuit as a function of frequency and circuit resonant frequency as a function of inductance and capacitance. 52
3.6 Amplitude spectral densities of all noise sources considered in the experimental setup 55
3.7 Sensitivity to an oscillatory theta angle $\bar{\theta}_a$ as a function of frequency for a single shot. 60
3.8 Axion parameter space probed by the setup described in Sec. 3.2. 61
3.9 Axion-electron coupling sensitivity 65

4.1 Experimental setup for the piezoaxionic force setup 75
4.2 Sensitivity to the gluon coupling for a monopole-dipole force generated by the nuclear Schiff moment. 76

4.3 Sensitivity to the gluon coupling for a monopole-dipole force generated by the nuclear magnetic quadrupole moment (MQM). 77
4.4 Sensitivity to the gluon coupling for a dipole-dipole force 78
4.5 Magnetic field norm along z-axis and y-axis of sample 82

List of Tables

3.1 List of primary symbols appearing in the four subsections 27
3.2 Candidate crystals categorized by their symmetry structure 45
3.3 Fiducial parameters for the idealized setup. 47

4.1 Estimated Schiff moments and MQMs of deformed (octupole or quadrupole) nuclei. 73

Chapter 1

Introduction

The Standard Model of particle physics (SM) is our most robust theory of the fundamental particles of nature and their interactions. It encompasses the strong, weak, and electromagnetic forces, with the latter two merged into the electroweak force. These forces are mediated by photons, W and Z bosons, and gluons. The SM matter content consists of quarks, which are charged under the strong force and combine to form composite particles like protons and neutrons, alongside leptons such as electrons and neutrinos. Finally, the SM is completed by the Higgs boson particle, discovered at the Large Hadron Collider (LHC) in 2012 [2, 3], which is responsible for endowing mass to the W and Z bosons, quarks and leptons. Precision tests of the SM such as the measurement of the anomalous magnetic dipole moment of the electron have been confirmed to a remarkable precision of 12 decimal places [4], heralding the SM as one of our most accurate theories of nature.

Despite these enormous achievements, the SM remains unable to provide solutions to several critical questions. These include the relatively "light" mass of the Higgs boson, despite its potential sensitivity to large corrections from unknown physics at higher energy scales (the hierarchy problem) [5, 6]; the origin of the asymmetry between matter and antimatter in the universe (baryogenesis) [7]; the source of the tiny masses of neutrinos [8]; an explanation for why we observe the three generations of quarks and leptons with varying masses and mixing patterns (the flavour problem) [9]; the elusive nature of dark energy [10, 11]; how we can integrate gravity on the same footing as the other fundamental forces; the unexpected absence of charge-parity symmetry violation in strong interactions (the strong CP problem) [12–15] and the nature of dark matter [16]. This thesis will explore how these last two issues may be interlinked through the hypothetical axion particle, and it will propose new experimental observables that could address them.

The Strong CP Problem concerns the non-violation of the combined charge conjugation (C) and parity reversal (P) symmetries by the strong force of the SM [17–19]. Here C symmetry signifies the invariance of the theory if we reverse the sign of the charges of particles, which switches particles and antiparticles, and P symmetry refers to invariance under a reversal of the sign of spatial coordinates from (x, y, z) to $(-x, -y, -z)$. If the strong force were to violate CP symmetry, this would naturally produce an experimentally measurable signature through the generation of an electric dipole moment (EDM) for the neutron. At present, no EDM for the neutron has been measured, setting extremely stringent constraints on the possibility of CP violation in this sector of the SM [20].

There are multiple reasons to be surprised by these observations. Violation of CP symmetry in the SM within the electroweak sector was verified over 60 years ago [21]. Thus, even if we set the QCD sector of the SM, which describes the strong force, to be invariant under CP, it does not enhance the overall symmetry of the SM. While the SM suffers from other "fine-tuning" problems, notably the hierarchy problem of the Higgs mass, the strong CP problem is more peculiar in that it does not have an anthropic solution [22]. In other words, it would be impossible for us to exist if the mass of the Higgs had a slightly different value, whereas it appears that our universe could accommodate a much larger CP violation within the QCD sector without altering its properties that are essential to our existence. The strong CP problem will be discussed more precisely in section 2.1.

The second issue tackled in this thesis is the nature of the DM, whose existence is supported by a wide range of extremely compelling evidence. Astrophysical studies have pointed to its existence since 1933 through galaxy rotation curves [23], with more recent research continuing to confirm this observation [24]. Gravitational lensing, the distortion of light due to distant galaxies' gravitational fields, provides further astrophysical evidence [25, 26]. Cosmological evidence, derived from observations of the cosmic microwave background (CMB) and combined with results from big bang nucleosynthesis (BBN), has solidified our current cosmological model of lambda cold dark matter (ΛCDM) [27]. This model precisely accounts for the abundances of the cosmological constant, dark and baryonic matter, indicating that 27% of the universe's energy density is comprised of cold, non-relativistic DM, which interacts extremely weakly with the ordinary baryonic matter of the SM. It is clear, however, that none of the particles within the SM can account for the DM. Neutrinos, our most weakly interacting particles, would be too hot in temperature and would therefore be in tension with our models for the formation of large-scale structure in the universe [28, 29]. Although alternative models posit that DM may not be a particle but rather a modification of gravity [30, 31], this explanation faces challenges in accurately describing observations of galaxy clusters [32].

It is thus clear that we must look beyond the SM to find a candidate particle for the

DM. Theoretical physicists have provided us with a plethora of models, but how do we determine which of these are the best motivated? A crucial model-building ingredient is that the DM candidate has a consistent cosmological history in which it is produced with the right temperature and the precise cosmological abundance that we observe in the universe today. Better yet, the particle could also solve additional problems in the SM. A highly motivated solution that ticks all of these boxes is the hypothetical axion particle [12–14]. The axion is a pseudoscalar particle proposed to provide a mechanism for solving the strong CP problem. The axion gains a potential from QCD processes such that when the axion is at the minimum of its potential, the strong CP problem is solved dynamically [33]. This mechanism is reviewed in greater detail in section 2.1.1. In addition, the presence of a large number of axion-like particles (ALPs) appears to be a generic prediction of string theory [34]. We will clarify now that this thesis will refer to the particle that solves the strong CP problem of QCD simply as an "axion" or sometimes the "QCD axion" for emphasis. While the QCD axion is the focus of this thesis, we will occasionally comment on other light, weakly interacting pseudoscalar particles that do not solve the strong CP problem; these are known as "ALPs".

The axion has a number of well-motivated cosmological production mechanisms that will be discussed in further detail in section 2.2.1, but we will introduce the most relevant here: the misalignment mechanism [35–37]. The framework of quantum field theory (QFT) tells us that particles are realised as excitations of an underlying quantum field. Early in the universe, when the temperature is higher than the QCD scale at which hadrons confine, the axion is massless. During this period, the axion field takes on a random initial value. As the universe expands and its temperature cools below the QCD confinement scale, the axion gains a mass. The equation of motion for the axion field becomes:

$$\ddot{a}(x) + 3H\dot{a}(x) + m_a^2(T)a(x) = 0. \tag{1.1}$$

where dots above terms indicate derivatives with respect to time, $a(x)$ is the axion field, $m_a(T)$ is its (temperature dependent) mass, and H_a is the Hubble parameter, which defines the expansion rate of the universe. This is the equation of a damped harmonic oscillator, where the friction term is set by the Hubble parameter. Initially, the system is overdamped, and the axion is frozen at its initial field value. As the universe continues to expand and cool and the size of the damping becomes less relevant, the axion rolls down towards the minimum of its potential. The oscillations of the axion field around the minimum of its potential correspond to a coherent state of cold, non-relativistic particles, with a final abundance that can vary depending on the initial value of the axion field – precisely what is needed for DM.

How can we search for the axion in the laboratory? To move forward, we must first

ask ourselves two more questions — what is the mass of the axion today and what sort of interactions does it have with the SM? It turns out that both of these questions are answered simultaneously by the theory of the axion. The axion's defining coupling is to the gluons of QCD, and the strength of this interaction, characterised by the so-called axion decay constant f_a, is inextricably linked to the axion's (low temperature) mass[1] [38]:

$$m_a = 5.691(51) \left(\frac{10^9 \text{GeV}}{f_a} \right) \text{meV} \tag{1.2}$$

The focus of the thesis will be on the development of new experimental observables that target this fundamental coupling of the axion to gluons. In addition to this coupling, however, is the possibility of model-dependent couplings to the other particles of the SM, in other words, couplings whose strengths are dependent on the specific way that we embed the axion in the SM. These topics are discussed in section 2.3, including examples of existing experimental directions that could probe a variety of couplings.

As can be seen from Eq. 1.2, axion theory does not provide us with a singular prediction for the mass of the axion, but rather a line in parameter space that could span many orders of magnitude. A guide to our current understanding of the potential parameter space where we can look for the axion is summarized in Figure 1.1. The possibility of an axion with a mass above 10^{-2}eV is constrained by astrophysical observations. If axions had such large couplings, their production rates in stars and supernovae would lead to faster cooling than our observations [39]. This limits the available parameter space of the axion to masses that are considered extremely light relative to many other well-motivated dark matter candidates such as weakly interacting massive particles (WIMPs), whose masses are typically in the GeV range. Such a vast difference in the mass regime points to a need for conceptually new experimental strategies to search for the axion. While the frontier of discovering new fundamental particles has historically required us to build colliders of increasing energy, discovering the axion will instead likely require low-energy, precision experiments.

When searching for light, bosonic DM such as the axion, we must also alter the way we picture DM interacting with our detectors. When considering models of fermionic dark matter, we are restricted to consider masses above 100eV. The origin of this bound is that fermions are restricted to a single particle per quantum state. Thus, within dense systems in our universe like dwarf galaxies, the occupation numbers of fermionic DM would become too high to allow for small particle masses [28]. Conversely, there is no

[1] Natural units, where $\hbar = c = k_B = 1$, will be used throughout this thesis. Here they are used to describe mass, so $1\,\text{eV} = 1.7 \times 10^{-36}$ kg.

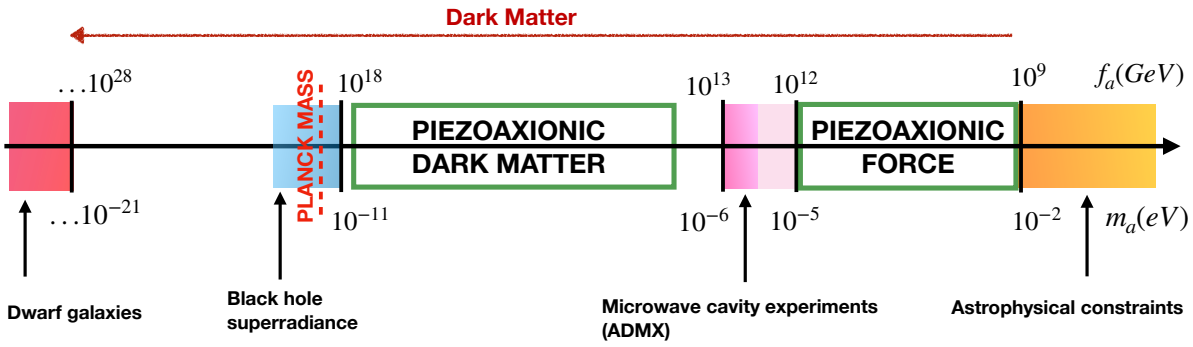

Figure 1.1: The QCD axion landscape: the shaded areas designate current and upcoming constraints on the axion, while the green outlined areas are the parts of parameter space that could potentially be probed with the new observables in this thesis. From right to left, the yellow shaded region is excluded by cooling of astrophysical objects [39], the dark pink is excluded by axion to photon conversion in the ADMX microwave cavity experiment [40] (the light pink is projected for upcoming ADMX runs), the blue region is excluded by black hole superradiance [34, 41], and the red region is excluded by kinematics of dwarf galaxies [42]. The limit where the axion decay constant f_a reaches the Planck scale is indicated, since a QCD axion with f_a above this scale is less well motivated.

such restriction on a bosonic DM particle. In fact, our choice of experimental techniques becomes motivated by such a transition into the low mass regime where we must consider high occupation numbers. Here it becomes more appropriate to think of bosonic DM as a coherent, oscillating classical field, whose frequency is set by the DM particle's mass, and its amplitude is determined by its density. This treatment stands in contrast to the more traditional picture of DM direct detection, where we might imagine looking for individual, heavy particles scattering off the atoms in our detectors.

The core idea behind the experimental observables of this thesis is that a common class of materials, piezoelectrics, provides the necessary symmetry structure to allow us to access a range of new physical observables for the axion's gluon coupling. A piezoelectric crystal is a type of crystal that can convert mechanical energy, in the form of stress or strain, into electrical energy, i.e., a potential difference across the crystal, and vice versa. The microscopic origin of this property arises from its point group symmetry. The symmetry groups of piezoelectric crystals are non-centrosymmetric, meaning that they lack a point in the unit cell which is invariant under a parity transformation: the transformation of a point (x, y, z) to the point $(-x, -y, -z)$, as can be seen in figure 1.2. Piezoelectricity turns

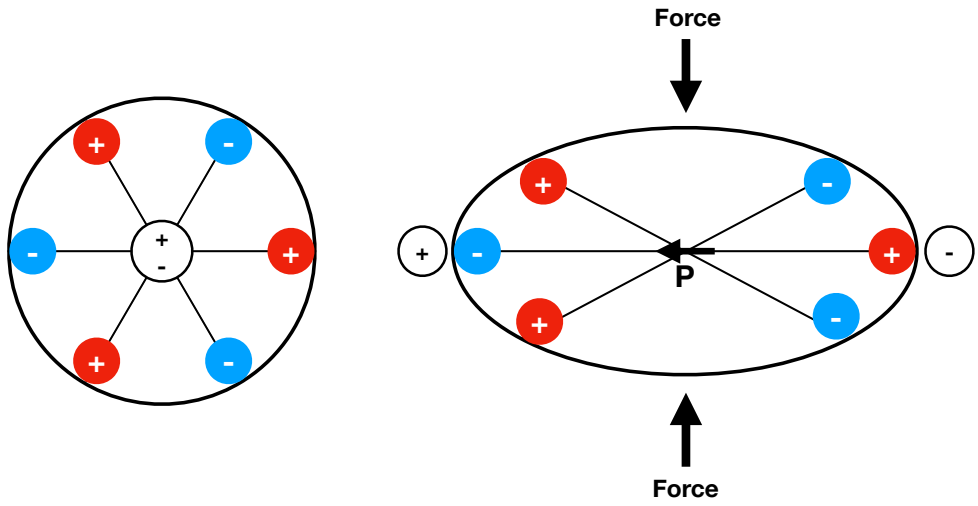

Figure 1.2: An example unit cell of a piezoelectric crystal. On the left hand side the unit cell does not have a dipole moment. Upon applying a stress to the unit cell, it is deformed to the shape on the right hand side, and the unit develops a polarization. This is a consequence of the lack of inversion symmetry at any point in the unit cell.

out to be a relatively common property of crystals; of the 32 possible crystal point groups, 20 of these are piezoelectric.

It is this lack of parity symmetry within the crystal that creates the possibility of probing new parity even observables for the axion, of which two possibilities will be explored in this thesis. The axion field itself is pseudoscalar and violates parity and time-reversal (T) symmetries (and thus by the CPT theorem, it also violates combined CP symmetry). One can then see that the combination of parity oddness from both the axion field and the piezoelectric crystal structure together allows us to access parity even observables. The remaining crucial ingredient is how to counteract the T symmetry violation of the axion field, which will be achieved by polarising the nuclear spins inside the crystal, thus providing an additional source of T-oddness.

The first of the new observables that we will explore in this thesis involves the generation of an oscillating mechanical strain in a piezoelectric crystal sourced by a background of axion dark matter. The target observable of a strain already has a well-studied history in precision searches for gravitational waves and scalar dark matter [43]. We coined this effect the "Piezoaxionic Effect". Much like the piezoelectric effect has a converse, we later

realised that in addition to being able to detect the axion particle, a piezoelectric crystal could also serve as a source of axions in the laboratory. This led to the second experimental observable demonstrated in this thesis: a search for a new force mediated by the axion and sourced by a piezoelectric crystal. This idea builds upon existing experimental searches for axion-like particles (ALPs) via their new forces such as the ARIADNE experiment [44]. While a search for a new force would not require the axion to also be the DM, it nevertheless probes a mass range where the axion could still potentially also serve as the DM.

The structure of this thesis will be as follows. In chapter 2, we will review the background theory and motivation for the axion, including the strong CP problem, production mechanisms for the axion, and different couplings to the SM. In chapter 3, we will discuss the piezoaxionic effect for dark matter detection, and in chapter 4, we will discuss the piezoaxionic force.

Chapter 2

Axion Theory

In this chapter, we will provide a brief overview of several key topics: the strong CP problem and the axion solution, the cosmological production of axion dark matter and its treatment in experiments, the various model-dependent and independent couplings of the axion, and a collection of existing experimental directions that can probe these couplings. The experiments mentioned represent only a small sample of the proposals found in recent publications. Some of the content in this chapter is drawn from the following reviews and textbooks:[45–49].

2.1 The Strong CP Problem

As suggested in the introduction of this thesis, we can add a new renormalizable term to the SM that is invariant under its gauge symmetries but also violates P and T symmetries (and hence also CP symmetry):

$$\Delta\mathcal{L}_0 = \frac{\alpha_s}{8\pi}\theta_0 G^a_{\mu\nu}\tilde{G}^{\mu\nu\,a} \tag{2.1}$$

$\alpha_s = \frac{g_s^2}{4\pi}$ is the $SU(3)_c$ gauge coupling, and $\tilde{G}^{\mu\nu\,a} = \frac{1}{2}\epsilon^{\mu\nu\lambda\rho}G^a_{\lambda\rho}$ (in Minkowski space). This term can also be written as a total divergence of a vector:

$$\Delta\mathcal{L}_0 = \frac{\alpha_s}{4\pi}\theta_0\partial_\mu K^\mu \tag{2.2}$$

$$K^\mu = \epsilon^{\mu\nu\lambda\rho}\cdot\left(G^a_\nu\partial_\lambda G^a_\rho + \frac{1}{3}f^{abc}G^a_\nu G^b_\lambda G^c_\rho\right) \tag{2.3}$$

Since this is a surface term it does not contribute to the classical equations of motion. Nevertheless, at the quantum level it can contribute non-perturbatively via instanton configurations.

Quantum effects also generate a contribution to the observable θ parameter of QCD through the quark mass terms:

$$\mathcal{L}_M = \bar{q}_L \hat{M}_q q_R + h.c. \tag{2.4}$$

where $q_{L/R}$ are the quark fields and M is their mass matrix. A chiral rotation of quark fields makes the masses real and therefore physical by removing any phases. However, through the axial anomaly, this redefinition generates a new term that is proportional to the same operator as Eq. 2.1:

$$\Delta\mathcal{L}_\theta = \frac{\alpha_s}{8\pi}\left(\theta_0 + \text{Arg}\left(\det(\hat{M}_q)\right)\right) G^a_{\mu\nu}\tilde{G}^{\mu\nu\,a} \equiv \frac{\alpha_s}{8\pi}\theta\, G^a_{\mu\nu}\tilde{G}^{\mu\nu\,a}. \tag{2.5}$$

θ now contains terms originating from two completely different sources of physics. The first is present even in the absence of quarks in the theory, whereas the second comes from the Yukawa couplings. There is thus no reason to assume that either is zero, or that they should cancel each other out.

The presence of a CP violating θ term generates a neutron electric dipole moment (EDM) d_n of the order [50]:

$$d_n \sim \theta \cdot 10^{-16}\, e\, cm. \tag{2.6}$$

This can be compared to experimental constraints, which find an upper bound on d_n of [20]:

$$d_n \lesssim 10^{-26}\, e\, cm. \tag{2.7}$$

These results tell us that θ must be incredibly small:

$$|\theta| < 10^{-10}. \tag{2.8}$$

This is the strong CP problem – the question of how two different sources of physics within the SM conspire to cancel to such high precision.

2.1.1 The Axion Solution

Suppose that we extend the SM with a new axial U(1) symmetry:

$$q_L \to e^{i\beta} q_L, \quad q_R \to e^{-i\beta} q_R. \tag{2.9}$$

This new $U(1)$ symmetry, known as Peccei-Quinn (PQ) symmetry, could rotate away θ [14]. PQ symmetry is explicitly broken by the Yukawa couplings of quarks to Higgs:

$$\mathcal{L}_Y = Y^d \bar{Q}\, H\, D_R + Y^u \bar{Q} i\sigma_2 H^* U_R. \tag{2.10}$$

where Y are the Yukawa couplings of the SM, Q, H, D and U are the SM fields, and σ denotes a Pauli matrix. PQ symmetry would be exact at the classical level if we could also perform the transformations $H \to i\beta H$ for first term, and $H \to -i\beta H$ for second term on the right hand side, which will motivate the UV completions considered later in this section. But even if PQ is an exact classical symmetry, there would still be the issue that PQ symmetry is spontaneously broken by quark masses. This spontaneous symmetry breaking leads to a massless Nambu-Goldstone-Boson, the axion, which transforms via a shift symmetry:

$$a(x) \to a(x) + \beta f_a. \tag{2.11}$$

Here f_a is a constant with dimension of mass known as the axion decay constant, and is related to the scale of PQ symmetry breaking. The axion enters the low energy Lagrangian as a phase in the quark mass matrix

$$\mathcal{L}_M = \bar{q}_R M_q e^{-2i\frac{a}{f_a}} q_L + h.c. \tag{2.12}$$

but like in Eq. 2.5, this phase can again be rotated into the θ term to arrive at:

$$\mathcal{L}_a = \frac{\alpha_s}{8\pi}\frac{a(x)}{f_a} G^a_{\mu\nu}\, \tilde{G}^{\mu\nu\, a}. \tag{2.13}$$

The overall effective theta parameter is then:

$$\bar{\theta}(x) = \theta + \frac{a(x)}{f_a} \tag{2.14}$$

We now see that quantum effects have explicitly broken PQ symmetry, so the axion must be a pseudo-Nambu-Goldstone boson.

Following the QCD phase transition when chiral symmetry is broken, non-perturbative effects generate a potential for the axion [38], given by:

$$V(a) = -m_\pi^2 f_\pi^2 \sqrt{1 - \frac{4 m_u m_d}{(m_u + m_d)^2} \sin^2\left(\frac{a(x)}{2f_a} + \frac{\theta}{2}\right)} \tag{2.15}$$

where $f_\pi \approx 130\text{MeV}$ is the pion decay constant. We see that the axion potential is periodic in 2π, and has a minimum at $\langle\bar{\theta}(x)\rangle = 0$, dynamically solving the strong CP problem. From the potential, the mass of the axion is found to be:

$$m_a^2 = \frac{m_u m_d}{(m_u + m_d)^2} \frac{m_\pi^2 f_\pi^2}{f_a^2}. \tag{2.16}$$

We will now very briefly describe the benchmark UV completions for implementing PQ symmetry with the SM:

- *PQWW*: Includes an additional Higgs doublet such that the transformation of the Higgs that preserves PQ symmetry suggested below eq. 2.10 becomes possible. The PQ breaking scale is then associated with the EW scale, and there is a prediction for a heavy axion with $m_a \sim 15\text{keV}$. This simple model has already been ruled out by experiment [12, 13].

- *DFSZ*: Includes a second Higgs doublet as before, but also an additional PQ charged complex scalar that is a singlet under the SM gauge group [15, 51] such that the axion is a linear combination of the phases of all three scalars in the theory. This raises the PQ symmetry breaking scale beyond experimentally constrained regions. This model also features couplings of the axion to both SM leptons and quarks.

- *KSVZ*: Includes a second Higgs doublet, a complex scalar and new heavy, quarks that are charged under PQ but neutral under electroweak symmetry. The axion is associated to the phase of the complex scalar [52, 53]. There are no tree level couplings of the axion to the SM quarks and leptons in this model.

A review of further possible models can be found in reference [54].

2.2 Axion Dark Matter

In the introduction of this thesis, we stated that axions with masses above 10^{-2} eV are constrained by stellar cooling (see figure 1.1). This constraint implies that axion dark matter must primarily consist of very light particles. When bosonic dark matter particles are light, it becomes more appropriate to treat them as a classical field. This rationale can be explained as follows: consider a cubic volume of dark matter, with dimensions set by the de Broglie wavelength of the axion, $\lambda_{DB} = \frac{1}{m_a v}$, where $v = 10^{-3}$ represents the

local velocity of dark matter. Using the fact that the energy density of dark matter in our galaxy is measured to be $0.4\,\mathrm{GeV\,cm^{-3}}$ [55, §27], we can estimate the number of particles within this volume as $N \sim 10^{24}\left(\frac{10^{-6}\text{ eV}}{m}\right)^4$. Quantum corrections to the classical picture should be significantly suppressed by factors of $\frac{1}{\sqrt{N}}$, making them negligible. This shift to the classical picture is appropriate when the occupation number of the axion particles is large, $N \gg 1$. In our galaxy, this transition occurs when $m_a \lesssim 1$ eV. We can write the classical axion dark matter field as [56]:

$$\bar{\theta}(t) \approx \bar{\theta}_0 \cos(m_a t) \tag{2.17}$$

$$\bar{\theta}_0 = \sqrt{\left\langle \bar{\theta}^2 \right\rangle} = \frac{\sqrt{2\rho_a}}{m_a f_a} \approx 4 \times 10^{-19} \sqrt{\frac{\rho_a}{\rho_{\mathrm{DM}}}} \tag{2.18}$$

where ρ_a is the axion density and ρ_{DM} is the dark matter density. The axion acts as a classical field up to its coherence time τ_{coh}, which is determined by the inverse kinetic energy spread of the axion DM:

$$\tau_{\mathrm{coh}} \simeq \frac{2\pi}{m_a} \frac{2}{v_0^2} \simeq \frac{1}{m_a} \left(4\pi \times 10^6\right). \tag{2.19}$$

.

In the following section we will review the cosmological production of axions. If axions were produced thermally like a WIMP, they would be relativistic and thus would be hot dark matter, which is excluded from accounting for the entirety of dark matter [57]. We will study an alternative mechanism that produces cold dark matter.

2.2.1 The Misalignment Mechanism

The classical equations of motion for an axion in an FRW spacetime are given by:

$$\ddot{a}(x) + 3H\dot{a}(x) - \frac{1}{R^2}\nabla^2 a(x) + \frac{\partial V(a,T)}{\partial a} = 0 \tag{2.20}$$

where dots denote time derivatives, R is the scale factor of the universe, $H = \dot{R}/R$ is the Hubble parameter, and spatial derivatives are taken with respect to comoving coordinates. For simplicity, we will ignore the periodic behaviour and take the small-angle limit, $\frac{\partial V(a,T)}{\partial a} \approx m_a(T)^2 a(x)$. The full potential is necessary in the case that the axion takes initial field values close to the top of its cosine-shaped potential, leading to interesting phenomenological signatures [58]. The author of this thesis wrote a paper on model-building for such a scenario in the early stages of their PhD, which can be found at [59].

Early in the universe when the $T > \Lambda_{QCD} \sim 200\text{MeV}$ and QCD is deconfined, the axion potential is negligible and the axion is massless. Each Hubble patch starts with a random initial misalignment angle for the axion field in the range $\bar{\theta}_i \in [0, 2\pi)$; since the potential is flat, all values are equally likely. After $T < \Lambda_{QCD}$, the axion gains a temperature dependent mass and the dynamics of the axion field begin to unfold [35]. There are two distinct possibilities for the subsequent evolution of the axion field depending on whether or not PQ symmetry is broken after inflation. We will focus on the case of PQ symmetry broken before or during inflation, and is not subsequently restored after inflation.

PQ symmetry not restored after inflation

Inflation stretches all Hubble patches and establishes homogeneous initial conditions, ensuring that the axion's initial misalignment angle is uniform everywhere post-inflation. Consequently, we can disregard the gradient term in Eq. 2.20, and the equation of motion becomes:

$$\ddot{a} + 3H\dot{a} + m_a^2(T)a = 0 \tag{2.21}$$

We will assume that the following dynamics occur during the radiation domination epoch of the universe, as the axion should act as dark matter before matter-radiation equality.

We can solve the equation of motion using the WKB approximation: we assume the solution is composed of a slowly varying amplitude and a quickly varying phase:

$$a(t) = A(t)e^{i\phi(t)}. \tag{2.22}$$

Plugging this into the equation of motion, we find separate equations for the real and complex parts:

$$\frac{\ddot{A}}{A} - \dot{\phi}^2 + 3H\frac{\dot{A}}{A} + m_a(T)^2 = 0 \tag{2.23}$$

$$2\dot{A} + A\frac{\ddot{\phi}}{\dot{\phi}} + 3AH = 0 \tag{2.24}$$

Since we expect the fast frequency scale of the phase to be of order m_a, we neglect the terms

$$\frac{\ddot{A}}{A}, H\frac{\dot{A}}{A} \quad \ll \quad \dot{\phi}^2, m_a^2$$

From Eq. 2.23, we then find the result:

$$\dot{\phi}^2 = m_a^2 \tag{2.25}$$

$$\phi(t) = \int dt' m_a(t') + \text{const.} \tag{2.26}$$

Putting this into 2.24 gives us:

$$\dot{A} - \frac{A}{2}\left(3H + \frac{\dot{m}_a}{m_a}\right) = 0 \tag{2.27}$$

This equation takes a solution of the following form:

$$A(t) = \frac{C}{R^{3/2} m_a(t)^{1/2}} \tag{2.28}$$

Now taking the real part of Eq. 2.22, we find:

$$a(t) = \frac{C}{R^{3/2}\, m_a(t)^{1/2}} \cos \int_{t_0} dt' m_a(t'). \tag{2.29}$$

We can now examine this solution in two limiting regimes. When $H > m_a(T)$, the axion is overdamped and frozen at its initial misalignment angle. We find the energy density in the axion field to be:

$$\rho_a = \frac{1}{2} f_a^2 m_a^2(t) \theta_i^2. \tag{2.30}$$

In the opposite limit as $H < m_a(T)$, the axion begins to oscillate around the minimum of its potential, and the energy density scales as:

$$\langle \rho_a(t) \rangle = \frac{C^2}{2m_a(t)} \frac{f_a^2 m_a^2(t)}{R^3} \tag{2.31}$$

where the averaging is over fast oscillations. Patching these two solutions together at the crossover point when the axion begins to oscillate ($H \sim m_a(T)$), one finds:

$$C^2 = m_a(T_{osc}) R^3(T_{osc}) \theta_i^2. \tag{2.32}$$

This can now be used to find the energy density at later times by including how it dilutes with expansion:

$$\rho_a(T) \simeq \frac{1}{2} f_a^2 m_a(T_{osc}) m_a(T) \left(\frac{R(T_{osc})}{R(T)}\right)^3 \theta_i^2 \tag{2.33}$$

$$\left(\frac{R(T_{osc})}{R(T_0)}\right)^3 = \left(\frac{g_{*s}(T)}{g_{*s}(T_{osc})}\right)\left(\frac{T_0}{T_{osc}}\right)^3 \tag{2.34}$$

where g_* is the effective number of degrees of freedom in entropy. The final ingredient is to understand how the axions mass depends on temperature. The classic result from the

dilute instanton gas approximation (DIGA) gives a power law dependence of the axion mass on temperature, with an approximate form [46, 60]:

$$m_a(T)^2 \sim \frac{m_u m_d m_s}{f_a^2} \frac{\Lambda_{QCD}^9}{T^8} \tag{2.35}$$

If we say that at the present day the axion mass is given by its zero-temperature value, $m_a(T) = m_a$, where m_a is given by Eq. 1.2, we find:

$$\Omega_a = \frac{\rho_a}{\rho_{\text{crit}}} \approx 0.25\, \theta_i^2 \left(\frac{f_a}{5 \times 10^{12} \text{GeV}} \right)^{1.2} \tag{2.36}$$

where Ω_a is the dimensionless energy density today, and ρ_{crit} is the critical energy density of the universe. We see that the abundance of QCD axion dark matter today is a function of the axion's initial misalignment angle and its decay constant f_a.

If we want $f_a \sim$ GUT scale, which is relevant for the dark matter parameter space featured in chapter 3 of this thesis, we would need $\theta_i \sim 10^{-5}$. There are two possible scenarios to mitigate this fine tuning:

- *Entropy Dilution*: this could originate from a period of early matter domination. Additional entropy from the reheating process would dilute the axion DM abundance [37, 61].
- *Anthropics*: different patches of the universe have different initial misalignment angles. Since inflation causes exponential expansion, we are no longer in causal contact with these other patches. Different patches may have different DM densities, but perhaps our patch is necessary for the existence of life [62].

PQ symmetry restored after inflation

In this scenario, different Hubble patches in the universe have different values of the initial misalignment angle θ_i. We can calculate the contribution to the axion abundance from misalignment, as in the previous scenario, by considering the average angle, $\langle \theta_i \rangle \sim \pi/\sqrt{3}$. If this were the sole contribution to the abundance, it would yield an extremely predictive result, with the axion mass being approximately 30μeV [63].

However, the PQ phase transition also results in the formation of topological defects such as axion walls and strings [64]. In the previous scenario, these were diluted away by inflation, but when they are not, their decay results in an additional population of

non-relativistic axions. Determining this contribution requires complex simulations and detailed computations, and there are still significant uncertainties with a wide range of results, ranging from a contribution comparable to that from misalignment to several orders of magnitude larger. For a more detailed understanding of this topic, see references [48, 63, 65].

2.3 Couplings of the Axion to the Standard Model

2.3.1 Axion-Gluon Coupling

While the defining coupling of the axion is to gluons, there are as yet no laboratory experiments capable of reaching QCD axion dark matter parameter space via this interaction [66]. It is also the subject of fewer proposed experiments relative to more model dependent couplings such as the photon coupling, which will be discussed later in this chapter.

A key existing experimental direction for this coupling is provided by the CASPER experiment, which will be outlined here. Axion dark matter produces an oscillating neutron electric dipole moment [50, 67]:

$$d_n(t) \approx 10^{-3}\,\overline{\theta}(t)\,\mathrm{e\ fm}. \tag{2.37}$$

which a frequency set by the axion mass. The interaction of this dipole moment in an electric field is given by:

$$H_{EDM} = -\mathbf{d}_n(t) \cdot \mathbf{E} \tag{2.38}$$

and a corresponding torque:

$$\tau_{EDM} = \mathbf{d}_n(t) \times \mathbf{E}. \tag{2.39}$$

The idea of the CASPER experiment is to use a material with a strong internal electric field, which can be found in ferroelectric type materials, and to polarize the nuclear spins in the material using an external magnetic field (see figure 2.1). The presence of axion dark matter will cause the spins inside the crystal to precess off axis, leading to a new source of magnetization within the crystal. When the natural frequency of the spins, the Larmor frequency, matches the axion's frequency, this magnetization is resonantly enhanced. The Larmor frequency of the spins is given by:

$$\omega_L = \gamma_n B_0 \tag{2.40}$$

where γ_n is the nuclear gyromagnetic ratio. The subsequent magnetization on resonance, $\omega_L \approx m_a$, scales as:

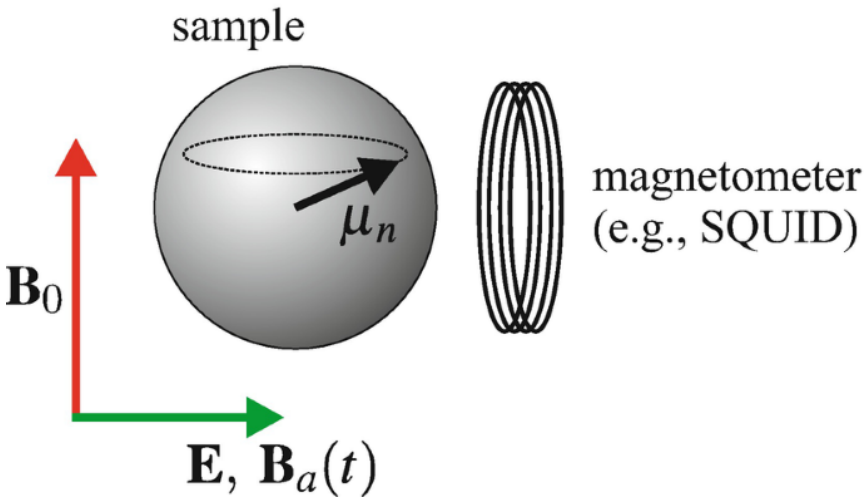

Figure 2.1: Basic setup of the CASPER experiment. A nuclear spin with magnetic moment μ_n is polarized in a constant external magnetic field B_0. The internal electric field of a material E that contains the spin, together with an axion induced EDM d_n, produce a torque on the magnetic moment. The new component of axion-induced magnetization can be read out using a SQUID. Figure taken from [68].

$$M \approx n_S p \mu_n d_n E\, T_2 \tag{2.41}$$

where n_S is the number density of spins in the material, p is their polarization, T_2 is the transverse coherence time of the nuclear spins and $\mu_n = \frac{e}{2m_p}$ is the nuclear magneton. The transverse coherence time T_2 corresponds to the timescale over which the spins contributing to the magnetization will dephase, and is a material dependent property. Increasing T_2 is one of the major technological challenges towards such a setup reaching QCD axion sensitivity.

Given the the largest possible laboratory B-fields are around $\sim 30T$, this corresponds to an upper limit on the axion mass that can be probed by this type of experiment of $m_a \sim 10^{-6}$eV. This falls within the optimal sensitivity of a SQUID magnetometer (superconducting quantum interference device) [69], around 10 Hz - 10^6 Hz. At the lower frequency end of this range, around kHz frequencies and below, the axion is already constrained by black hole superradiance [41] as can be seen in figure 1.1.

Finally, it should be noted that the mass-coupling relation of the QCD axion in Eq. 1.2, which is determined by the axion's gluon coupling, can be broken in principle. In practice, a modification to lower the $m_a f_a$ product of the QCD axion, which would increase the

effective theta angle amplitude in Eq. 2.1, requires a fine tuning of both the first and second derivatives of the potential, to preserve the Peccei-Quinn solution to the strong CP problem and to partially cancel the QCD contributions to the axion mass, respectively. Even with significant model-building efforts, this part of parameter space is precarious, as finite-density and finite-temperature effects can undo the fine tuning in the vacuum, leading to wildly different in-medium minima in stellar systems [70]. A significant increase in the $m_a f_a$ product is generically only fine-tuned in the first derivative of the potential, but would lower the rms $\overline{\theta}_a$ angle and thus would be much harder to detect.

2.3.2 Axion-Photon Coupling

The axion photon coupling is defined as [38]

$$\mathcal{L} \supset \frac{1}{4} g_{a\gamma\gamma} a(x) F_{\mu\nu} \tilde{F}^{\mu\nu} = \frac{1}{4} g_{a\gamma\gamma} a(x) \mathbf{E} \cdot \mathbf{B} \tag{2.42}$$

$$g_{a\gamma\gamma} = \frac{\alpha_{EM}}{2\pi f_a} \left[\frac{E}{N} - \frac{2}{3} \frac{4m_d + m_u}{m_d + m_u} \right] \tag{2.43}$$

The first term on the right hand side of Eq. 2.43 is a model dependent contribution, where E is the electromagnetic anomaly of the axial current associated with the axion and N is the colour anomaly. For DFSZ axions, $E/N = 8/3$, whereas for KSVZ, $E/N = 0$. The second term is a model-independent contribution that derives from the fundamental coupling of the axion to gluons of Eq. 2.13 via a quark field redefinition. More precisely, to arrive at Eq. 2.43 the quark fields are redefined as:

$$q = \begin{pmatrix} u \\ d \end{pmatrix} \to e^{i\gamma_5 \frac{a}{2f_a} Q_a} \begin{pmatrix} u \\ d \end{pmatrix}, \quad Q_a = \frac{M_q^{-1}}{\langle M_q^{-1} \rangle} \tag{2.44}$$

Depending on the UV completion of the axion, given the opposite signs of the two contributions it is possible that they could conspire to produce a small coupling. The two benchmark models above, however, are already within the reach of microwave cavity haloscope experiments within a small mass window.

Haloscopes

A starting point for considering experimental probes of the axion-photon coupling is the modification of two of Maxwell's equations:

$$\boldsymbol{\nabla} \cdot \mathbf{E} = \rho - g_{a\gamma\gamma} \mathbf{B} \cdot \boldsymbol{\nabla} a \tag{2.45}$$

$$\nabla \times \mathbf{B} = \frac{\partial \mathbf{E}}{\partial t} + \mathbf{J} - g_{a\gamma\gamma} \left(\mathbf{E} \times \boldsymbol{\nabla} a - \frac{\partial a}{\partial t} \mathbf{B} \right). \tag{2.46}$$

Axion haloscopes are designed to detect axion dark matter through its conversion to photons in a strong magnetic field, the prototype being the ADMX experiment [40, 71]. They use a cylindrical electromagnetic cavity with a very high quality factor ($Q_c \sim 10^5$), permeated by a static, homogeneous magnetic field B_0. If the de Broglie wavelength of the axion is large compared to the size of the cavity, we can neglect the spatial derivatives of the axion in the modified Maxwell equations when solving for the cavity modes. The power on resonance ($\omega_{nl} = m_a$) for a given cavity mode is found to be:

$$P = g_{a\gamma\gamma}^2 V B_0^2 \rho_a C \frac{1}{m_a} \min(Q_c, Q_a) \tag{2.47}$$

where V is the volume of the cavity, ρ_a is the local energy density of dark matter, Q_c is the quality factor of the cavity, and C is a geometric form factor for the cavity that takes into account the overlap between the penetrating magnetic field B_0 and the cavity electric field, given by:

$$C = \frac{|\int_V d^3x \mathbf{E} \cdot \mathbf{B}_0|^2}{\mathbf{B}_0^2 V \int_V d^3x \epsilon |\mathbf{E}|^2}. \tag{2.48}$$

where $\mathbf{E}$ is the electric field of the relevant cavity mode, and ϵ is the dielectric constant. The largest form factor is $C = 0.69$ for the TM_{010} mode.

The cavity is tuned by moving a dielectric rod or metal post inside in order to change the fundamental frequency. Since the axion has a very large open parameter space, a key measure of the effectiveness of such an experiment is the frequency scanning rate. For the ADMX experiment, the scanning rate scales as:

$$\begin{aligned} \frac{df}{dt} = \frac{12\,\mathrm{GHz}}{\mathrm{year}} \left(\frac{4}{\mathrm{SNR}} \right)^2 \left(\frac{V}{500\,L} \right)^2 \left(\frac{B_0}{7\,T} \right)^2 C^2 \\ \times \left(\frac{g_{a\gamma\gamma}}{0.72} \right)^4 \left(\frac{\rho_a}{0.3\mathrm{GeV\ cm}^{-3}} \right) \left(\frac{3K}{T_n} \right)^2 \left(\frac{f}{\mathrm{GHz}} \right)^2 \frac{Q_L}{Q_a} \end{aligned} \tag{2.49}$$

where T_n is the sum of the physical temperature of the cavity plus the noise temperature of the microwave receiver that detects the photons from axion-to-photon conversion [72]. The haloscope is sensitive to axions with Compton wavelengths roughly comparable to the cavity size. The ADMX experiment has already begun to probe the QCD axion mass window between 10^{-6}eV and 10^{-5}eV.

2.3.3 Axion-Fermion Couplings

The most generic couplings of the axion to fermions can be written as:

$$\mathcal{L}_{aff} = -g_s^f a\bar{\psi}_f\psi_f + \frac{g_p^f}{2m_f}\partial_\mu a\bar{\psi}_f\gamma^\mu\gamma_5\psi_f \tag{2.50}$$

where the first term is a scalar coupling of the axion, and the second is a pseudoscalar coupling. The scalar coupling g_s^f requires an extra source of P and T violation in addition to the axion in order to be generated. This could be supplied by the CP violation already present in the SM through the CKM matrix, however, this is usually small – we will review this case below for nuclear couplings. In the non-relativistic limit, the second term on the right hand side becomes

$$\frac{g_p^f}{2m_f}\boldsymbol{\sigma}\cdot\left[\boldsymbol{\nabla}a + \dot{a}\frac{\mathbf{p}_f}{m_f}\right] \tag{2.51}$$

Nucleon Couplings

The couplings for nuclei are model dependent but do contain an irreducible contribution derived from the axion gluon interaction of Eq. 2.1. For the scalar nucleon coupling, we have [73]:

$$g_s^N \sim 10^{-30}\frac{10^9 GeV}{f_a}. \tag{2.52}$$

where the additional parity violation required has been sourced by the electroweak sector of the SM. Bigger couplings are possible if considering an ALP or additional BSM fields up to $g_s^N \sim 10^{-21}\,(10^9\text{GeV}/f_a)$, where the upper bound is set by constraints from EDM searches [74]. For the pseudoscalar coupling, there is an irreducible contribution from the gluon coupling in addition to model dependent contributions, characterised by the coefficient C_N:

$$g_p^N \equiv \frac{C_N m_N}{f_a} \simeq C_N \times 10^{-9}\,\frac{10^9 GeV}{f_a} \tag{2.53}$$

In the KSVZ model, there are no model dependent contributions and we only have the irreducible coefficients from QCD:

$$C_p \approx 0.47(3), \quad C_n \approx 0.02(3) \tag{2.54}$$

whereas in the DFSZ model,

$$C_p \approx -0.182 + 0.435 \sin^2\beta \pm 0.025 \tag{2.55}$$

$$C_n \approx 0.160 - 0.414 \sin^2\beta \pm 0.025 \tag{2.56}$$

where $\tan\beta = v_u/v_d$ is the ratio of the VEVs of the two Higgs doublets in the SM. From unitarity arguments, $\tan\beta \in [0.28, 140]$ [63].

Electron Couplings

The axion coupling to fermions does not have a model independent coupling directly derived from the gluon coupling, with the exception of very small radiative corrections via the photon/meson couplings. There can be tree level pseudoscalar couplings depending on the UV completion of the axion:

$$g_p^e \equiv \frac{C_e m_e}{f_a} \tag{2.57}$$

$$C_e = \sin^2\beta/3 \quad \text{(DFSZ)} \tag{2.58}$$

$$C_e = 0 \quad \text{(KSVZ)} \tag{2.59}$$

since only the DFSZ model features couplings of the axion to leptons [63].

New macroscopic forces

The fermion couplings above can be used to generate macroscopic forces that are mediated by the axion [76], with three possibilities depending on the combination of scalar (monopole) and pseudoscalar (dipole) couplings:

$$U_{ss}(r) = \frac{g_s^1 g_s^2\, e^{-m_a r}}{4\pi\, r} \tag{2.60}$$

$$U_{sp}(r) = \frac{g_s^1 g_p^2}{8\pi\, m_{f_2}} \left(\frac{m_a}{r} + \frac{1}{r^2}\right) e^{-m_a r} (\hat{\boldsymbol{\sigma}}_2 \cdot \hat{\mathbf{r}}) \tag{2.61}$$

$$U_{pp}(r) = \frac{g_p^1 g_p^2}{16\pi\, m_{f_1} m_{f_2}} \left((\hat{\boldsymbol{\sigma}}_1 \cdot \hat{\boldsymbol{\sigma}}_2) \left(\frac{m_a}{r^2} + \frac{1}{r^3}\right) - (\hat{\boldsymbol{\sigma}}_1 \cdot \hat{\boldsymbol{r}})(\hat{\boldsymbol{\sigma}}_2 \cdot \hat{\boldsymbol{r}}) \left(\frac{m_a^2}{r} + \frac{3m_a}{r^2} + \frac{3}{r^3}\right) \right) e^{-m_a r} \tag{2.62}$$

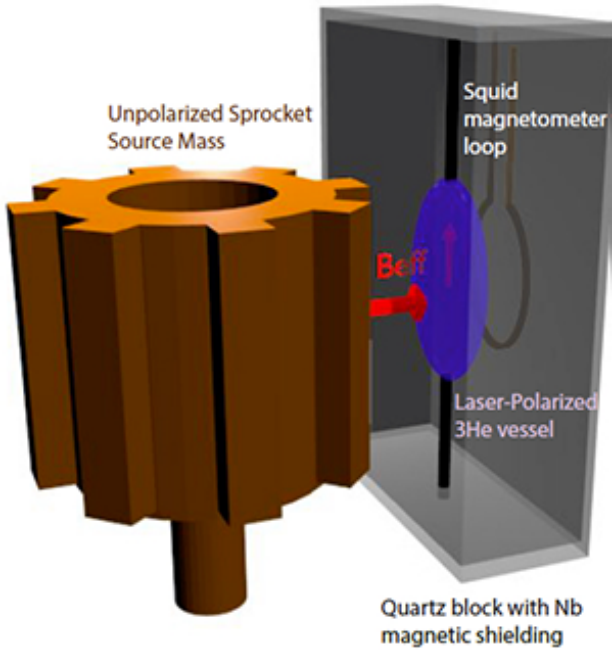

Figure 2.2: Setup for the ARIADNE experiment. A dense mass sources an effective axion-induced magnetic field, which unlike a real magnetic field, can penetrate the magnetic shielding containing the detection sample. Spin-polarized ^{3}He is used to detect the axion magnetic field, by looking for a new, anomalous component of its magnetization. When the segmented source mass is rotated to match the Larmor frequency of the spins, the signal is resonantly enhanced. Figure taken from [75].

The first of these, the monopole-monopole force, is often searched for as a correction to Newton's inverse square law [77]. The second two forces will be explored as a probe of the axion in chapter 4 of this thesis, building upon an existing experimental proposal for detecting monopole-dipole forces mediated by an ALP known as ARIADNE [44, 75, 78], which will be described in this section.

The starting point is that the monopole-dipole force can also be expressed as an "ef-

fective" magnetic field

$$U_{sp} = \boldsymbol{B}_{\text{eff}} \cdot \hat{\boldsymbol{\sigma}}_2 \tag{2.63}$$

$$B_{\text{eff}} = \frac{2}{\gamma_f} \frac{g_s^1 g_p^2}{8\pi m_f} \left(\frac{m_a}{r} + \frac{1}{r^2} \right) e^{-m_a r} \hat{\boldsymbol{r}} \tag{2.64}$$

where γ_f is the fermion gyromagnetic ratio. The ARIADNE experiment uses a dense mass to source an effective axion-induced magnetic field that is directed perpendicular to the polarization direction of a sample of spin polarized ^{3}He (figure 2.2). Magnetic shielding around the ^{3}He blocks real magnetic fields so that only the axion magnetic field can reach the sample. The source mass is made up of n segments and is rotated at a fixed frequency, such that the axion magnetic field takes on the frequency $\omega = n\omega_{\text{rot}}$. This frequency is matched to the Larmor frequency of a sample of polarised nuclear spins, $\omega_L = 2\mu_n B_{\text{ext}}$, so that the signal is resonantly enhanced. In this way, the helium spins are acting as an amplifier and transducer of the axion magnetic field, turning it into a larger, real magnetic field. This leads to an anomalous magnetisation of the sample that scales as:

$$M(t) \approx \frac{n_s}{2} p \, \mu_n \, \gamma_N \, B_{\text{eff}} \, t \cos(\omega t) \tag{2.65}$$

where n_s is the polarized spin density in the material, p is the polarization fraction and μ_n is the nuclear magnetic moment. The magnetization grows linearly until $t \sim T_2$, the transverse coherence time of the nuclear spins. This anomalous magnetization can be picked up by a SQUID magnetometer. The axion mass range that can be probed by this experiment is determined by the separation of the source mass and spin sample in the experiment, since the force is finite range, and peaks when the axion's Compton wavelength is comparable to the separation. The current design scans the mass range between 10^{-5}eV to 10^{-2}eV, corresponding to forces of range 1cm to 0.001cm. The main noise source in the experiment derives from spin decoherence in the ^{3}He sample, and sets the minimum magnetic field that the setup is sensitive to:

$$\begin{aligned} B_{\text{min}} &\approx p^{-1} \sqrt{\frac{2b}{n_s \mu_{^3\text{He}} \gamma V T_2}} \\ &= 3 \times 10^{-19} \text{ T} \times \left(\frac{1}{p} \right) \sqrt{\left(\frac{b}{1 \text{ Hz}} \right) \left(\frac{1 \text{ mm}^3}{V} \right) \left(\frac{10^{21} \text{ cm}^{-3}}{n_s} \right) \left(\frac{1000 \text{ s}}{T_2} \right)}. \end{aligned} \tag{2.66}$$

where b is the bandwidth and V is the volume of ^{3}He. The current forecasts for the ARIADNE experiment suggest sensitivity to new ALP parameter space. Reaching the

QCD axion, however, is challenging since the irreducible contribution of the QCD axion to the scalar coupling of Eq. 2.50 without additional CP violating BSM fields is very small, as can be seen in Eq. 2.52. The results of chapter 4 will address how we can hope to reach the QCD axion via a new effective coupling present within piezoelectric crystals.

Chapter 3

The Piezoaxionic Effect for Dark Matter

When axions make up (all or a component of) the DM of our Universe, they manifest as a background that violates parity (P) and time reversal (T) invariance. In this chapter, we show how a P-violating axion DM background produces a stress in piezoelectric crystals, a new observable that we call the *piezoaxionic effect*. Piezoelectric crystal structures break parity, by definition. Therefore, no symmetry forbids the occurrence of stress (even under P and T) upon application of an electric field (odd under P and even under T)—the converse piezoelectric effect [79, 80]. Vice versa, an electric field results from an applied stress—the piezoelectric effect [81, 82]. For such a material, a stress can appear across the crystal in an axion DM background, by analogy to the (converse) piezoelectric effect. For the axion coupling to anomaly of the strong interactions, which violates simultaneously P and T, a piezoelectric crystal with polarized nuclear spins is needed for the stress to appear. When the oscillation frequency of the axion DM wave matches an acoustic resonance frequency of the crystal, the axion-induced stress results in a resonantly enhanced strain.

Such strain, or simply put, a change in the length of a crystal, is an observable that has been used for decades in the context of resonant-mass gravitational wave detectors [83–85]. Resonant-mass GW detectors measure *absolute* changes in length much more more precisely than LIGO [86]. A subset of the authors in this paper has shown in the past that such sensitivity can be used to probe scalar DM [87]. The AURIGA collaboration implemented this idea and used their existing data to place the most stringent constraints thus far on (P- and T-even) scalar DM that couples to the electron and/or the photon [88], showing sensitivity to strains as small as 10^{-25}, provided the signal has a sufficiently long coherence time.

We expand on these ideas and demonstrate how a resonant-mass detector made from a piezoelectric crystal can be used to detect QCD axion DM with masses between $10^{-11}\,\text{eV}$ and $10^{-7}\,\text{eV}$. While several axion couplings may produce a signal in our setup, the most promising one at low frequencies is the irreducible coupling of the QCD axion to gluons.

There is one more observable associated with the P- and T-violating nature of an axion background. Aligned nuclear spins in any dielectric material, bathed in QCD axion DM, source electric displacements [89], that produce an oscillating voltage difference across two opposing surfaces of the material. We call this phenomenon the *electroaxionic effect*. As we will see, this effect does not benefit from the same enhancement through mechanical resonance as the piezoaxionic effect, but nevertheless contributes to the axion signal when using an electrical readout. A similar electroaxionic effect is also present for derivative couplings of axion-like particles.

The observables discussed in this paper differ significantly from solid-state EDM experiments [90–94] as well as nuclear-magnetic-resonance-based techniques for QCD axion DM detection [95], since they do not require the application of an electric field to be effective or the use of ferroelectric materials. Furthermore, both of these types of experiments rely on detecting a change in the magnetization of the sample due to a reversal of the electric field (solid-state EDM experiments) or due to the precession of the spins in the axion background. The piezoaxionic and electroaxionic effects produce an oscillatory signal without any change in the direction of the aligned spins.

Our paper is structured as follows. In Sec. 3.1, we calculate the piezoaxionic and the electroaxionic tensors in piezoelectric crystals, focusing on the axion coupling to the QCD anomaly. In Sec. 3.2, we describe the experimental setup, delineate the signal, discuss noise sources and possible backgrounds, and present our forecast for the reach to axion parameter space. Finally, we present estimates for other couplings in Sec. 3.3 and discuss our assumptions and future directions in Sec. 3.4. We use natural units wherein $\hbar = c = k_B = 1$. For the convenience of the reader, Tab. 3.1 summarizes the main symbols used in this chapter.

Table 3.1: List of primary symbols appearing in the four subsections of both Secs. 3.1 and 3.2, their transformations (even = +, odd = −) under parity P and time-reversal T (where relevant), and the subsections where they first appear.

Quantity	Symbol	P	T	Subsection
Axion mass, decay constant	m_a, f_a			2
Axion frequency	f			
Axion coherence time	$\tau_{\rm coh}$			
Effective theta angle (with axion)	$\overline{\theta}_a$	−	−	
Schiff moment (magnitude)	S	−	−	3.1.1
Schiff moment	$\mathbf{S}$	−	+	
Nuclear spin	I_α	+	−	
Atomic charge, number	Z, A			3.1.2
Atomic matrix element	$\mathcal{M}_\alpha$	−	+	
Relativistic enhancement factor	$\mathcal{R}$			
Wavefunction $\lvert s\rangle, \lvert p_j\rangle$ coefficients	$\epsilon_s, \epsilon_{p_j}$			
Effective quantum numbers	ν_s, ν_{p_j}			
Mass density (crystal)	ρ			3.1.3
Heavy-nucleon number density	n_N			
Volume of unit cell	V_c			
Potential energy density (crystal)	U			
Strain	$S_{\alpha\beta}$	+	+	
Stress	$T_{\alpha\beta}$	+	+	
Electric field	E_α	−	+	
Electric displacement	D_α	−	+	
Elastic stiffness (at constant D)	$c^D_{\alpha\beta,\gamma\delta}$	+	+	
Impermittivity (at constant S)	$\beta^S_{\alpha\beta}$	+	+	
Piezoelectric tensor	$h_{\alpha,\gamma\delta}$	−	+	
Piezoaxionic tensor	$\xi_{\alpha,\gamma\delta}$	−	+	
Electroaxionic polarizability	$\zeta_{\alpha\beta}$	+	+	
Impedance of circuit element X	Z_X			3.2.1
Inductance	L_X			
Capacitance	C_X			
Resistance	R_X			
Mutual inductance, coupling	M_X, k_X			

Table 3.1 (continued)

Quantity	Symbol	P	T	Subsection
Crystal length in direction i	ℓ_i			
Mechanical resonance frequency	f_0			
Natural resonance frequency	f_{nat}			
Mechanical displacement	u_i			
Sound speed (longitudinal)	v^D			3.2.2
Electromechanical coupling	k			
Quality factor	$Q(\omega)$			
Axion-induced voltage, current	V_a, I_a			
SQUID flux	Φ_{SQ}			
Noise spectral density (voltage)	S_V			
Loss angle of X	δ_X			
Temperature	T			3.2.3
SQUID noise parameter	η_{SQ}			
Cooling power, decay heat	$\dot{Q}$			
Signal-to-noise ratio	SNR			
Resonance frequency (circuit)	f_{res}			3.2.4
Shot time	t_{shot}			
Total integration time	t_{int}			

3.1 Theory

In this section, which is split into three parts, we work out the theory of the piezoaxionic and electroaxionic effects. In section 3.1.1 reviews the generation of P- and T-violating electromagnetic moments of nuclei due to this coupling, in particular the Schiff moment. Section 3.1.2 explains how a Schiff moment leads to energy shifts at the atomic level, with further details on atomic matrix elements provided in App. A.1. Finally, in Sec. 3.1.3, a mapping of these atomic energy shifts to the piezoaxionic and electroaxionic crystal tensors is outlined.

3.1.1 Nucleus

In this section, we compute the $\bar{\theta}_a$-dependent Schiff moment of nuclei. The most basic P- and T-violating electromagnetic moment of a nucleus is its electric dipole moment (EDM). (An EDM is P-odd and T-even, but its alignment with spin, which itself is P-even and T-odd, is what violates P and T separately.) Our ability to probe nuclear EDMs in atomic systems is, however, restricted by Schiff's screening theorem [67, 96–99]. In any system composed of nonrelativistic, pointlike, charged particles (e.g. an atom or crystal), the bare EDMs of all particles are perfectly screened by a spatial rearrangement of the (monopole) electric charges. However, nuclei have a finite radius R_0, so the position of their EDMs need not coincide with their centers of charge. One can systematically take into account these finite-size effects through a nuclear multipole expansion: an EDM at dimension 1, a magnetic quadrupole moment (MQM) at dimension 2, an electric octupole moment (EOM) and a Schiff moment at dimension 3, etc. The EDM is screened, the MQM only has effects in magnetic materials, and effects on the electronic wavefunction from the EOM are suppressed by the angular-momentum barrier near the nucleus [98]. (Moments at dimension 4 and higher are completely negligible.)

Hence our focus on the Schiff moment, which interacts with electrons via the Hamiltonian:

$$H_{\mathsf{S}} = 4\pi e \mathbf{S} \cdot \boldsymbol{\nabla}\delta(\mathbf{r}), \tag{3.1}$$

where $\boldsymbol{\nabla}\delta(\mathbf{r})$ is to be evaluated on the electron wavefunction. Like an EDM, a Schiff moment is P-odd and T-even, but its alignment with the nuclear spin violates both P and T invariance. Note that the effective operator on electrons is P-odd and T-even. A Schiff moment [99]

$$\mathbf{S} = \mathbf{S}_{\text{EDM}} + \mathbf{S}_{\text{ch}} \tag{3.2}$$

can arise from EDMs of the constituent nucleons

$$\mathbf{S}_{\text{EDM}} = \sum_{j=p,n} \left\{ \frac{1}{6} e \left[\mathbf{r}_j (\mathbf{r}_j \cdot \mathbf{d}_j) - \frac{1}{3} \langle r^2 \rangle_{\text{ch}} \mathbf{d}_j \right] + \frac{1}{6} e \left(r_j^2 \mathbf{r}_j - \langle r^2 \rangle_{\text{ch}} \mathbf{r}_j \right) \right\} \tag{3.3}$$

and from an asymmetrical distribution of charge (i.e. protons) within the nucleus

$$\mathbf{S}_{\text{ch}} = \sum_p \frac{1}{10} e \left(r_p^2 \mathbf{r}_p - \frac{5}{3} \langle r^2 \rangle_{\text{ch}} \mathbf{r}_p \right). \tag{3.4}$$

In Eq. 3.3, the sum over j runs over all nucleons (protons p and neutrons n), while the sum in Eq. 3.4 runs over all protons. Above, we have also used shorthand for the mean squared radius of the nuclear charge distribution (with density $\rho_{\rm ch}$):

$$\langle r^2 \rangle_{\rm ch} \equiv \frac{1}{Z} \int \mathrm{d}^3\mathbf{r}\, r^2 \rho_{\rm ch}(\mathbf{r}), \tag{3.5}$$

with Z the total nuclear charge. The *magnitude* of the Schiff moment is defined as $\mathsf{S} \equiv \langle \mathsf{S}_z \rangle_{M=I}$, i.e. the magnitude of the expectation value of $\mathbf{S}$ in the $+z$-direction, for a fully polarized nuclear spin along the $+z$-direction ($M = I$).

As we derive below, the effects from the Schiff moment are largest in high-Z nuclei, because of their larger size and because of relativistic enhancement effects of the electron density for heavy nuclei (see Sec. 3.1.2 for this second effect). In Sec. 3.1.1, we evaluate the size of the Schiff moments from bare nucleon EDMs through Eq. 3.3. In Sec. 3.1.1, we review the PT-violating nuclear forces that arise at finite $\overline{\theta}_a$, and then evaluate the resulting Schiff moments via Eq. 3.4 in non-deformed nuclei in Sec. 3.1.1, and in octupole-deformed nuclei in Sec. 3.1.1.

Schiff moment from the EDM of a valence nucleon

A theta term, from a static $\overline{\theta}$ or from an oscillating $\overline{\theta}_a$ in a QCD axion DM background, induces a typical nucleon EDM of order [50, 67]:

$$d_n \approx 10^{-3}\, \overline{\theta}_a \, \mathrm{e\ fm}. \tag{3.6}$$

This nucleon EDM in turn produces a nuclear Schiff moment in nuclei with odd atomic number A. For an odd-A nucleus with a static, spherically symmetric core of radius $R_0 \simeq r_0 A^{1/3}$ with $r_0 \approx 1.2\,\mathrm{fm}$, the valence nucleon EDM leads to a Schiff moment magnitude [98]:

$$\begin{aligned} \mathsf{S}_{\rm EDM} &= \frac{1}{10} d_n R_0^2 \frac{2}{5} \frac{(K+1)}{(I+1)} \\ &\sim 10^{-3}\, \overline{\theta}_a \, e\, \mathrm{fm}^3 \frac{(K+1)}{(I+1)} \left(\frac{A}{230}\right)^{2/3}, \end{aligned} \tag{3.7}$$

with $K \equiv (l-I)(2I-1)$, I the nuclear spin, and l the valence nucleon's orbital angular momentum. The nuclear core may exhibit significant polarizability and deformations from sphericity, in which case the estimate of Eq. 3.7 will receive large corrections. However, in those cases, the $\mathsf{S}_{\rm EDM}$ contribution to the Schiff moment will be subdominant to the asymmetric charge distribution of the nucleus, to which we turn next.

P−and T−violating forces

Forces between nucleons that violate parity and time-reversal symmetries can cause an asymmetric (parity-odd) charge distribution of the nucleus that is aligned with the nuclear spin, thus generating a Schiff moment $\mathsf{S}_{\rm ch}$ via Eq. 3.4 [100–102]. Since this is a tree-level effect from light-meson exchange between nucleons, this contribution to the Schiff moment will typically dominate over the loop-level effect from Eqs. 3.6 and 3.7. To leading order, these P- and T-violating forces are mediated by pion exchange; in the heavy-pion limit ($m_\pi R_0 \gg 1$) and nonrelativistic approximation, they are given by the effective interaction potential:

$$V_{\mathsf{PT}} = \frac{1}{2m_N m_\pi^2}(\eta_{ab}\boldsymbol{\sigma_a} - \eta_{ba}\boldsymbol{\sigma_b}) \cdot \boldsymbol{\nabla}\delta(\boldsymbol{r}_a - \boldsymbol{r}_b). \tag{3.8}$$

where $m_N \simeq m_n \simeq m_p$ is the nucleon mass, the Pauli matrix $\boldsymbol{\sigma}$ acts on the spin Hilbert space of the nucleons a and b, and $\mathbf{r}$ on the position Hilbert space. The effective couplings among protons p and neutrons n are:

$$\eta_{pp} = -\eta_{np} = g_s(g_0 + g_1), \tag{3.9}$$
$$\eta_{nn} = -\eta_{pn} = g_s(g_1 - g_0). \tag{3.10}$$

The coupling g_s is the standard P- and T-conserving pion-nucleon coupling, while g_0, and g_1 are the P- and T-violating isoscalar and isovector couplings, respectively, sourced by the $\overline{\theta}_a$ term. We assume the numerical values [103]:

$$g_s \approx -13.45, \tag{3.11}$$
$$g_0 \approx (15.5 \pm 2.6) \times 10^{-3}\,\overline{\theta}_a, \tag{3.12}$$
$$g_1 \approx -0.2 g_0. \tag{3.13}$$

We neglect the numerically smaller isotensor pion-nucleon coupling g_2. The contributions to V_{PT} from exchange of ρ and ω mesons have been argued by Refs. [104, 105] to be smaller than the pion-exchange contributions from Eq. 3.8, by the numerical factor $0.3(m_\pi^2/m_{\rho,\omega}^2)$.

Non-deformed nuclei

The P- and T-odd internucleon potential of Eq. 3.8 provides the symmetry breaking needed to create a P-odd charge distribution of a nucleus. Since the values of $\overline{\theta}_a$ of interest are

tiny (cfr. Eq. 2.18), we will evaluate the Schiff moment in perturbation theory:

$$\langle \mathbf{S}_{\rm ch} \rangle = \sum_n \frac{\langle 0|V_{\not\mathsf{PT}}|n\rangle \, \langle n|\mathbf{S}_{\rm ch}|0\rangle}{E_0 - E_n} + \text{h.c.}, \tag{3.14}$$

where the sum is over nuclear states n with energies E_n; $n = 0$ labels the ground state.

In the nuclear shell model, where the core is treated as a static source, only a valence proton can generate a nonzero Schiff moment. The effective mean-field interaction potential of the valence nucleon (with label a) stemming from Eq. 3.8 becomes:

$$V_{\not\mathsf{PT}} = \frac{1}{2m_N m_\pi^2} \eta_a \boldsymbol{\sigma}_a \cdot \boldsymbol{\nabla}_a \rho(\mathbf{r}_a), \tag{3.15}$$

$$\eta_a \equiv \eta_{ap} \frac{Z}{A} + \eta_{an} \frac{A-Z}{A}, \tag{3.16}$$

with ρ the number density of core neutrons and protons normalized as $\int \mathrm{d}^3 r \, \rho(\mathbf{r}) = A$. (In the above formulae, we ignore corrections of order $1/A$ and $1/Z$.) The contribution to the Schiff moment from a valence proton in the nuclear shell model is [100]:

$$\mathsf{S}_{\rm ch} \simeq \frac{e}{10} \frac{\eta_a}{2m_N m_\pi^2} \frac{\rho_0}{U_0} R_0^2 \simeq \frac{3e\eta_a}{4\pi^2 m_N} R_0^2 \tag{3.17}$$

with $\rho_0 \simeq 3/(4\pi r_0^3)$ the nucleon number density, and $U_0 \simeq 3\pi/(60 m_\pi^2 r_0^3)$ the spherically symmetric potential of the nuclear core.

However, excitations of *core protons*, which are dynamics not captured within the nuclear shell model, by either a valence proton or neutron, can yield Schiff moment contributions of similar size as the expression in Eq. 3.17 [106]. This means that P- and T-odd forces can generate Schiff moments in nuclei with either an odd number of protons or an odd number neutrons. Numerically, the effect in Eq. 3.17 is typically much larger than that of Eq. 3.7. For example, one finds:

$$\mathsf{S}_{\rm ch}\left({}^{181}_{73}\mathrm{Ta}\right) \simeq 0.2 \, \overline{\theta}_a \, e \, \mathrm{fm}^3 \tag{3.18}$$

for the stable nucleus of ${}^{181}_{73}$Ta, which has one valence proton. Estimates for other stable isotopes of heavy nuclei can be found e.g. in Ref. [99].

Octupole-deformed nuclei

A class of nuclei with strongly enhanced P- and T-violating moments are those possessing *permanent octupole deformations* or *soft octupole modes*. (For reviews on deformed nuclei,

see Refs. [107–110].) Such nuclei typically have anomalously large values for certain transition matrix elements, paired with small energy splittings between opposite-parity nuclear levels. The origin of these two signatures and their role in collective enhancements of the nuclear Schiff moment will be summarized here, following Refs. [111, 112].

We first discuss permanent octupole deformation of heavy nuclei. Analogously to the Born-Oppenheimer approximation in molecules, where one factorizes rotational motion of a "rigid" shape from the internal excitations (vibration, electronic excitations, etc.), we can consider the shape of the nucleus in the intrinsic (body-fixed) frame of the nucleus. Assuming the nuclear core to be axially symmetric and of constant density (equal for protons and neutrons), the core shape is described by the location of its surface R, expanded into the following multipoles l:

$$R = R_0 \left(1 + \sum_{l=1} \beta_l Y_{l0}\right), \tag{3.19}$$

where the β_i parameters characterize the strength of the dipole, quadrupole, octupole, etc. deformations. The dipole deformation β_1 is fixed such that the center of mass/charge is at the origin. In the intrinsic frame, and with the above assumptions, the Schiff moment can then be straightforwardly calculated using Eq. 3.4:

$$\mathsf{S}_{\rm ch}^{\rm (int)} = ZeR_0^3 \frac{3}{20\pi} \sum_{l=2} \frac{(l+1)\beta_l \beta_{l+1}}{\sqrt{(2l+1)(2l+3)}}, \tag{3.20}$$

with the main piece typically coming from the first term $\propto \beta_2\beta_3$.

If a deformed nucleus is reflection asymmetric in its intrinsic frame, then in the laboratory frame, its ground state wavefunction will be composed of a parity doublet:

$$\Psi^{\pm} = \frac{1}{\sqrt{2}}(|IMK\rangle \pm |IM-K\rangle). \tag{3.21}$$

Here I is the nuclear spin, M is the quantum number of I_z, and K that of the operator $\mathbf{I}\cdot\mathbf{n}$, with $\mathbf{n}$ the nuclear axis. The wavefunctions $\Psi^{\pm}$ are good parity states since $\langle\Psi^{\pm}|\mathbf{n}|\Psi^{\pm}\rangle = 0$, i.e. there is no average orientation of the nuclear axis, and P and T are preserved. Turning around the argument, a tell-tale signature of static octupole deformation of a nucleus is the presence of a low-lying opposite-parity level with the same angular momentum as the ground state. (In reality, the members of the parity doublet are not exactly degenerate due to Coriolis forces and other effects; these are analogous to the rovibrational and vibronic couplings that signal corrections to the Born-Oppenheimer approximation for molecular states.)

Interactions that violate both P and T can mix these opposite-parity states of a spin-polarized nucleus, and partially align the nuclear axis with the nuclear spin, leading to a collective enhancement of the Schiff moment. The perturbed wavefunctions under the interaction Hamiltonian of Eq. 3.15 are:

$$\widetilde{\Psi}^+ = \Psi^+ + \widetilde{\alpha}\Psi^-, \quad \widetilde{\Psi}^- = \Psi^- - \widetilde{\alpha}\Psi^+, \tag{3.22}$$

where

$$\widetilde{\alpha} = \frac{\langle \Psi^- | V_{\mathsf{PT}} | \Psi^+ \rangle}{\Delta E_\pm} \approx 0.5\, \overline{\theta}_a \frac{\eta_a}{0.1} \frac{50\,\mathrm{keV}}{\Delta E_\pm} \frac{\beta_3}{0.1} \left(\frac{230}{A}\right)^{1/3}, \tag{3.23}$$

with $\Delta E_\pm \equiv E^+ - E^-$ the energy splitting of the doublet and η_a the effective coupling of the valence nucleon as in Eq. 3.16. Within this framework, we then finally have $\langle \widetilde{\Psi}^\pm | n_z | \widetilde{\Psi}^\pm \rangle = 2\widetilde{\alpha} K M/[(I+1)I]$, and since the ground-state wavefunction typically has $K = I$ [111], a laboratory-frame Schiff moment of

$$\begin{aligned} \mathsf{S}_{\mathrm{ch}} &= 2\widetilde{\alpha} \frac{I}{I+1} \mathsf{S}_{\mathrm{ch}}^{(\mathrm{int})} \\ &\approx 5\, \overline{\theta}_a\, e\,\mathrm{fm}^3 \frac{\eta_a}{0.1} \frac{50\,\mathrm{keV}}{\Delta E_\pm} \frac{\beta_2}{0.12} \left(\frac{\beta_3}{0.1}\right)^2 \frac{Z}{88} \left(\frac{A}{230}\right)^{2/3}. \end{aligned} \tag{3.24}$$

Contributions from higher-order deformations of the nucleus are usually subdominant. We observe that the collective (Z-enhanced) effect of static octupole deformation can lead to very large Schiff moments, compared to the contributions from valence nucleons in non-deformed nuclei (Eqs. 3.17 and 3.18) and from bare EDMs of the valence nucleons (Eq. 3.7). Tabulations of the parameters β_2, β_3, and $\Delta E_\pm$ can be found in Ref. [113] for the ground states of nearly all nuclei, though estimates with other nuclear structure models often give different results [114, 115].

The class of nuclei with collectively enhanced Schiff moments extends beyond those with static octupole deformations, and includes also those with *soft octupole modes*. Ref. [112] showed that it is sufficient to have a significant octupole-deformation-*squared*, i.e. $\langle \beta_3^2 \rangle \neq 0$, even if $\langle \beta_3 \rangle = 0$, for a nucleus to have a Z-enhanced Schiff moment. This dynamical octupole deformation can be thought of as a collective nuclear octupole vibration with angular frequency $\Delta E_\pm$, and corresponding zero-point amplitude-squared inversely proportional to this frequency, $\langle \beta_3^2 \rangle \propto 1/\Delta E_\pm$, as for any quantum harmonic oscillator.

An ideal octupole-enhanced candidate nuclear isotope (with either static or dynamical deformation) should thus have an opposite-parity level with a small energy gap above the ground state. For the experimental concept proposed in this paper, the isotope needs to

be (meta)stable (cfr. the discussion on heating from radioactivity in Sec. 3.2.3). Energy splittings and half-lives are tabulated in Ref. [116]. Three potentially suitable isotopes were suggested in Ref. [117], together with estimates of their Schiff moments:

$$\mathsf{S}_{\rm ch}\left({}^{153}_{63}\mathrm{Eu}\right) \approx 3.7\,\overline{\theta}_a\,e\,\mathrm{fm}^3, \tag{3.25}$$

$$\mathsf{S}_{\rm ch}\left({}^{235}_{92}\mathrm{U}\right) \approx 3.0\,\overline{\theta}_a\,e\,\mathrm{fm}^3,\ \tau_{1/2} \approx 7\times 10^8\,\mathrm{yr}, \tag{3.26}$$

$$\mathsf{S}_{\rm ch}\left({}^{237}_{93}\mathrm{Np}\right) \approx 6.0\,\overline{\theta}_a\,e\,\mathrm{fm}^3,\ \tau_{1/2} \approx 2\times 10^6\,\mathrm{yr}. \tag{3.27}$$

In addition, the isotopes ${}^{161}_{66}\mathrm{Dy}$ and ${}^{155}_{64}\mathrm{Gd}$ are known to have very small energy gaps between the ground state and the excited state of opposite parity [116], which suggests a possible octupole enhancement. According to Ref. [113], they are not statically octupole deformed, but they could still exhibit significant dynamical octupole deformation. We therefore estimate the Schiff moment from soft octupole vibrations using Eq. 3.24 as suggested in Ref. [112], with the squared octupole deformation estimated using the collective $B(E3)$ octupole transition probability for neighbouring even-even nuclei found in e.g. Ref. [118]:

$$B(E3)_{0^+\to 3^-} = \left(\frac{3}{4\pi}\right)^2 \left(ZeR_0^3\right)^2 \langle\beta_3^2\rangle\,. \tag{3.28}$$

Data from Ref. [116] with Eqs. 3.24 and 3.28 then yields our estimates:

$$\mathsf{S}_{\rm ch}\left({}^{161}_{66}\mathrm{Dy}\right) \approx 4\,\overline{\theta}_a\,e\,\mathrm{fm}^3, \tag{3.29}$$

$$\mathsf{S}_{\rm ch}\left({}^{155}_{64}\mathrm{Gd}\right) \approx 1\,\overline{\theta}_a\,e\,\mathrm{fm}^3. \tag{3.30}$$

Despite these encouragingly large fiducial values, the accuracy of the predictions in this section is under poor control, as different nuclear structure models suggest widely different values [109, 110]. More theoretical support is needed to identify suitable candidate isotopes for a large-scale experiment, and to provide accurate and precise determinations of the predicted Schiff moments in the presence of a nonzero $\overline{\theta}_a$ parameter.

3.1.2 Atom

In Eq. 3.1 of Sec. 3.1.1, we already wrote down the parity-odd electrostatic potential for electrons produced by a nuclear Schiff moment. This potential can mix opposite-parity electronic states, or equivalently, lead to an atomic energy shift if the electronic wavefunction already breaks parity (which is the case inside a piezoelectric crystal).

The energy shift of an atom with a polarized nuclear spin[1] and Schiff moment, from the perturbing Hamiltonian in Eq. 3.1, is:

$$\langle H_{\mathsf{S}} \rangle = -4\pi e \mathsf{S} \sum_{j,m_j,k} \hat{I}_k \epsilon_s \epsilon^*_{p_{j,m_j}} \mathcal{M}_{j,m_j,k} + \text{c.c.}, \tag{3.31}$$

$$\equiv -4\pi e \mathsf{S} \sum_k \mathcal{M}_k \hat{I}_k; \tag{3.32}$$

where the quantum numbers j and m_j are those of the total angular momentum and its projection on the z-axis, respectively, the index k denotes spatial direction, $\hat{I}_k$ is the direction of the nuclear spin (normalized such that $|\hat{\mathbf{I}}| = 1$ corresponds to a fully polarized nuclear spin state, and $|\hat{\mathbf{I}}| = 0$ an unpolarized state), and $\mathcal{M}_{j,m_j,k} = \langle s^0 | \hat{r}_k \, \partial_r \delta^3(\mathbf{r}) \, | p^0_{j,m_j} \rangle$ is an atomic matrix element. The coefficients ϵ_s and $\epsilon_{p_{j,m_j}}$ parametrize the admixture of atomic s and p_{j,m_j} valence electron states, i.e. $|\psi_{\text{el}}\rangle = \epsilon_s \, |s^0\rangle + \sum_{j,m_j} \epsilon_{p_{j,m_j}} \, |p^0_{j,m_j}\rangle$, and characterize the breaking of parity symmetry by the crystal potential. (This treatment of the atom's wavefuction in a crystal is only possible in the tight-binding approximation, which holds to leading order for the insulating crystals considered in this paper.) The admixture of opposite-parity states in the atom's ground state in the crystal allows for a piezoaxionic effect *linear* in the Schiff moment, without the need of other parity-breaking sources such as the application of an external electric field. We expand on this procedure in App. A.1.

The energy shift of Eq. 3.32 can be reliably calculated in perturbation theory up to a wavefunction normalization constant, as the Schiff interaction of Eq. 3.1 is a short-distance effect where screening effects are unimportant. Armed with only a few inputs, namely $E_s \equiv \alpha^2 m_e / 2\nu_s$ and $E_{p_j} \equiv \alpha^2 m_e / 2\nu_{p_j}$ with effective quantum numbers ν_s and ν_j, the normalization of the radial part of the wavefunctions can be fixed by the matching procedure of Ref. [98, Ch. 8]. This leads to a matrix element of the form:

$$\mathcal{M}_{j,m_j,k} = \langle \Omega_s | \hat{r}_k | \Omega_{p,j,m_j} \rangle \, \frac{Z^2}{a_0^4 (\nu_s \nu_{p_j})^{3/2}} \mathcal{R}_j \tag{3.33}$$

where $a_0 \equiv 1/\alpha m_e$ is the Bohr radius, Ω are the spinor spherical harmonics as in Ref. [119, §24], and their angular matrix elements in Eq. 4.11 are $\mathcal{O}(1)$ and evaluated in App. A.1.

[1] Technically, we are referring here to the polarization of an ensemble of nuclear spins, within which we are studying a single atom.

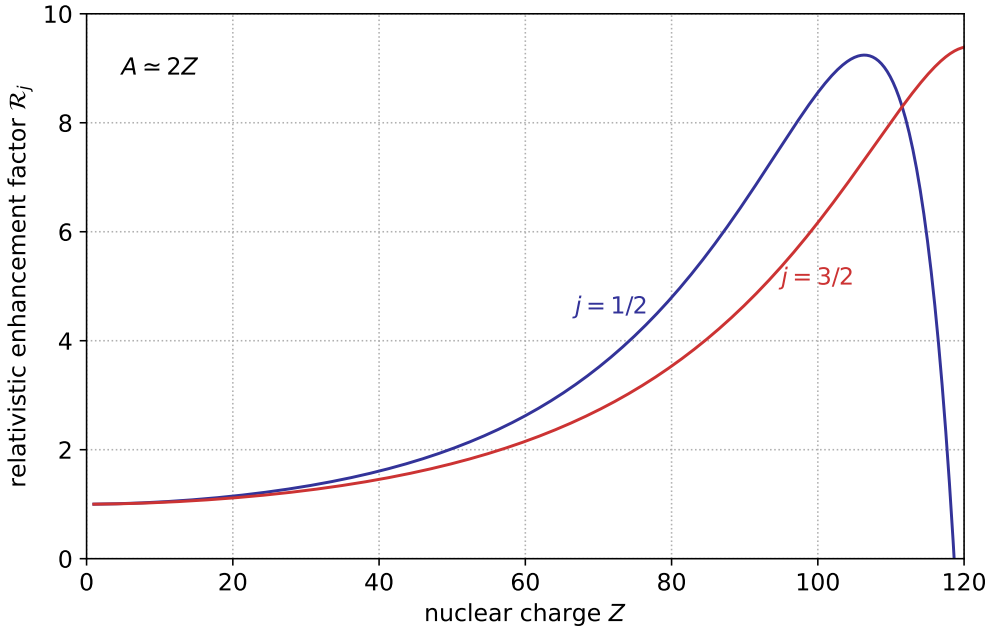

Figure 3.1: The relativistic enhancement factor $\mathcal{R}_j$ of Eqs. 3.34 and 3.35 as a function of the proton number Z, assuming an atomic number of $A \approx 2Z$, for two values of the total electron angular momentum $j = 1/2, 3/2$.

The relativistic enhancement factors $\mathcal{R}_j$ are defined as:

$$\mathcal{R}_{\frac{1}{2}} = \frac{3\gamma_{\frac{1}{2}}(2\gamma_{\frac{1}{2}} - 1)}{2\gamma_{\frac{1}{2}} + 1} \frac{4}{\Gamma^2(2\gamma_{\frac{1}{2}} + 1)} \left(\frac{a_0}{2ZR_0}\right)^{2-2\gamma_{\frac{1}{2}}} \tag{3.34}$$

$$\mathcal{R}_{\frac{3}{2}} = \frac{6\left[(\gamma_{\frac{1}{2}} + 1)(\gamma_{\frac{3}{2}} + 2) + Z^2\alpha^2\right]}{\Gamma(2\gamma_{\frac{1}{2}} + 1)\Gamma(2\gamma_{\frac{3}{2}} + 1)}, \tag{3.35}$$

$$\times \left(\gamma_{\frac{1}{2}} + \gamma_{\frac{3}{2}} - 2\right) \left(\frac{a_0}{2ZR_0}\right)^{3-\gamma_{\frac{1}{2}}-\gamma_{\frac{3}{2}}},$$

$$\gamma_j = \sqrt{\left(j + \frac{1}{2}\right)^2 - Z^2\alpha^2}. \tag{3.36}$$

These enhancement factors are defined such that they go to unity in the limit $Z\alpha \to 0$, and evaluate to about 3–8 for nuclei of interest, with $60 \lesssim Z \lesssim 93$, see Fig. 3.1.

A numerical estimate of the energy shift yields:

$$\langle H_{\mathsf{S}} \rangle \approx 2.0 \times 10^{-24}\,\mathrm{eV} \times \left(\frac{Z}{80}\right)^2 \frac{\mathcal{R}\,(\nu_s\,\nu_p)^{-\frac{3}{2}}}{10} \frac{\mathsf{S}}{\overline{\theta}_a\, e\,\mathrm{fm}^3} \frac{\epsilon_s \epsilon_p \hat{I}_k\,\langle \Omega_s | \hat{r}_k | \Omega_p \rangle}{1}, \tag{3.37}$$

where we assume $\overline{\theta}_a$ is given by the rms amplitude of Eq. 2.18, i.e. that the QCD axion makes up all of the DM.

3.1.3 Crystal

Up to this point, we have reviewed how QCD axion DM gives rise to an oscillatory $\overline{\theta}_a$ angle, nuclear Schiff moments (Sec. 3.1.1), and atomic energy shifts (Sec. 3.1.2). In this section, we will show how the latter translates in effective stresses and electric displacements in macroscopic crystals.

The internal energy density U of the crystal can be expanded to quadratic order around its equilibrium as:

$$U = \frac{\mathbf{S}^\intercal \mathbf{c}^D \mathbf{S}}{2} - \mathbf{D}^\intercal \mathbf{h} \mathbf{S} + \frac{\mathbf{D}^\intercal \boldsymbol{\beta}^S \mathbf{D}}{2} - \mathbf{S}^\intercal \boldsymbol{\xi} \hat{\mathbf{I}} \overline{\theta}_a - \mathbf{D}^\intercal \boldsymbol{\zeta} \hat{\mathbf{I}} \overline{\theta}_a. \tag{3.38}$$

Here the independent variables are the strain 2-tensor $\mathbf{S}$, the electric displacement vector $\mathbf{D}$, the nuclear spin polarization direction $\hat{\mathbf{I}}$ (normalized so that saturated spin polarization corresponds to $|\hat{\mathbf{I}}| = 1$), and the axionic theta angle $\overline{\theta}_a$. The proportionality constants of the first three terms are given by the elastic stiffness 4-tensor (at constant electric displacement) $\mathbf{c}^D$, piezoelectric 3-tensor $\mathbf{h}$, and dielectric impermittivity 2-tensor (at constant strain) $\boldsymbol{\beta}^S$. In the last two terms, we introduce new interactions at linear order in the nuclear Schiff moment direction, whose proportionality constants we will refer to as the "piezoaxionic" 3-tensor $\boldsymbol{\xi}$ and "electroaxionic" 2-tensor $\boldsymbol{\zeta}$. In absence of these two nuclear-spin-induced contributions, the internal energy density above reduces to the usual expression for a piezoelectric crystal, which can be found e.g. in Ref. [120, Ch. 5]. Superscripts $^\intercal$ denote transposed quantities. We assume all quantities are given at (or near) zero temperature. We have also integrated out short-wavelength fluctuations, such as individual atomic displacements, a more detailed treatment of which is given in App. A.2; all quantities in Eq. 3.38 should be understood to be (nearly) homogeneous.

The constitutive equations for the stress $\mathbf{T}$ and electric field $\mathbf{E}$ can be written as first

derivatives of the internal energy density of Eq. 3.38 [120],

$$\mathbf{T} = \frac{\partial U}{\partial \mathbf{S}} = +\mathbf{c}^D\mathbf{S} - \mathbf{h}^\intercal\mathbf{D} - \boldsymbol{\xi}\hat{\mathbf{I}}\overline{\theta}_a, \tag{3.39}$$

$$\mathbf{E} = \frac{\partial U}{\partial \mathbf{D}} = -\mathbf{h}\mathbf{S} + \boldsymbol{\beta}^S\mathbf{D} - \boldsymbol{\zeta}\hat{\mathbf{I}}\overline{\theta}_a. \tag{3.40}$$

Equations 3.39 and 3.40 reveal that an axion DM background in the presence of nuclear spin polarization manifests itself both as a stress across the crystal due to $\boldsymbol{\xi}$ and an electric field due to $\boldsymbol{\zeta}$.

For the subsequent discussion of our proposed experimental setup and sensitivity, it is instructive to introduce Voigt notation. In this notation, the independent components of 3×3 symmetric tensors such as the strain $S_{\alpha\beta}$ and stress $T_{\alpha\beta}$ are reduced to 6 dimensional "vectors" S_i and T_i, and the indices of their proportionality constants are reduced similarly (see App. A.2 for further details). The above equations can thus be written as:

$$T_n = +c^D_{nk}S_k - h^\intercal_{nk}D_k - \xi_{nk}\hat{I}_k\overline{\theta}_a, \tag{3.41}$$

$$E_n = -h_{nk}S_k + \beta^S_{nk}D_k - \zeta_{nk}\hat{I}_k\overline{\theta}_a; \tag{3.42}$$

with Einstein summation convention on repeated indices.

The piezoaxionic tensor in Eq. 3.38 can be computed from the atomic matrix element $\mathcal{M}$ of Sec. 3.1.2 through

$$\begin{aligned}\xi_{nk} &= \frac{\partial}{\partial\overline{\theta}}\sum_{t=1}^{N_\mathsf{S}} 4\pi e\mathsf{S}\frac{\partial}{\partial S_n}\sum_{j,m_j}\left[\frac{\epsilon_s\epsilon^*_{p_{j,m_j}}\mathcal{M}_{j,m_j,k}}{V_c} + \text{c.c.}\right]_{(t)} \\ &\equiv \widetilde{\xi}_{nk}\frac{4\pi eN_\mathsf{S}}{V_c}\frac{\mathrm{d}\mathsf{S}}{\mathrm{d}\overline{\theta}}\mathcal{M}_k,\end{aligned} \tag{3.43}$$

which follows directly from Eq. 3.32, and where the subscript $t = 1, \ldots, N_\mathsf{S}$ runs over the spin-polarized nuclei (which are all assumed to have the same Schiff moment S) in the unit cell with volume V_c. The electroaxionic tensor is given by a similar formula:

$$\begin{aligned}\zeta_{nk} &= \frac{\partial}{\partial\overline{\theta}}\sum_{t=1}^{N_\mathsf{S}} 4\pi e\mathsf{S}\frac{\partial}{\partial D_n}\sum_{j,m_j}\left[\frac{\epsilon_s\epsilon^*_{p_{j,m_j}}\mathcal{M}_{j,m_j,k}}{V_c} + \text{c.c.}\right]_{(t)} \\ &\equiv \widetilde{\zeta}_{nk}\frac{4\pi eN_\mathsf{S}}{V_c}\frac{ea_0^2}{\alpha}\frac{\mathrm{d}\mathsf{S}}{\mathrm{d}\overline{\theta}}\mathcal{M}_k.\end{aligned} \tag{3.44}$$

In Eqs. 3.43 and 3.44, we have defined the dimensionless quantities $\widetilde{\xi}$ and $\widetilde{\zeta}$, respectively, and are the only factors through which the electron wavefunction properties of the atoms in the crystal enter.

A density functional theory (DFT) calculation of $\widetilde{\xi}$ and $\widetilde{\zeta}$ for materials of interest is left to future work. Here, we will content ourselves with naive dimensional analysis (NDA) estimates, guided by crystal symmetry principles and augmented with certain measured crystal tensors. From NDA, we expect the "conventional" crystal tensors to be given by:

$$c^D_{nk} \equiv \widetilde{c}^D_{nk} \frac{N_c \alpha}{a_0 V_c}, \tag{3.45}$$

$$h_{nk} \equiv \widetilde{h}_{nk} \frac{N_c e a_0}{V_c \, \varepsilon}, \tag{3.46}$$

$$\beta^S_{nk} \equiv \widetilde{\beta}^S_{nk} \tag{3.47}$$

with N_c the number of atoms per unit cell and ε the relevant component of the dielectric tensor for a given mode. The factor of ε is necessary to convert between the density of electric dipole moments produced by the piezoaxionic effect and the resultant electric field. This NDA approach, which we have been unable to find in the literature, typically agrees with the measured (and/or calculated) values of the corresponding stiffness, piezoelectricity, and dielectric properties within an order of magnitude. The disagreement between the universal NDA approach and individual material properties is captured by the tensors $\widetilde{c}^D_{nk}$, $\widetilde{h}_{nk}$, and $\widetilde{\beta}^S_{nk}$, which generally have $\mathcal{O}(1)$ dimensionless coefficients.

Crystal symmetry dictates that certain components of crystal tensors vanish. For example, $\widetilde{h}_{kn}$ and $\widetilde{\xi}_{kn}$ are odd under a parity transformation of the crystal lattice, so they must vanish identically for parity-even crystals. The piezoaxionic effect can therefore only be present in crystals with piezoelectric point groups, which constitute 20 geometric crystal classes (out of a total of 32) [121]. The point group of the crystal further constrains relations among the components of the piezoelectric and piezoaxionic tensors. For example, for the crystal class 32 which includes quartz, the symmetry of the piezoelectric tensor is given by:

$$h_{nk} = \begin{pmatrix} h_{11} & -h_{11} & 0 & h_{14} & 0 & 0 \\ 0 & 0 & 0 & 0 & -h_{14} & -h_{11} \\ 0 & 0 & 0 & 0 & 0 & 0 \end{pmatrix}, \tag{3.48}$$

and the ξ tensor has exactly the same symmetry structure. The electroaxionic tensor $\widetilde{\zeta}_{nk}$ is even under a parity transformation of the crystal structure, and is generally nonvanishing for any crystal.

Based on the crystal symmetries and the parity properties of the different coefficients, we expect that:

$$\left(\widetilde{\xi}_{nk}\right)^{\mathsf{T}} \sim \widetilde{h}_{nk} \quad \text{and} \quad \widetilde{\zeta}_{nk} \sim \widetilde{\beta}^{S}_{nk}, \tag{3.49}$$

allowing a preliminary estimate of the piezoaxionic and electroaxionic tensors from *measurements* of piezoelectric and dielectric properties. The relations in Eq. 3.49 capture suppression (enhancement) effects in the crystal, leading to numerically small (large) $\widetilde{h}_{nk}$ and $\widetilde{\xi}_{nk}$. In the case of quartz, for example, the piezoelectric tensor components are $e_{11} = 0.17\,\mathrm{C/m^2}$ and $e_{14} = -0.041\,\mathrm{C/m^2}$ at room temperature [122], corresponding to $\widetilde{h}_{11} = 0.80$ and $\widetilde{h}_{14} = -0.19$ (these piezoelectric constants are related as $h_{mi} = \beta^{S}_{nm} e_{ni}$ [123, Ch. IIIA]), suggesting that the piezoaxionic and electroaxionic tensors in the quartz crystal are also $\mathcal{O}(1)$. (Quartz is not a good candidate material, primarily due to the smallness of the $^{29}_{14}$Si Schiff moment.) We have verified this NDA estimate for a number of materials using measured values also found in reference [122]. For langasite, $\widetilde{h}_{11} = 0.71$, and for PZT (Lead Zirconate Titanate), $\widetilde{h}_{33}$ can vary from $\sim 20 - 70$.

We do not expect Eq. 3.49 to hold much better than up to an $\mathcal{O}(1)$ number. Firstly, piezoelectricity depends on electron charge redistribution (under strain) in the entire unit cell, whereas piezoaxionicity only depends on electronic wavefunction changes near spin-polarized nuclei of interest. Secondly, only electron wavefunction components with minimal angular momentum (and thus large nuclear overlap) contribute to the piezoaxionic effect, whereas there is no such restriction for piezoelectricity.

In summary, we have shown that a nuclear Schiff moment can lead to stresses and electric fields via Eqs. 3.39 and 3.40, respectively. QCD axion dark matter generates *oscillatory* Schiff moments, so these stresses and electric fields also oscillate in time, and can in turn excite acoustic modes and currents, which we aim to detect with setups described in the next section.

Finally, we provide a numerical estimate of the magnitude of the piezoaxionic effect. From Eq. 3.39, the stress induced by a Schiff moment is equal to the stress induced by an equivalent strain of:

$$S_{\mathrm{eq}} \sim \left|\left(\mathbf{c}^{D}\right)^{-1} \boldsymbol{\xi}\hat{\mathbf{I}}\overline{\theta}_a\right| \sim \frac{\widetilde{\xi}P}{\widetilde{c}^{D}} \frac{N_{\mathsf{S}}}{N_c} \frac{Z^2\mathcal{R}}{(\nu_s\nu_p)^{3/2}} \frac{4\pi e}{\alpha a_0^3} \frac{\mathrm{d}\mathsf{S}}{\mathrm{d}\overline{\theta}} \overline{\theta}_a \tag{3.50}$$

$$\sim 3\times 10^{-26} \frac{\widetilde{\xi}P}{\widetilde{c}^{D}} \frac{N_{\mathsf{S}}}{N_c} \left(\frac{Z}{80}\right)^2 \frac{\mathcal{R}(\nu_s\nu_p)^{-\frac{3}{2}}}{10} \frac{\mathsf{S}}{\overline{\theta}_a\, e\,\mathrm{fm}^3}, \tag{3.51}$$

where we have assumed that the amplitude of $\overline{\theta}_a$ is that of Eq. 2.18 and that S is linear in $\overline{\theta}_a$. The fiducial equivalent strain of Eq. 3.51 is just one order of magnitude smaller than the constraints achieved by the AURIGA collaboration, which set a limit on strains induced by scalar dark matter in an aluminum resonant-mass detector at the level of $S \sim \text{few} \times 10^{-25}$, based on a one-month data set [88].

3.2 Experiment

In Sec. 3.1, we reviewed the mechanisms by which QCD axion DM can mix opposite-parity electronic states through short-range interactions with the nucleus, most notably via the nuclear Schiff moment induced by the irreducible QCD axion coupling. It is well known that the resulting effective Hamiltonian induces nuclear spin precession in parity-violating systems. This effect has been exploited in *isolated* atoms or molecules, where parity is broken by a background electric field, to perform static measurements of the strong CP angle $\overline{\theta}$ [124]. Refs. [89, 95] proposed using this nuclear precession effect combined with nuclear magnetic resonance techniques in solid-state systems, to look for an oscillatory $\overline{\theta}_a$ angle from QCD axion DM. Both of these aforementioned schemes rely on *changes in the spin state*, specifically transverse polarization, as their primary signature.

The experimental setup we describe in this section utilizes the piezoaxionic effect of Eq. 3.43 in piezoelectric crystals with spin-polarized nuclei. This setup does not rely on changes of the magnetization of the crystal. Instead, with the nuclear spin polarization fixed both in magnitude and direction, the oscillatory Schiff moment changes the electronic wavefuction so that the crystal lattice structure is no longer in equilibrium, resulting in a stress given by Eq. 3.39. This axion-induced stress excites bulk acoustic modes in the piezoelectric crystal, whose electromechanical coupling admits an electric readout of this strain. Concurrently, the secondary electroaxionic effect parametrized by the ζ tensor of Eq. 3.44 is also generally present in any crystal, and produces an additional electric field contribution via Eq. 3.40.

Our proposed setup detects axion DM through the measurement of these bulk acoustic mode excitations. The acoustic modes are read out electrically (capacitively), and the resulting current is fed to a superconducting quantum interference device (SQUID). The main advantage of our proposal is the extraordinarily low *mechanical* losses of certain piezoelectric crystals. This fact implies very high quality factors (Q-factors) of bulk acoustic modes, and low thermal noise. The associated mechanical Q-factors can be much larger than those of solid-state nuclear spin precession systems or those of purely electric modes. Furthermore, centimeter-scale crystals have natural mechanical resonance frequencies in

the MHz range, providing natural amplification around all of the harmonics, with further scanning possible through electrical loading by an external circuit, as explained below.

We sketch a simplified experimental setup in Sec. 3.2.1, where we also discuss possible candidate materials. For concreteness, we quantitatively describe the signal for one particular geometry in Sec. 3.2.2. We discuss different backgrounds and how they can be mitigated in Sec. 3.2.3. We finally present our sensitivity forecasts for our simplified setup with an idealized material in Sec. 3.2.4.

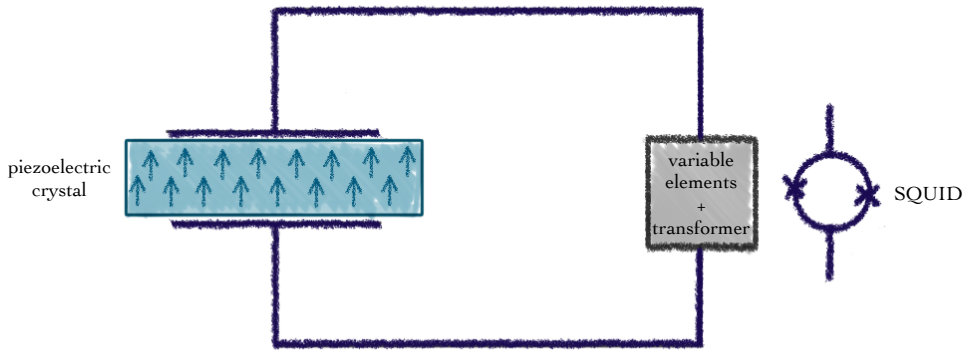

Figure 3.2: A simplified illustration of the proposed experimental setup. The axion-induced stress and resulting strain signal in a piezoelectric crystal with polarized nuclear spins is read out capacitively and ultimately measured through a SQUID. The circuit includes variable inductive and capacitive elements to scan around the mechanical resonance frequency, as well as a transformer circuit for impedance matching with the SQUID.

3.2.1 Setup

Our proposed setup consists of a piezoelectric crystal with electrodes placed on two of its faces, connected to a SQUID via a transformer circuit and variable input inductor and capacitor, as shown schematically in Fig. 4.1. For simplicity of description, we will take the crystal to be a rectangular prism in the form of a thin plate, with electrodes on the two opposing major faces. The nuclear spins are aligned along an appropriately chosen crystal axis in order to maximize sensitivity. For nuclear spins, $\mathcal{O}(1)$ polarization can be achieved through the application of a large magnetic field at the cryogenic temperatures relevant for this experiment, since the Zeeman energy is of order the temperature $\mu_N B \approx 3.7\,\mathrm{mK}$ at $B = 10\,\mathrm{T}$. Due to the long relaxation times in solids, this polarization can be preserved

for extended periods of time under application of a moderate magnetic field on the order of 10^{-4}–10^{-3} T [125].

We focus our treatment of the signal in Sec. 3.2.2 on the thickness expander mode, which has an acoustic wave vector and electric field perpendicular to the major faces; other geometries and modes are also possible and are discussed in App. A.4. Bulk acoustic modes in thin piezoelectric plates have been widely studied (see for example [126–128]) and utilized in industrial, sensing, and fundamental physics applications [129, 130]. We note that curvature of some of the crystal surfaces may help localize acoustic modes in the transverse direction and help minimize clamping losses [131], but for illustrative purposes we ignore this complication.

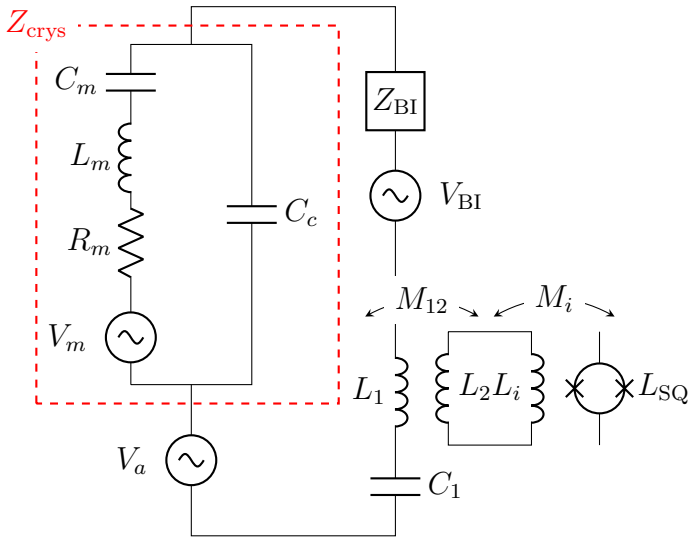

Figure 3.3: Equivalent electric circuit of the experimental set-up described in Sec. 3.2.1 and shown in Fig. 4.1. The axion signal appears as an in-series voltage, V_a, to the piezoelectric crystal with capacitance C_m, inductance L_m, and resistance R_m around mechanical resonance. Two of the crystal's faces are connected to electrodes, resulting in a clamped capacitance C_c. The electrodes are connected to variable electrical components L_1 and C_1. The current inside the circuit is read out inductively by a SQUID through a transformer. The SQUID and transformer contribute also a back-impedance Z_{BI} to the circuit (see text for more details).

The axion signal and the electromechanical dynamics of the crystal will be further expounded in the next section, where we show that they can be modeled by an effective axion voltage V_a in series with an effective "primary" impedance Z_{crys}, respectively, as

shown in the equivalent circuit of Fig. 3.3. Near one of the acoustic resonances, the primary impedance can then further be approximated with an effective mechanical capacitance C_m, inductance L_m, and resistance R_m (see App. A.3), all in parallel with the "clamped capacitance" C_c. The electrodes are connected to a variable capacitor C_1 and a variable inductor with self-inductance L_1. The latter has a mutual inductance M_{12} to an inductor with self-inductance L_2, as part of a transformer circuit. The current inside the transformer circuit is sent to a SQUID with input inductance L_i, mutual inductance M_i, and SQUID self-inductance L_{SQ}, as depicted in Fig. 3.3.

Class	Candidates
32	$\mathrm{Na}\mathbf{Dy}\mathrm{H_2S_2O_9}$ $\mathbf{Bi}\mathrm{PO_4}$
3m	$\mathbf{U}\mathrm{OF_4}$ $\mathbf{U}\mathrm{Cd}$
4mm	$\mathbf{Dy}\mathrm{Si_3Ir}$ $\mathbf{Pb}\mathrm{Zr_xTi_{1-x}O_3}$ (PZT) $\mathbf{Dy}\mathrm{AgSe_2}$
$\bar{4}$2m	$\mathbf{Dy}\mathrm{AgTe_2}$ $\mathbf{Dy_2}\mathrm{Be_2GeO_7}$
mm2	$\mathbf{U}\mathrm{CO_5}$

Table 3.2: Candidate crystals for our setup, categorized by their crystal structure, as found in Ref. [132]. The nucleus with the largest Schiff moment in each compound is printed in bold.

Materials

The sensitivity of our setup relies crucially on a number of material properties, most importantly piezoelectric and dielectric properties, low mechanical losses, and a high concentration of nuclei with large Schiff moments. In this section, we identify a number of suitable crystals with these properties, and discuss possible measures to improve the sensitivity of a given crystal.

Before discussing candidate materials, we point out that since piezoelectric crystals are anisotropic, the orientation of different crystal cuts can result in significantly different material properties. These include variations in temperature coefficients, frequency stability,

resonator quality factors, and spurious modes. For the example of quartz-type resonators, a comparison of state-of-the-art cuts and their properties can be found in Refs. [133, 134], while Ref. [134] also presents a comparison of the properties of SC- and LD- cut resonators at cryogenic temperatures. Non-contacting electrode designs where the electrodes are not deposited on the resonator itself can further reduce acoustic losses [126, 129, 134].

Piezoelectrics make up a large class of materials; of the 32 possible crystal symmetry classes, 20 exhibit piezoelectricity [135]. Nevertheless, the success of just a handful of piezoelectric crystals, for example quartz and langasite, has meant little previous need to explore the wide arena of potential materials. We provide in Tab. 4.1 an indicative (but not exhaustive) list of promising candidate materials collected from the database of The Materials Project [132]. The properties of these materials are predicted using density functional theory (DFT) and matched to an experimentally determined crystal structure. We searched for crystals with a high concentration of nuclei with large Schiff moments. We have also listed the crystal symmetry group as this can give an indication of whether crystals in that group have been grown for the purposed of resonators in the past, or whether the crystal could be ferroic. For examples of piezoelectric crystal classes and their properties, see Ref. [127].

We expect that the ideal material will be comprised of a single crystal and not be ferromagnetic or ferroelectric, so as to reduce losses associated with movement of domain walls. This is not a requirement however – for instance we consider the reach of PZT in figure 3.8, which is ferroelectric and has a poor quality factor but compensates due to its strong piezoelectric effects, and therefore a large piezoaxionic tensor. A number of optimal, octupole-deformed nuclei are listed at the end of Sec. 3.1.1. In practice, the electronic properties of Eu (europium) and Gd (gadolinium) mean that their compounds are usually ferromagnetic. As a result, Tab. 4.1 mainly contains compounds of U (uranium) and Dy (dysprosium). We have also included crystals containing $^{209}_{83}$Bi and $^{207}_{82}$Pb as examples of high-Z nondeformed nuclei (Sec. 3.1.1).

While DFT can be used to predict the unit cell volume, stiffness, dielectric, and piezoelectric properties of a candidate crystal with good accuracy, the loss angles of the material (the imaginary parts of the crystal tensors) remain critical unknowns that must be determined experimentally. Any resonator's quality factor can nevertheless be further improved by increased purity, choice of cut, surface polishing, use of energy-trapping geometries, and lower temperature. It has been suggested that these measures can reliably improve the quality factor of many crystals by 3–4 orders of magnitude, with Q factors approaching 10^{10} for quartz [126, 129]. While the exact choice of material for our setup is still to be determined, we think the requirements are not overly restrictive, and can hopefully be satisfied by existing crystals. This will require future experimental investigation.

Parameter	Value/Formula	Parameter	Value/Formula
ρ	$12\,\mathrm{g\,cm^{-3}}$	V_c	amu A/ρ
N_{S}	5	$[S_\Phi^{\mathrm{SQ}}]^{1/2}$	$2.5\times10^{-7}\,\Phi_0\,\mathrm{Hz}^{-1/2}$
N_c	10	L_{SQ}	0.1 nH
Z	92	R_{SQ}	$10\,\Omega$
A	200	η_{SQ}	20
S	$5\,\overline{\theta}_a\,e\,\mathrm{fm}^3$	k_i, k_{12}	0.75
n_N	N_{S}/V_c	L_i	$1\,\mu$H
$\mathcal{R}(\nu_s\nu_p)^{-\frac{3}{2}}$	10	C_1, L_1, L_2	variable
$\mathcal{M}_1$	$Z^2\mathcal{R}(\nu_s\nu_p)^{-\frac{3}{2}}a_0^{-4}$	δ_{L_1}	10^{-6}
v^D	$\sqrt{\rho/c_{11}^D}$	δ_{C_1}	0
c_{11}^D	$N_c\alpha/a_0V_c$	δ_c	10^{-9}
β_{11}^S	1/3	δ_β	10^{-6}
h_{11}	$N_c e a_0/V_c$	δ_h	0
ζ_{11}	$(4\pi)^2N_{\mathsf{S}}a_0^2\mathcal{M}\mathsf{S}/V_c$	$\langle\hat{I}_1\rangle$	1
ξ_{11}	$4\pi eN_{\mathsf{S}}\mathcal{M}\mathsf{S}/V_c$	T	1 mK

Table 3.3: Fiducial parameters for an idealized setup assumed throughout this work. The definitions of each symbol can be found in the main text, primarily Sec. 3.1.3 and Sec. 3.2.2.

3.2.2 Signal

In this section, we describe the axion DM signal and how it excites the crystal's electromechanical modes, as well as the entire circuit. We focus on the thickness expander mode, with electric field parallel to the thickness direction (normal to the electrodes). It should be noted that the relevant indices for these modes will change depending on the crystal class; for concreteness, they have been chosen with quartz-type symmetry class 32 in mind. Other possible modes and geometries are discussed in App. A.4, and could be useful for searching for axion signals at lower frequencies and with other crystal classes.

Thickness expander mode of a thin plate

Other than the excitation due to the piezoaxionic effect, the setup and treatment below are analogous to that of Ref. [123, Sec. 3.V.D]. We will take the piezoelectric crystal to be a rectangular prism with side lengths ℓ_i of high aspect ratio (thin plate): $\ell_1 \ll \ell_2, \ell_3$. We are interested in the "fast thickness expander mode": an electro-acoustic wave with both the propagation and displacement in the thickness direction, i.e. wavenumber $\mathbf{k} \propto \hat{\mathbf{x}}_1$

and displacement $\mathbf{u} \propto \hat{\mathbf{x}}_1$. Such a mode only has a normal strain $S_1 \neq 0$, while the other 5 strain components vanish identically. For a high-permittivity dielectric medium with negligible flux leakage, we have that the electric displacements D_2 and D_3 vanish on the minor faces, and because all gradients are in the $\mathbf{x}_1$ direction, they also vanish in the bulk. Furthermore, inside the insulating crystal, we have $\boldsymbol{\nabla} \cdot \mathbf{D} = 0$, so D_1 is spatially uniform. Since the major faces are connected to electrodes in our fiducial setup, we are interested only in the electric field in the thickness direction. The constitutive Eqs. 3.41 and 3.42 therefore reduce to:

$$T_1 = +c_{11}^D \, S_1 - h_{11} D_1 - \xi_{11} \hat{I}_1 \overline{\theta}_a; \tag{3.52}$$

$$E_1 = -h_{11} S_1 + \beta_{11}^S D_1 - \zeta_{11} \hat{I}_1 \overline{\theta}_a. \tag{3.53}$$

The equation of motion for this effectively one-dimensional acoustic mode is $\rho \ddot{u}_1 = \partial_1 T_1 = c_{11}^D \partial_1^2 u_1$, the latter equality following from uniformity of D_1, $\hat{I}_1$, and $\overline{\theta}_a$. The solution to this equation that also satisfies the boundary conditions $T_1 = 0$ at $x_1 = 0, \ell_1$ is:

$$u_1 = \frac{h_{11} D_1 + \xi_{11} \hat{I}_1 \overline{\theta}_a}{\frac{\omega}{v^D} c_{11}^D} \left[\sin \frac{\omega x_1}{v^D} - \tan \frac{\omega \ell_1}{2 v^D} \cos \frac{\omega x_1}{v^D} \right], \tag{3.54}$$

with $v^D = \sqrt{c_{11}^D / \rho}$ the crystal sound speed. Above, the quantities u_1, D_1, and $\overline{\theta}_a$ are assumed to be oscillatory with angular frequency ω; the factors of $e^{i\omega t}$ are not shown.

The voltage difference

$$V = \int_0^{\ell_1} \mathrm{d}x_1 \, E_1 = Z_{\text{crys}} I + V_a \tag{3.55}$$

measured across the electrodes attached to the crystal can be separated in a term equal to the current $I = i\omega \ell_2 \ell_3 D_1$ times the impedance

$$Z_{\text{crys}} = \frac{1}{i\omega C_c} \left[1 - k^2 \frac{2 v^D}{\omega \ell_1} \tan \frac{\omega \ell_1}{2 v^D} \right] \tag{3.56}$$

and the axion-induced voltage

$$V_a = - \left\{ \frac{h_{11} \xi_{11}}{c_{11}^D} \frac{2 v^D}{\omega} \tan \frac{\omega \ell_1}{2 v^D} + \zeta_{11} \ell_1 \right\} \hat{I}_1 \overline{\theta}_a \tag{3.57}$$

proportional to the nuclear spin polarization fraction $\hat{I}_1$ and axion-induced, oscillatory theta angle $\overline{\theta}_a$. In Eq. 3.56, we have defined the clamped capacitance $C_c \equiv \ell_2 \ell_3 / (\ell_1 \beta_{11}^S)$

and the electromechanical coupling factor:

$$k^2 \equiv \frac{h_{11}^2}{c_{11}^D \beta_{11}^S}. \tag{3.58}$$

The axion-induced voltage V_a thus appears *in series* with that of the entire equivalent circuit of the crystal resonator. In the top panel of Fig. 3.4, we plot in black the axion voltage amplitude, V_a, near the crystal's fundamental mechanical frequency $f \simeq f_0 \equiv v^D/2\ell_1$ (vertical black dashed line). (The fundamental resonance frequency is sometimes also referred to as the "anti-resonance frequency", because it maximizes the effective impedance of the unloaded crystal.) We also define the natural resonance frequency $f_{\rm nat} = \omega_{\rm nat}/2\pi$ as the frequency at which the imaginary part of the crystal impedance $Z_{\rm crys}$ vanishes, and is depicted as the vertical gray dashed line in Fig. 3.4. Below the fundamental frequency $f < f_0$, the ξ and ζ contributions (plotted separately in red and blue, respectively) add constructively, while they add destructively above the mechanical resonant frequency. (This cancellation depends on the relative sign between ξ and ζ, which we have taken to be the same here; an opposite relative sign causes a cancellation below the fundamental resonance.) Near the fundamental resonance frequency, the voltage from the piezoaxionic effect dominates, due to the enhancement of the bulk acoustic mode displacement amplitude (Eq. 3.54). This resonant enhancement turns out to be crucial to reach sensitivity to QCD axion DM parameter space.

Losses in the system are introduced through the complex stiffness and impermittivity tensors:

$$c_{11}^D = \mathrm{Re}\left\{c_{11}^D\right\}(1 + i\delta_c), \tag{3.59}$$

$$\beta_{11}^S = \mathrm{Re}\left\{\beta_{11}^S\right\}(1 - i\delta_\beta); \tag{3.60}$$

where the loss angles δ_c and δ_β parametrize the mechanical and dielectric losses in the piezoelectric crystal. (For all quantitative results in this work, the signal response and noise treatment utilizes the above loss angles, not resistive elements such as R_m from Sec. A.3 and shown in Fig. 3.3.) The effective quality factor Q of the piezoelectric plate, as a circuit element referred to the primary circuit, can be calculated as $Q(\omega) =$ (stored energy)/(energy dissipated per cycle). One then finds a frequency-dependent quality factor:

$$Q(\omega) = \frac{1}{\omega C_c \mathrm{Re}\left\{Z_{\rm crys}\right\}}\left[1 + k^2 \frac{1 - \frac{3v^D}{\omega\ell_1}\sin\frac{\omega\ell_1}{v^D}}{1 + \cos\frac{\omega\ell_1}{v^D}}\right]. \tag{3.61}$$

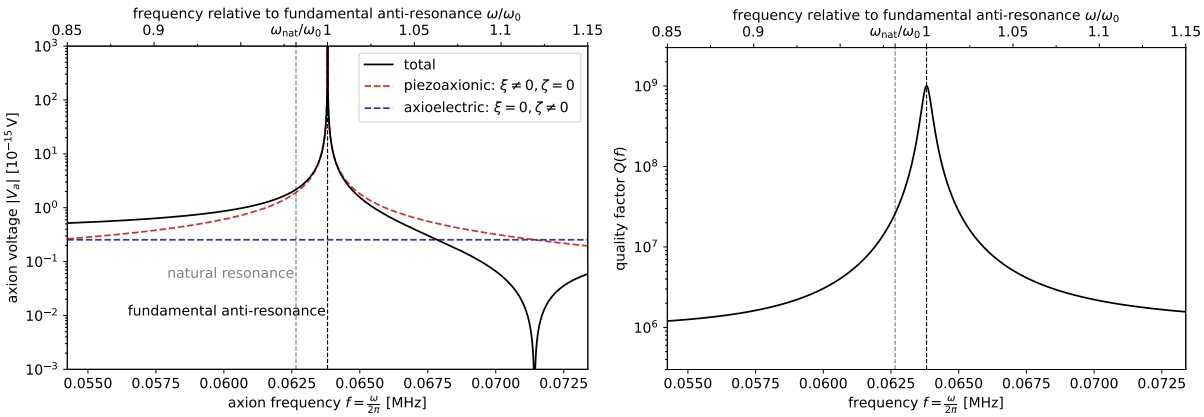

Figure 3.4: *Left:* Axion induced voltage V_a from Eq. 3.57 as function of frequency f for the idealized crystal with parameters shown in Table 3.3. The piezoaxionic (red dashed) and electroaxionic (blue dashed) contributions are plotted separately, giving the total voltage in black. The piezoaxionic effect changes sign, and adds constructively (destructively) to the axioelectric polarizability effect just above (below) the fundamental mechanical resonance frequency (dashed black vertical line), for our choice of relative sign between the piezoaxionic and electroaxionic coefficients ξ and ζ. *Right:* Crystal quality factor Q from Eq. 3.61 as a function of frequency f for the same idealized crystal. The fundamental and the natural resonance frequencies f_0 and $f_{\rm nat}$ are depicted by the black and dashed gray vertical lines, respectively.

The quality factor is plotted in the bottom panel of Fig. 3.4. We observe that, near the fundamental mechanical resonance frequency, the quality factor approaches the inverse of the *mechanical* loss angle δ_c. Far away from this resonance, the quality factor asymptotes to the inverse dielectric loss angle δ_β^{-1}, which is empirically much worse than the mechanical one for most materials. Thermal noise is therefore substantially reduced near the fundamental mechanical frequency of the system compared to that of a purely electrical resonator (Sec. 3.2.3).

Readout circuit components

Having described the signal and response of the piezoelectric crystal, we now turn to the other circuit components used for the readout of the signal due to the axion voltage of Eq. 3.57, which are qualitatively similar to that of other experimental setups [130, 136–139]. The total impedance $Z_{\rm tot}$ of the circuit loop containing the piezoelectric crystal, which we shall refer to as the input circuit, is:

$$Z_{\rm tot} = Z_{\rm crys} + \frac{1}{i\omega C_1} + i\omega L_1 + \Delta Z_{\rm BI} \tag{3.62}$$

The second and third terms in $Z_{\rm tot}$ are the impedances of the capacitor with capacitance C_1, and inductor with self-inductance L_1, respectively. These two impedances serves as the main loads of the resonator, and can be used to control the setup's resonant frequency $f_{\rm res} = \omega_{\rm res}/2\pi$, i.e. the frequency at which $\mathrm{Im}\{Z_{\rm tot}\}$ vanishes, as shown in Fig. 3.5. As discussed in Sec. 3.2.4, changing L_1 or C_1 is one of the methods that can be used to shift the resonance frequency of the circuit and scan (continuously) over possible axion masses. The transformer circuit and the SQUID contribute a fourth term to $Z_{\rm tot}$ in Eq. 3.62, the back impedance [69]:

$$\Delta Z_{\rm BI} = \frac{\omega^2 M_{12}^2}{i\omega L_2 + i\omega L_i + \omega^2 M_i^2 \left(\frac{1}{i\omega \mathcal{L}^r} + \frac{1}{\mathcal{R}^r}\right)}, \tag{3.63}$$

where $\mathcal{L}^r$ and $\mathcal{R}^r$ are the reduced dynamical inductance and resistance of the SQUID, respectively [140]. This back impedance is typically negligible under optimal operating conditions.

The ultimate readout observable is the flux $\Phi_{\rm SQ}$ through the SQUID:

$$\Phi_{\rm SQ} = \frac{I\, M_{12}\, M_i}{L_i + L_2}, \tag{3.64}$$

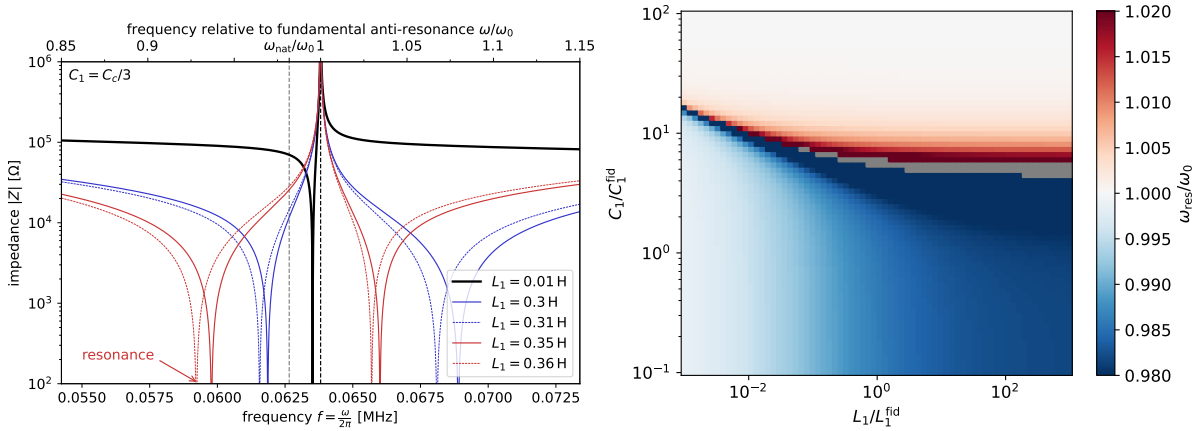

Figure 3.5: *Left:* Total impedance as referred to the input circuit of Fig. 3.3, for fixed $C_1 = C_c/3$ and different values of the transformer inductance L_1. For small $L_1 = 0.01\,\mathrm{mH}$ (black), the resonance frequency f_{res} below the fundamental mechanical resonance angular frequency f_0 (black dashed line) is shifted up above the natural resonance frequency f_{nat} (gray dashed line) due to the finite value of C_1. For increasing L_1, the resonance frequency is tuned downwards, as indicated by the blue lines for $L_1 = 12.0, 12.5\,\mathrm{mH}$. For yet larger inductances $L_1 = 16.0, 16.5\,\mathrm{mH}$, the resonance frequency associated with the mode *above* the fundamental mechanical resonance approaches f_0 (red lines). *Right:* Resonance angular frequency ω_{res} (in units of ω_0) as a function of L_1 and C_1. Blue (red) colors indicate the resonant branch below (above) ω_0, like in the top panel. For both panels, the parameters of the idealized crystal used are given in Tab. 3.3.

where I is the input circuit current, which receives an additive contribution I_a due to the axion voltage V_a from Eq. 3.57:

$$I_a = \frac{V_a}{Z_{\rm tot}}. \tag{3.65}$$

We take the mutual inductances to have fixed coupling coefficients $k_{12} \equiv M_{12}/\sqrt{L_1 L_2}$ and $k_i = M_i/\sqrt{L_i L_{\rm SQ}}$, respectively. While the flux through the SQUID (from the axion voltage) is maximized when $L_2 = L_i$, it is not generally optimal in view of back action noise (see Sec. 3.2.3). We note that the readout signal, for fixed axion voltage, is enhanced for two reasons in the above setup. Firstly, the axion signal current from Eq. 3.65 is enhanced on resonance (when $|\mathrm{Im}\{Z_{\rm tot}\}|$ is small). Secondly, the transformer current steps up the current in the transformer circuit by a factor of $\mathcal{O}(\sqrt{L_1/L_2})$, resulting in a corresponding enhancement of the flux through the SQUID.

3.2.3 Backgrounds

In Sec. 3.2.2, we computed how the axion DM background sourced the signal voltage V_a in the input circuit, and how this propagated to a flux $\Phi_{\rm SQ}$ through the SQUID. In this section, we will outline the main backgrounds that compete with this signal. These noise sources can be divided into three categories: thermal noise due to dissipative circuit elements (Sec. 3.2.3), SQUID flux noise (Sec. 3.2.3), and spin projection noise, i.e. magnetization noise (Sec. 3.2.3). For direct comparison to the axion voltage V_a, we quantify all noise sources in terms of their equivalent voltage noise spectral densities:

$$S_V^{\rm tot} = S_V^{\rm th} + S_V^{\rm SQ} + S_V^{\rm spin} \tag{3.66}$$

as referred to the input circuit, and assume a noise model with vanishing cross-correlations between voltage and current (see Ref. [141] for more discussion). We also comment on non-thermal vibration or seismic noise (Sec. 3.2.3), as well the limitations in cryogenic cooling arising from the possible use of metastable nuclei such as $^{235}_{92}$U and $^{237}_{93}$Np (Sec. 3.2.3).

Thermal Noise

Thermal noise due to the lossy circuit elements is the primary source of noise on and near resonance. Its equivalent voltage noise spectral density $S_V^{\rm th}$ can be written as:

$$S_V^{\rm th} = 4T\,\mathrm{Re}\,\{Z_{\rm tot}\} = S_V^{\rm crys} + S_V^{C_1} + S_V^{L_1} + S_V^{\rm BI}, \tag{3.67}$$

where T is the thermodynamic temperature, and the breakdown in terms of different thermal noise sources is the same as in the sum of Eq. 3.62. The thermal noise is proportional to the real part of the impedance, and thus to the loss angles δ_c and δ_β for the crystal circuit element, δ_{C_1} for the capacitor with complex capacitance $C_1 = |C_1|(1 + i\delta_{C_1})$, and δ_{L_1} for the inductor with complex inductance $L_1 = |L_1|(1 - i\delta_{L_1})$. The thermal voltage noise from the SQUID back impedance is linearly proportional to $\mathcal{R}^r$. In the top panel of Fig. 3.6, we plot representative values for the thermal voltage noise S_V^{crys} of the crystal (blue), as well as $S_V^{L_1}$ of the inductor (green). The contribution S_V^{BI} of the back-action impedance of the SQUID readout system is negligible, and we assume the capacitance has a negligible loss angle (compared to that of C_c). Fiducial parameters for the setup are given in Tab. 3.3. The combined thermal noise is seen to dominate the total noise (black) on resonance. The total noise off-resonance is dominated by the SQUID noise to which we turn next.

SQUID Noise

The voltage noise spectral density for the SQUID amplifier consists of current imprecision noise S_I^{flux} (due to the finite precision with which the flux can be read out) and back action noise S_V^{back}:

$$S_{V,\text{tot}}^{\text{SQ}} = |Z_{\text{tot}}|^2 S_I^{\text{flux}} + S_V^{\text{back}}. \tag{3.68}$$

As demonstrated in Ref. [141, Apps. E, F], under operating conditions with vanishing cross-correlated noise, these two noise sources are related by:

$$S_V^{\text{back}} = \frac{\eta_{\text{SQ}}^2 \omega^2}{S_I^{\text{flux}}}, \tag{3.69}$$

where $\eta_{\text{SQ}} \geq 1$ determines the noise temperature $T_N^{\text{SQ}} = \eta_{\text{SQ}}\omega/\pi$ at each angular frequency ω, and saturation of the inequality is achieved at the standard quantum limit (SQL). We take $\eta_{\text{SQ}} = 20$ as a fiducial SQUID sensitivity, a value that has already been reached in a read-out circuit of a kHz-frequency mechanical resonator [142].

The imprecision noise of the SQUID is related to the finite flux noise spectral density S_Φ^{SQ}, and quantifies how small a flux Φ_{SQ} can be read out by the device. Translating this flux noise to an equivalent current noise in the input circuit gives:

$$S_I^{\text{flux}} = \frac{(L_i + L_2)^2}{k_{12}^2 k_i^2 L_1 L_2 L_i L_{\text{SQ}}} S_\Phi^{\text{SQ}}. \tag{3.70}$$

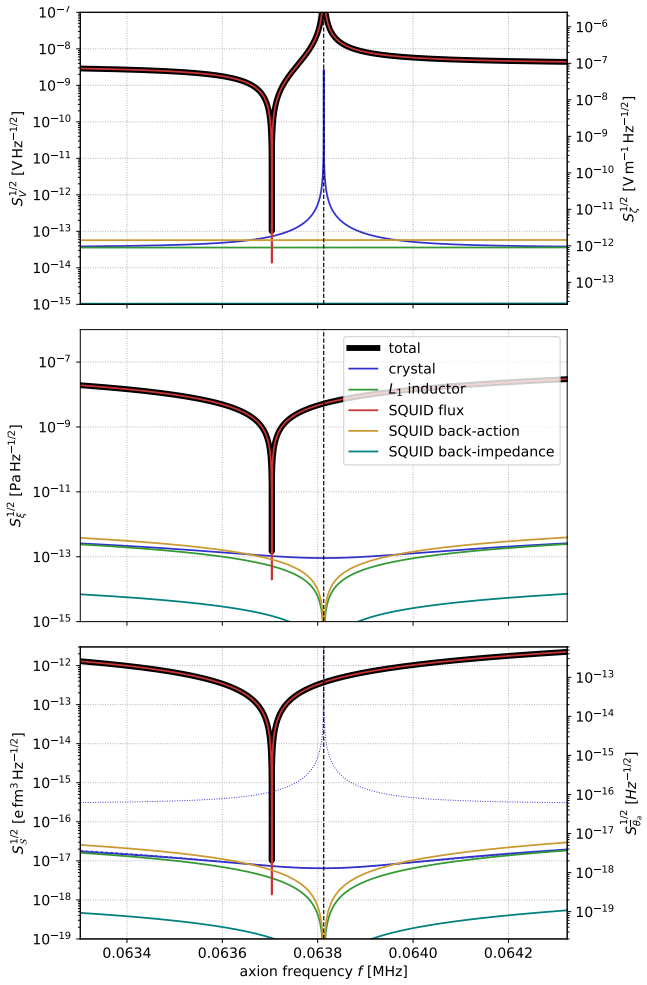

Figure 3.6: Amplitude spectral densities of all noise sources considered in the experimental setup with a crystal of dimensions $\ell_1 = 4\,\mathrm{cm}$ and $\ell_{2,3} = 40\,\mathrm{cm}$, variable capacitance $C_1 = C_c/10$, and variable inductance $L_1 = 0.06\,\mathrm{H}$. All other parameters are the fiducial ones from Tab. 3.3. The top panel depicts noise sources expressed as equivalent voltage noise amplitudes $S_V^{1/2}$ of Eqs. 3.66, 3.67, and 3.70, as referred to in the input circuit of Fig. 3.3. Via Eq. 3.57, they can be expressed as effective noise amplitudes for $\zeta_{11}\overline{\theta}_a$ (right axis of top panel) and $\xi_{11}\overline{\theta}_a$ (middle panel). In the bottom panel, they are shown as effective noise amplitudes for the Schiff moment S (left axis) and the QCD $\overline{\theta}_a$ angle (right axis), via Eqs. 3.43 and 3.44.

As mentioned in Sec. 3.2.2, the value of L_2 that maximizes the flux through the SQUID at fixed coupling coefficients k_{12} and k_i (and thus minimizes $S_I^{\rm flux}$) is $L_2 = L_i$. However, this flux maximization also maximizes the back action noise, cfr. Eq. 3.69, and is typically suboptimal. Ref. [141][App. F] found the best operating point for any search for a near-monochromatic signal with log-uniform priors on its frequency; in the limit of $T \gg \omega$, which applies to our low-frequency setup, this corresponds to:

$$S_V^{\rm back} = 2T\,{\rm Re}\{Z_{\rm tot}\}, \tag{3.71}$$

which we take to hold on resonance. For any resonance frequency of our system, we try to satisfy Eq. 3.71 by tuning the value of L_2. This could also be improved in future by using a readout that can perform back-action evading measurements, for example [143].

The energy resolution of an optimized SQUID is limited by the uncertainty principle to satisfy the inequality [144]:

$$\frac{S_\Phi^{\rm SQ}}{2L_{\rm SQ}} \gtrsim \pi, \tag{3.72}$$

a limit that has been nearly saturated within a factor of $\mathcal{O}(1)$ by many groups [145]. For the purposes of our projections, we assume fiducial SQUID parameters from reference [142] of $[S_\Phi^{\rm SQ}]^{1/2} = 2.5\times10^{-7}\,\Phi_0\,{\rm Hz}^{-1/2}$, $L_{\rm SQ} = 0.1\,{\rm nH}$ and $L_i = 1\,\mu{\rm H}$, where $\Phi_0 = \pi/e$ is the magnetic flux quantum. The SQUID's energy resolution is however not the sensitivity-limiting factor, which is instead the balancing of back impedance and back action and imprecision noise of Eqs. 3.63, 3.69 and 3.70.

In the top panel of Fig. 3.6, we plot the equivalent imprecision voltage noise of the SQUID flux noise in red (the first term in Eq. 3.70); off-resonance, imprecision noise is the sensitivity-limiting factor. In gold, we plot the corresponding back action voltage noise at the optimal operating point of Eq. 3.71, which is always of order the thermal noise from the other circuit components.

Spin Noise

For a crystal to exhibit the piezoaxionic effect due to the irreducible coupling of QCD axion DM, it needs to be populated by a high density of nuclear spins, whose fluctuations—spin projection noise or magnetization noise—can source an effective noise voltage in the circuit. The effective magnetic field noise spectral density of these spin fluctuations is [95]:

$$S_B^{\rm spin} = \frac{\mu_N^2 n_N}{8\ell_1\ell_2\ell_3}\frac{T_2}{1+T_2^2(\omega-\mu_N B_0)^2}, \tag{3.73}$$

where μ_N, n_N, and T_2 are the nuclear magnetic moment, the nuclear spin density, and the transverse spin relaxation time, respectively. There is generically a static magnetic field B_0 present in the material, from an externally applied field and/or from the aligned nuclear spins (unless they cancel each other). The resulting voltage noise spectral density into the input circuit can then be estimated as:

$$S_V^{\text{spin}} = \omega^2 \ell_1^2 C_c^2 S_B^{\text{spin}} \simeq \frac{\ell_2 \ell_3}{8\ell_1 \left(\beta_{11}^S\right)^2} \frac{\mu_N^2 n_N}{T_2}, \tag{3.74}$$

where we have assumed $\omega \gg \mu_N B_0$. The voltage amplitude spectral density of these spin fluctuations evaluates to $[S_V^{\text{spin}}]^{1/2} \approx 1.0 \times 10^{-16}\,\text{V}\,\text{Hz}^{-1/2}$ for a magnetic moment equal to a nuclear magneton $\mu_N \equiv e/2m_p$, a typical solid-state transverse spin relaxation time $T_2 = 10^{-3}\,\text{s}$, and otherwise the same parameters as used in Fig. 3.6; this value is far below the other noise sources depicted in the top panel.

Magnetization noise can also arise from fluctuating magnetic impurities in the crystal. The electron impurity spin noise is similar to the one shown above, with μ_N substituted by the effective electron magnetic moment $\mu_e \sim \mu_B \equiv e/2m_e$ and correspondingly shorter transverse relaxation times $T_2' \sim 10^{-3}\,T_2$, since the electrons interact $\mu_e/\mu_N \sim 10^3$ times more strongly with their environment. Magnetic impurity concentrations as low as 1 part per billion have previously been reported [146]. We find this source of noise to be subdominant to nuclear magnetization noise as long as magnetic impurities are kept to below 1 part per million, and certainly below the other noise sources plotted in Fig. 3.6, even for much higher concentrations. Magnetization noise would however become the dominant source of broadband noise for any version of our proposed experiment with order-unity polarization fraction of *electron* spins. For such magnetically ordered materials, magnetomechanical effects such as magnetostriction [147] and piezomagnetism [123, Ch. VII]—lattice strain/stress proportional to magnetic fields—must also be considered in the noise budget, but are highly suppressed for the nonmagnetic crystals (with only nuclear spin polarization) considered in this work.

Vibration Noise

Non-thermal, external sources of vibration, such as those from seismic noise or human activity must be isolated from the crystal's acoustic modes. Around $f \sim$ kHz frequencies, the displacement noise amplitude spectral density $S_{\text{disp}}^{1/2}$ is empirically found to scale as [148]:

$$S_{\text{disp}}^{1/2} \sim \beta\, 10^{-13}\,\text{m}\,\text{Hz}^{-1/2} \left(\frac{\text{kHz}}{f}\right)^2 \tag{3.75}$$

with β a parameter ranging from 1 to 10 depending on the amount of surrounding human activity. In order to keep this vibration noise down to an equivalent strain noise amplitude of $S_{\rm strain}^{1/2} \sim 10^{-25}\,{\rm Hz}^{-1/2}$—as needed to detect the piezoaxionic effect from QCD axion DM (see Eq. 3.51)—in a crystal of thickness $\ell \sim$ cm at $f \sim$ MHz, one requires a vibration attenuation of at least $-160\,$dB. In other words, the rms displacement of the crystal's major surfaces (off-resonance) needs to be suppressed by at least 8 orders of magnitude compared to the rms absolute displacement of the environment in the same frequency band. Such levels of vibration mitigation are well within the $-240\,$dB attenuation levels achieved by the AURIGA collaboration at $f \sim 900\,$Hz [149].

Cooling Limitations

In order to achieve our target sensitivity, a crystal containing a high concentration of nuclei with octupole-enhanced Schiff moments needs to be cooled to cryogenic temperatures. Some candidate nuclear isotopes, such as ${}^{235}_{92}$U and ${}^{237}_{93}$Np, are radioactive. The decay heat [150] from these metastable nuclei presents a challenge, as the cooling power of dilution refrigerators is limited.

A dilution refrigerator's cooling power $\dot{Q}$ depends chiefly on the target temperature T and the ^{3}He flow rate $\dot{n}$ [151]:

$$\dot{Q} \approx 8.4\,\mu{\rm W}\,\left(\frac{\dot{n}}{10^{-3}\,{\rm mol/s}}\right)\left(\frac{T}{10\,{\rm mK}}\right)^2, \tag{3.76}$$

with a (high) fiducial flow rate indicated in brackets.

The largest crystal size $4 \times 40 \times 40$ cm^3 under consideration, with a density of $12\,{\rm g/cm^3}$, contains 64 kg of heavy (and potentially radioactive) nuclei, if they make up $10\,{\rm g/cm^3}$ in terms of mass density. The decay heating power of e.g. ${}^{235}_{92}$U is approximately $60\,\mu{\rm W/kg}$ [150], which would preclude reaching temperatures below 200 mK. This problem is even more severe for ${}^{237}_{93}$Np, which has a decay heating power of $0.02\,{\rm W/kg}$.

This decay heat makes the presence of metastable nuclei in a cryogenic environment challenging, if not prohibitive. As noted in Sec. 3.1.1, there are several *stable* nuclear isotopes with octupole-enhanced Schiff moments which do not suffer from this problem. Finally, it may also be possible to cool a single acoustic mode below the thermodynamic temperature of the crystal via optomechanical methods [152]. Such futuristic experimental directions are outside the scope of this work.

3.2.4 Sensitivity

In Secs. 3.2.2 and 3.2.3, we calculated the axion signal voltage V_a (Eq. 3.57 and Fig. 3.4) and the voltage noise spectral density $S_V^{\rm tot}$ (Eq. 3.66 and Fig. 3.6), respectively, as referred to the input circuit. We will now synthesize these results to compute the sensitivity of our proposed experiment.

After one "shot" of time $t_{\rm shot}$, which we assume to be larger than the coherence time $\tau_{\rm coh}$ of the axion DM signal in Eq. 2.19, the signal-to-noise ratio (SNR) is:

$$\mathrm{SNR}_{\rm shot} = \sqrt{\frac{|V_a|^2\sqrt{t_{\rm shot}\tau_{\rm coh}}}{S_V^{\rm tot}}}, \tag{3.77}$$

where $S_V^{\rm tot}$ is to be evaluated at an angular frequency of $\omega = m_a$. The SNR of a single shot is largest whenever $|V_a|^2/S_V^{\rm tot}$ is largest, which typically only occurs for axion frequencies $f = m_a/2\pi$ in a small bandwidth around the resonance frequencies $f_{\rm res} = \omega_{\rm res}/2\pi$ of the complete circuit. This is shown in Fig. 3.7, which assumes a crystal of size $4 \times 40 \times 40$ cm^3 with parameters given in Table 3.3. The red curve is a $\mathrm{SNR}_{\rm shot} = 1$ contour expressed in terms of $\overline{\theta}_a$ sensitivity as a function of axion frequency. In addition to noise suppression, whenever a resonance is close to a fundamental resonance frequency of the crystal (the vertical black dashed line in Fig. 3.7), the sensitivity is enhanced further due to the increase of the axion voltage signal (see Fig. 3.4 and also the bottom panel of Fig. 3.6).

The narrow instantaneous bandwidth of the setup necessitates a scanning strategy to achieve sensitivity to a broad range of axion masses. Our suggested strategy in this paper is to dial the resonance frequencies by changing the electric loads, namely the readout circuit's capacitance C_1 and inductance L_1 between each shot. For the resonance peak below the mechanical resonance, we take $C_1 = 10\,|C_c|$, and $C_1 = 0.1\,|C_c|$ for the resonance peak above the mechanical resonance frequency. We suggest scanning the resonance frequency with a large number $N = 10^4$ shots over regularly spaced steps in the range of $[2\omega_{\rm nat} - \omega_0, 3\omega_0 - 2\omega_{\rm nat}]$ by changing the inductance L_1 in incremental steps. The value of the inductance needed lies in a range of a few orders of magnitude around the typical impedance-matched value of $|L_1| \sim 1/(\omega_0^2|C_c|)$. The total SNR of all shots is computed as:

$$\mathrm{SNR}_{\rm tot} = \sum_{\rm shots} \left(\mathrm{SNR}_{\rm shot}^{-4}\right)^{-1/4}. \tag{3.78}$$

The isocontour $\mathrm{SNR}_{\rm tot} = 1$ as a result of this procedure is plotted as the red line of Fig. 3.7.

Figure 3.8 shows in blue the forecasted sensitivity for 13 crystals with thicknesses ℓ_1 logarithmically spaced between 4 cm and 2 cm and an aspect ratio of 10 (i.e. transverse sizes

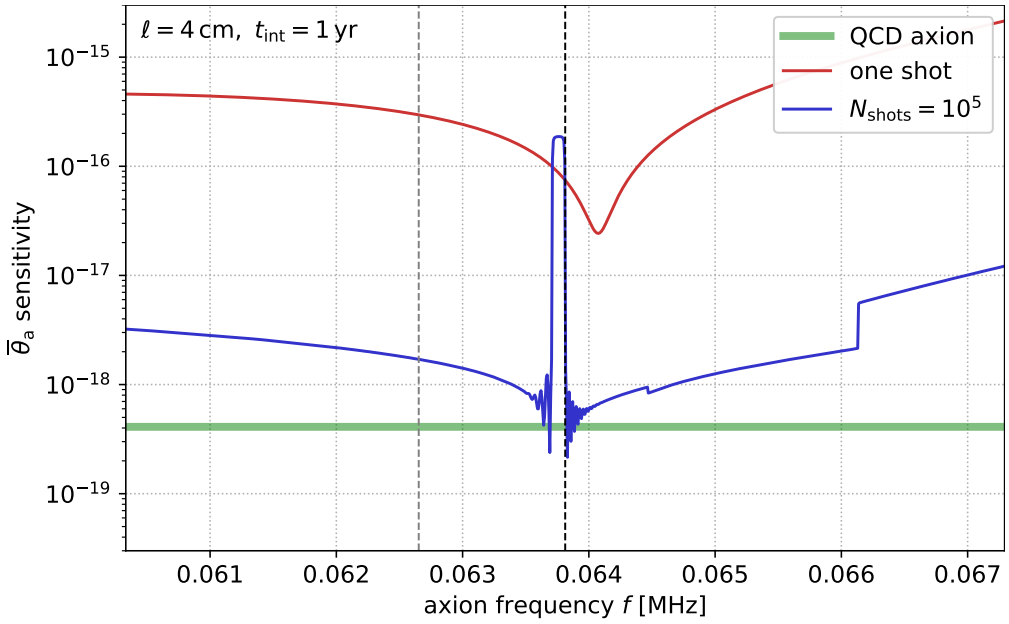

Figure 3.7: Sensitivity to an oscillatory theta angle $\bar{\theta}_a$ as a function of frequency for a single shot (red line) and for a scan around the mechanical resonance frequency of the first acoustic thickness expander mode of an idealized crystal with fiducial parameters given by Tab. 3.3. The green line shows the prediction for QCD axion DM.

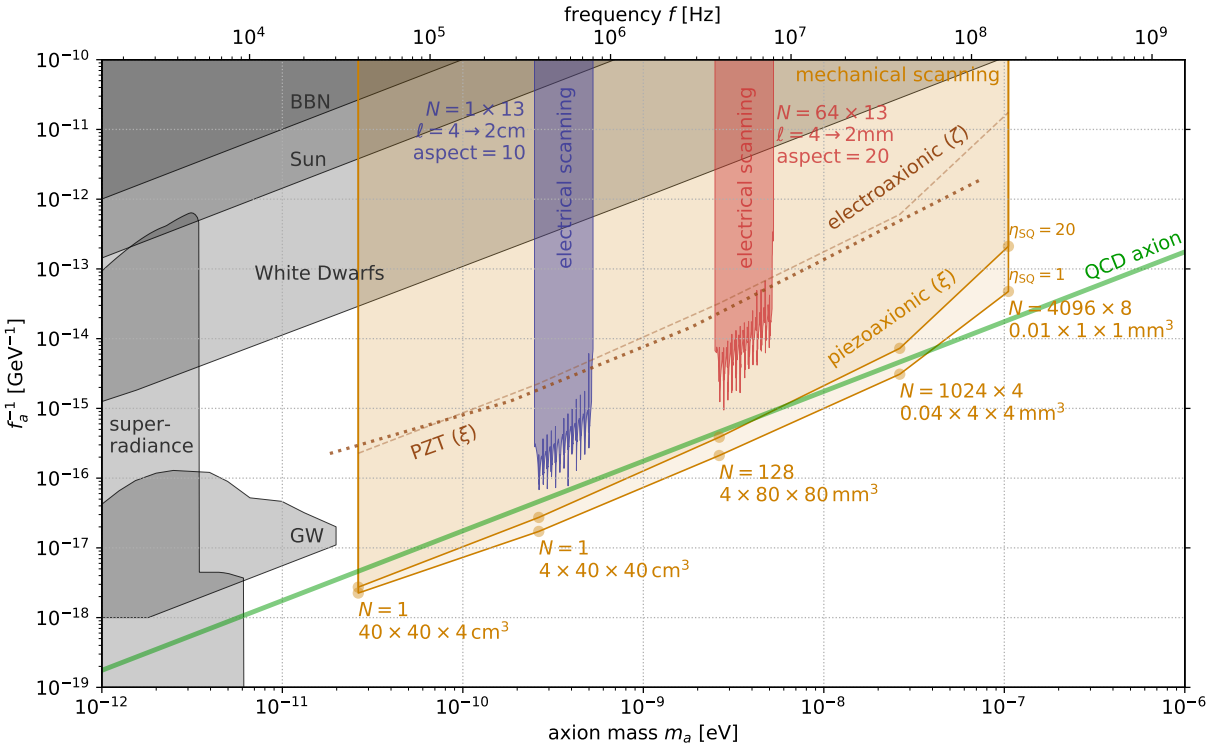

Figure 3.8: Axion parameter space probed by the setup described in Sec. 3.2 and parameters given in Tab. 3.3 as a function of the axion decay constant f_a (inverse, vertical axis) and the axion mass m_a (the top axis also indicates the corresponding frequency f). The blue and red shaded regions show the reach ($\mathrm{SNR}_{\mathrm{tot}} = 1$ with Eq. 3.78) by scanning electrically around the first acoustic modes of a series of crystals with 13 different thicknesses. The gold region outlines the ultimate reach assuming mechanical scanning of the frequency for the parameters indicated. The ultimate reach, limited by a combination of SQUID noise and the crystal thermal noise, is shown for different values of η_{SQ}, the parameter indicating how close the SQUID operates to the quantum limit (see Sec. 3.2.3 and Sec. 3.2.4 for more details).Similarly, the sensitivity achieved by the electroaxionic effect alone is outlined by the brown dashed line. The QCD axion relation between the mass and the decay constant (Eq. 1.2) is shown in green. The gray shaded regions are disfavored from BH superradiance [41], BBN [153], the structure of the Sun [70], white dwarfs [154], and neutron star binary mergers [155]. The brown dotted line is the projected sensitivity for commercially available PZT crystals with $\eta_{SQ} = 1$, assuming an $\mathcal{O}(1)$ concentration of $^{207}_{82}$Pb
.

$\ell_2 = \ell_3 = 40 \to 20\,\mathrm{cm}$), for a total integration time of $t_{\rm int} = 10\,\mathrm{yr}$, and other parameters matching those of Fig. 3.7 and Tab. 3.3. Sensitivity to the QCD axion can be reached for such a setup over an octave in axion masses. The red region is a scaled-down version of the setup with 13 different values of $\ell_1 = 4 \to 2\,\mathrm{mm}$, 64 identical crystals hooked up in series, and an aspect ratio of $\ell_{2,3}/\ell_1 = 20$.

The gold region in Fig. 3.8 is the parameter space that can plausibly be covered by setups similar to those previously described, assuming *mechanical scanning* of frequency, which is not discussed in detail in this work. Mechanical scanning would allow taking full advantage of the high Q factor around the resonance frequency. This plotted region is constructed by interpolating between the on-resonance sensitivity for 4 setups (indicated by gold circles) with dimensions $\ell_1 \times \ell_2 \times \ell_3$ equal to $40 \times 40 \times 4\,\mathrm{cm}^3$, $4 \times 40 \times 40\,\mathrm{cm}^3$, $4 \times 40 \times 40\,\mathrm{mm}^3$, and $0.01 \times 1 \times 1\,\mathrm{mm}^3$, respectively. The third and fourth fiducial setups assume a large number of crystals in series and parallel at any one time, namely 64×1 and $512 \times 32 = 8192$. For each setup, we take $C_1 = 0.1\,|C_c|$ and $L_1 = (\omega_0^2 |C_c|)^{-1}$. To cover an octave within a 10-year integration time, the shot time is assumed to be $t_{\rm shot} = t_{\rm int}/(Q_{\rm res} \ln 2)$ where $Q_{\rm res} \equiv \omega_{\rm res}/\Delta\omega$ is the inverse fractional bandwidth, and $\Delta\omega$ is the range of ω over which $S(\omega) < 4S(\omega_{\rm res})$. With those assumptions, sensitivity to the QCD axion may be attained over a mass range of $m_a \in [10^{-11}\ \mathrm{eV},\ 10^{-8}\ \mathrm{eV}]$ for a fiducial SQUID noise temperature determined by $\eta_{\rm SQ} = 20$, and over $[10^{-11}\ \mathrm{eV},\ 10^{-7}\ \mathrm{eV}]$ for a quantum-limited amplifier ($\eta_{\rm SQ} = 1$). Also shown is the reach due to the electroaxionic effect (dashed brown), which is weaker. The superiority of the piezoaxionic effect is due to the enhancement of the axion-induced voltage on resonance and the large Q factor associated with mechanical oscillations of the crystal. The brown dotted line in figure 3.8 corresponds to the reach of the piezoaxionic effect using commercially available PZT-7A [122] grown with a 100% abundance of the lead isotope ${}^{207}_{82}\mathrm{Pb}$, assuming the same experimental setup and a quantum-limited amplifier ($\eta_{\rm SQ} = 1$). The mechanical and electrical loss angles of the crystal have been taken conservatively to be of the order of 10^{-3}.

The green line in Fig. 3.8 shows the QCD axion prediction, while gray regions indicate previously known constraints. Black-hole (BH) superradiance [34, 156] is a process wherein the spontaneous/stimulated production of axions can extract a large amount of angular momentum from BHs; we take the updated constraints from Ref. [41], outlining parameter space that is inconsistent with spin measurements on five known BHs in x-ray binary systems. (These are lower bounds on f_a, as axion self-interactions can quench this process.) At sufficiently small values of f_a, the value of $\overline{\theta}_a$ could be so large that the neutron-proton mass difference at neutron freeze-out alters big-bang nucleosynthesis (BBN) predictions significantly [153]. The region labeled "Sun" is excluded by direct measurements of the Sun, as the in-medium reduction of the axion potential will generically destabilize the

axion to $|\overline{\theta}_a| \sim \pi$ at those small values of f_a [70]. A similar destabilization can occur much more easily (for much larger f_a) in neutron stars, with the sourced axion field altering short-range forces within a double-neutron-star binary system—shown are corresponding gravitational-wave (GW) constraints from Ref. [155]. Near nuclear saturation densities, as exhibited by supernova remnants and cores of neutron stars (e.g. SN1987A and Cassiopeia A, respectively), axion production through the nuclear coupling is very efficient, leading to a bound of order $f_a \gtrsim 10^8\,\mathrm{GeV}$ (outside the plot range in Fig. 3.8), though the precise value of this bound is not yet settled [55, §91]. As discussed in Sec. 2.3.1, any bounds (and also our projections) above the QCD axion line prediction of Fig. 3.8 are model-dependent due to the fine-tuning needed in this part of the parameter space.

In summary, Fig. 3.8 illustrates how the piezoaxionic effect can be used to search for the irreducible coupling of QCD axion DM. For other setups and proposals to search for this coupling, see Refs. [68, 95, 157–159]. Because of derivative suppression, this is also a challenging mass range for detection concepts that search for other couplings of QCD axion DM [68, 160–163]. The parameters of Tab. 3.3 should be taken as indicative, with significant research and development needed to achieve the sensitivity curves of Fig. 3.8 in practice. Nevertheless, we believe our idealized forecast demonstrates that the piezoaxionic effect can be a powerful probe of QCD axion DM.

3.3 Other Axion Couplings

In Secs. 3.1 and 3.2, we have focused on the irreducible coupling of QCD axion DM in Eq. 2.13, and the resulting P- and T-violating effects. Generic axion-like particles (ALP), as well as the QCD axion [38], can have shift-symmetric couplings to fermions and photons:

$$\mathcal{L} \supset \frac{G_{a\gamma\gamma}}{4} a F_{\mu\nu} \widetilde{F}^{\mu\nu} - \sum_{f=p,n,e} \frac{G_{aff}}{2} \partial_\mu a \overline{\psi}_f \gamma^\mu \gamma^5 \psi_f, \tag{3.79}$$

with $\widetilde{F}^{\mu\nu} \equiv \epsilon^{\mu\nu\rho\sigma} F_{\rho\sigma}/2$. The shift symmetry [$a \to a + \text{constant}$] of the resulting action implies that all physical effects from these couplings are proportional to *derivatives* of the axion field, i.e. $\partial_\mu a$, where now a can be a generic ALP or the QCD axion. We do not consider in detail the effects from the axion-photon coupling in this work, as our preliminary calculations indicate they are numerically small, and electrical resonator setups such as those of Refs. [136–138, 160, 164] are better suited.

For the axion-fermion couplings, one finds the following single-particle Hamiltonian:

$$H_f = \frac{G_{aff}}{2}\partial_\mu a \gamma^0\gamma^\mu\gamma^5 \simeq -\frac{G_{aff}}{2}\boldsymbol{\sigma}_f \cdot \left[\boldsymbol{\nabla} a + \dot{a}\frac{\mathbf{p}_f}{m_f}\right], \tag{3.80}$$

with $\boldsymbol{\sigma}_f$, $\mathbf{p}_f$, and m_f the spin, momentum, and mass of the fermion f, respectively. The nonrelativistic limit was taken in the second equality. The "axion wind" interaction, the P-even and T-odd operator proportional to $\boldsymbol{\nabla} a$ (and thus the axion velocity) in Eq. 3.80, has been proposed to search for ALPs and the QCD axion, by detecting changes in transverse magnetization from precessing nuclear [89] and electron spins [165].

In a parity violating medium, the P-odd and T-even operator proportional to $\dot{a}$ in Eq. 3.80, generically contributes to the internal energy density U of Eq. 3.38 an additive correction:

$$U \supset \sum_{e}^{\text{unit cell}} \frac{\langle H_e\rangle}{V_c} = -\frac{G_{aee}\dot{a}}{2V_c}\sum_e \left\langle \psi_e \middle| \frac{\mathbf{p}_e\cdot\boldsymbol{\sigma}_e}{m_e} \middle| \psi_e \right\rangle, \tag{3.81}$$

since there is no symmetry that forbids such a nonzero contribution, in analogy to the piezoelectric effect. The axion-nucleon coupling G_{aNN} yields numerically small effects in what follows, since nuclear contributions to the crystal lattice dynamics are suppressed by positive powers of m_e/m_N and/or R_0/a_0, so we focus on electronic contributions from hereon; the sum in Eq. 3.81 is over all electrons in the unit cell. Note that since the operator in Eq. 3.81 is T-even, the electrons need *not* be spin-polarized or unpaired, which is advantageous from the point of view spin-noise backgrounds (Sec. 3.2.3). The internal energy density correction of Eq. 3.81 results in corresponding additive changes to the constitutive equations for the stress and electric field (e.g. Eqs. 3.41 and 3.42):

$$T_n = \frac{\partial U}{\partial S_n} \supset -\frac{G_{aee}\dot{a}}{2}\theta_n \equiv -\frac{G_{aee}\dot{a}}{2}\frac{\alpha N_c}{V_c}\widetilde{\theta}_n, \tag{3.82}$$

$$E_n = \frac{\partial U}{\partial D_n} \supset -\frac{G_{aee}\dot{a}}{2}\eta_n \equiv -\frac{G_{aee}\dot{a}}{2}\frac{\alpha N_c}{V_c}\frac{e a_0^2}{\alpha}\widetilde{\eta}_n; \tag{3.83}$$

where by NDA, the 2-tensors $\widetilde{\theta}_n$ and $\widetilde{\eta}_n$ should be of order unity. In Eqs. 3.82 and 3.83, we estimate that there are N_c number of valence electrons, and that each matrix element in Eq. 3.81 is $\mathcal{O}(\alpha)$. Unlike in the case of the piezoaxionic and electroaxionic effects from a Schiff moment, where only $j = 1/2$ electrons around a high-Z nucleus contribute, here *all* valence electrons participate.

In Fig. 3.9, we show that with the same setup as described in the previous section, one is also sensitive to the axion-electron coupling of ALP DM. (The sensitivity calculation

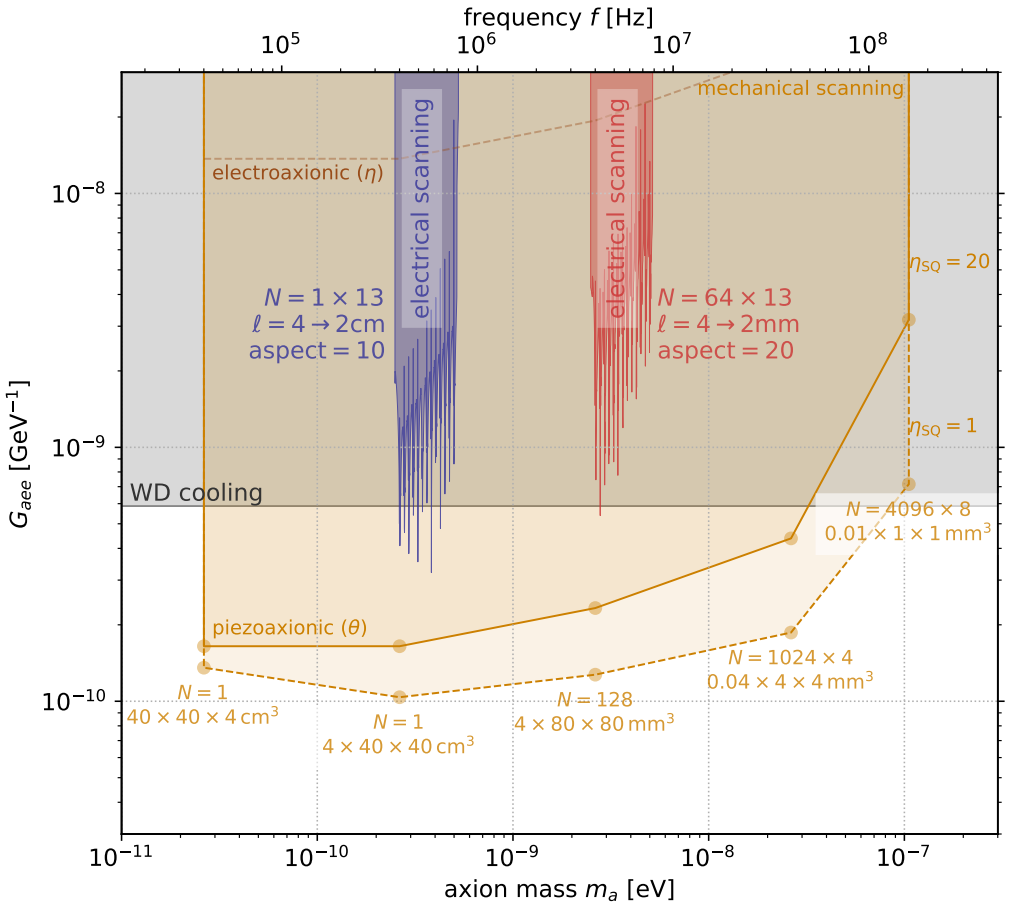

Figure 3.9: Sensitivity to the derivative axion-electron coupling G_{aee} of Eq. 3.79 as a function of mass m_a of the axion-like particle. The setup and parameters are the same as in Fig. 3.8, with the additional assumption of $\widetilde{\theta}_1 = \widetilde{\eta}_1 = 1$ in Eqs. 3.82 and 3.83. The gray region indicates couplings strongly disfavored by cooling of white dwarf (WD) stars [166].

is completely analogous to the steps in Sec. 3.2 with the appropriate substitutions of the axion-induced effects in Eqs. 3.41 and 3.42 with those of Eqs. 3.82 and 3.83, and is not repeated here.) The ultimate reach is up to one order of magnitude stronger than the bound $|G_{aee}| \lesssim 3 \times 10^{-13}/m_e$, obtained from considering the influence of axion-induced excess cooling on white-dwarf luminosity functions [166]. While sensitivity to the irreducible coupling of the QCD axion requires a crystal hosting nuclei with large Schiff moments, a competitive reach to G_{aee}—and scalar DM couplings [87]—can be already realized with commercially available crystal resonators such as quartz or gallium arsenide, and is thus an interesting target for a pilot experiment.

3.4 Discussion

In this work, we have described two new axion DM phenomena, and proposed an experimental concept that may discover QCD axion DM through its model-independent coupling over several decades in mass range. The setup relies on the intrinsic parity breaking in piezoelectric crystals. In such a material, an axion background results in a stress that can resonantly excite bulk acoustic modes if the axion frequency matches a fundamental acoustic frequency (or any of its harmonics) of the crystal, a phenomenon that we call the "piezoaxionic effect". Due to the piezoelectric effect, this excited mode produces a voltage difference across the material that can be read out electrically. An axion background will also generically give another, non-resonant, additive contribution to this voltage difference—the "electroaxionic effect". Our proposed setup is capable of detecting axions from tens of kHz to up to hundred(s) of MHz using well-known techniques from resonant-mass detectors developed for gravitational-wave detection, and low-noise electrical readout circuits used in other axion and dark-photon DM experiments. The most exciting signal is produced by the irreducible P- and T-violating coupling of the QCD axion to gluons, which furthermore requires that the piezoelectric crystal contain spin-polarized nuclei (to break T symmetry) with large Schiff moments. A detectable signal can also arise from the derivative coupling of axion-like particles to electrons, which is less challenging experimentally since the occurrence of the piezoaxionic effect for this coupling does not require polarized spins or the presence of special nuclear isotopes.

On the theoretical front, our treatment in Sec. 3.2.2 of the magnitude of the signal carries a large fractional uncertainty. The three bottlenecks are: a systematically improvable computation of nuclear Schiff moments proportional to $\overline{\theta}_a$ (Sec. 3.1.1); an accurate determination of (soft) octupole deformation parameters for (meta)stable nuclear isotopes (Sec. 3.1.1); and a DFT calculation of the ξ and ζ 3-tensors (Sec. 3.1.3), as well as the θ

and η 2-tensors for the ALP-electron coupling (Sec. 3.3). While difficult, these theoretical issues are not insurmountable, and we plan on addressing them in a future publication.

More research and development is also needed on the experimental front, regarding the following four issues in particular. Firstly, once a suitable crystal is identified using nuclear and crystal DFTs, its synthetic growth methods need to be studied and evaluated. Secondly, the elastic and electric loss angles δ_c and δ_β need to be experimentally determined at cryogenic temperatures, as well as optimal cut geometries and clamping methods to minimize external losses and optimize the signal. Thirdly, more investigation of frequency scanning strategies is desirable: this work showed that electric loading can effectively tune the resonance frequency (and retain sensitivity in a fractional bandwidth of order k^2 in Eq. 3.58), but a (coarse) mechanical loading would reduce the total number of crystals needed to cover a fixed frequency range, and put less stringent requirements on the electrical components of the readout circuit (L_1, C_1, and the SQUID). Finally, it is worthwhile to study the feasibility of quantum-optics-based refrigeration of single acoustic modes (as opposed to the entire crystal), which would suppress the primary background (thermal noise) in our proposed setup and thus further enhance its sensitivity to this guaranteed signal of QCD axion DM. In a shorter time frame, and without these four advances, pathfinder experiments would already be sensitive to other dark matter candidates such as pseudoscalars coupled to electrons (Sec. 3.3 and Fig. 3.9) and scalars coupled to electrons and/or photons [87].

This work studies the implementation of the piezoaxionic effect in the direct detection of DM; in forthcoming work, we will outline its potential applications to static searches for P- and T-violating phenomena. This new observable thus opens up exciting new avenues in the search for physics beyond the Standard Model.

Chapter 4

The Piezoaxionic Force

In the previous chapter, we pointed out that inside a crystal with a P-violating (piezoelectric) lattice structure and polarized nuclear spins (which provide the breaking of T invariance), a QCD axion DM background can manifest itself as a periodic stress that coherently excites a macroscopic strain via Eq. 2.13. We coined this phenomenon "the (converse) piezoaxionic effect", and proposed a new class of DM searches for the QCD axion based on bulk acoustic resonators. (Previous works [89, 167] had noticed that the same coupling can also cause nuclear spin resonance under similar conditions.) Just as piezoelectricity consists of a direct effect (stress generating an electric field) and a converse effect (an electric field producing stress), piezoaxionicity can also be employed to directly generate an axion field.

In this chapter, we discuss a new signature of the QCD axion—the piezoaxionic force—wherein a spin-polarized pyroelectric crystal sources a static monopole axion field through the defining coupling of Eq. 2.13. The resulting in-medium scalar coupling can be orders of magnitude larger than the in-vacuum scalar coupling predicted in the SM, without the need for additional CP violation in the fundamental theory. The ferroaxionic effect can be used as a model-independent source for monopole-dipole forces mediated by the QCD axion, thus motivating a new category of short-range force experiments.

This paper is structured as follows. In Sec. 4.1, we explain how this new coupling arises, and estimate its effective size for some candidate nuclei and crystals. In Sec. 4.2, we describe an experimental setup that can be used to detect the ferroaxionic force, based on a modification of the ARIADNE experiment [44]. The forecasted sensitivity of this modified setup is discussed in Sec. 4.3, and several anticipated noise sources and systematics are addressed in Sec. 4.4. We conclude in Sec. 4.5.

4.1 Theory

Axion interactions— At low energies below QCD confinement, Eq. 2.18 reduces to an effective Lagrangian for the QCD axion coupled to nucleons N (we ignore couplings to electrons and photons):

$$\begin{aligned}\mathcal{L} \supset \frac{(\partial a)^2}{2} - \frac{m_a^2 a^2}{2} - \frac{a}{f_a}\left(\rho_{\mathsf{S}} + \rho_{\mathsf{M}}\right) \\ - g_s^N a \bar{N} N + \frac{g_p^N}{2m_N} \partial_\mu a \bar{N} \gamma^\mu \gamma_5 N.\end{aligned} \tag{4.1}$$

Its mass is inversely related to the decay constant f_a through Eq. 1.2. The factors ρ_{S} and ρ_{M} are effective in-medium energy densities from interactions of the nuclear Schiff moments (SM) S and magnetic quadrupole moments (MQM) M in the material; they are the subject of this work and will be estimated below.

First, we quote the expected in-vacuum scalar (g_s^N) and pseudoscalar (g_p^N) couplings to nucleons. The scalar coupling is CP-violating: in the SM augmented by the QCD axion, it is proportional to the CKM phase, yielding the estimate [168]:

$$g_s^N \sim 10^{-30} \, \frac{10^9 \, \mathrm{GeV}}{f_a} \tag{4.2}$$

for both N = proton, neutron (isospin breaking is suppressed). The numerical value is highly uncertain but unlikely to be more than an order of magnitude smaller than in Eq. 4.2 due to several independent contributions of similar magnitude [73]. It can be larger than in Eq. 4.2 with additional sources of CP violation beyond the Standard Model. For example, infrared "tadpole" contributions to the QCD axion potential that shift the induced minimum of the axion potential at $a/f_a = \bar{\theta}_{\mathrm{ind}}$ can boost it to $g_s^N \approx 1.5 \times 10^{-21} \left(\bar{\theta}_{\mathrm{ind}}/10^{-10}\right) \left(10^9 \, \mathrm{GeV}/f_a\right)$ [73], with the numerical value roughly saturating the experimental upper limit on $|d_n|$ and thus $|\bar{\theta}|$ [20]. The pseudoscalar coupling to nucleons is not CP violating, and has a generic size of:

$$g_p^N \equiv \frac{c_N m_N}{f_a} \approx c_N \times 10^{-9} \, \frac{10^9 \, \mathrm{GeV}}{f_a}. \tag{4.3}$$

The interaction of Eq. 2.13 irreducibly yields the coefficients $c_{\mathrm{proton}} \approx 0.47(3)$ and $c_{\mathrm{neutron}} \approx 0.02(3)$ (e.g. in the KSVZ model [52, 53]). These can easily receive corrections from derivative couplings to quarks: e.g. in DFSZ axion models [15, 51], $c_{\mathrm{proton}} \approx -0.617 + 0.435 \sin^2\beta \pm 0.025$ and $c_{\mathrm{neutron}} \approx 0.254 - 0.414 \sin^2\beta \pm 0.025$ [38].

Axion source— A P- and T-odd "monopole" axion configuration is generated via the equation of motion:

$$\left(\Box + m_a^2\right) a\left(t, \mathbf{x}\right) = -\frac{\rho_{\mathsf{S}} + \rho_{\mathsf{M}}}{f_a} - g_s^N n_N \equiv j(t, \mathbf{x}). \tag{4.4}$$

The source of P and T violation on the RHS can be *explicit* through g_s^N and/or *spontaneous* through the in-medium SM or MQM energy densities ρ_{S} and ρ_{M}; we shall see that the latter two can generate larger axion fields than the scalar coupling of Eq. 4.2. In the quasistatic approximation, the axion field solution to Eq. 4.4 is $a(t, \mathbf{x}) = \int \mathrm{d}^3x' \, (4\pi|\mathbf{x} - \mathbf{x}'|)^{-1} e^{-m_a|\mathbf{x}-\mathbf{x}'|} j(t, \mathbf{x}')$. At a point a distance $\mathbf{D}$ away from a uniform slab of thickness h and large transverse area $A \gg h^2, D^2$, the gradient of the slab-induced theta angle is approximately:

$$\boldsymbol{\nabla}\overline{\theta}_a \simeq -\hat{\mathbf{D}} \frac{j}{2m_a f_a} e^{-m_a D} \left(1 - e^{-m_a h}\right), \tag{4.5}$$

where (slow) time dependence may enter implicitly either through $\mathbf{D}$ or j.

Similarly, a "dipole" axion field configuration may sourced from an ensemble of spins $\boldsymbol{\sigma}_N$ with number density n_N via the pseudoscalar coupling:

$$a(t, \mathbf{x}) = (g_p^N / 8\pi m_N) \int \mathrm{d}^3x' \, n_N(\mathbf{x}') e^{-m_a|\mathbf{x}-\mathbf{x}'|} |\mathbf{x} - \mathbf{x}'|^{-3} (1 + m|\mathbf{x} - \mathbf{x}'|)(\mathbf{x} - \mathbf{x}') \cdot \boldsymbol{\sigma}_N, \tag{4.6}$$

which yields the theta angle gradient

$$\boldsymbol{\nabla}\overline{\theta}_a \simeq -\hat{\mathbf{D}} \left(\hat{\mathbf{D}} \cdot \boldsymbol{\sigma}_N\right) \frac{g_p^N n_N}{4m_N f_a} e^{-m_a D} \left(1 - e^{-m_a h}\right). \tag{4.7}$$

from a uniform slab of large transverse area. The parametric ratio of Eqs. 4.5 and 4.7 is $2j/c_N m_a f_a n_N$ after using Eq. 4.3.

The gradient of the induced theta angle is the observable quantity of interest, as detection is most sensitively performed via the Hamiltonian

$$H \supset -\frac{g_p^N}{m_N} \boldsymbol{\sigma}_N \cdot \boldsymbol{\nabla}\overline{\theta}_a, \tag{4.8}$$

through a spin precession process analogous to nuclear magnetic resonance. The combination of Eqs. 4.5 & 4.8 (Eqs. 4.7 & 4.8) yields a monopole-dipole (dipole-dipole) potential. Ref. [44] has charted out the sensitivity of these potentials proportional to $g_s^N g_p^N$ and $(g_p^N)^2$, respectively. In this work, we propose sourcing a QCD axion gradient through its *irreducible* coupling, via the spontaneous P and T violation—parametrized by the energy densities ρ_{S} and ρ_{M} of SMs and MQMs—that a parity-odd crystal with polarized nuclear spins may exhibit.

Schiff Moment— The QCD axion field generated via the SM is proportional to:

$$\rho_{\mathsf{S}} = 4\pi e n_{\mathrm{S}} \frac{\partial \mathsf{S}}{\partial \bar{\theta}_a} \boldsymbol{\mathcal{M}}_{\mathsf{S}} \cdot \hat{\mathbf{I}} \tag{4.9}$$

$$\boldsymbol{\mathcal{M}}_{\mathsf{S}} = \sum_{j,m_j} \epsilon_{s,m_j} \epsilon^*_{p_{j,m_j}} \boldsymbol{\mathcal{M}}_{\mathsf{S}:\, j,m_j} + \text{c.c.}, \tag{4.10}$$

where n_{S} is the density of nuclei with large Schiff moments, $\boldsymbol{\mathcal{M}}_{\mathsf{S}}$ is an atomic matrix element related to mixing between the nuclear SM potential and atomic electrons, with direction given by the intrinsic electric polarization vector of the (necessarily pyroelectric) crystal, and $\mathbf{I}$ is the nuclear spin vector, normalized such that $|\hat{\mathbf{I}}| = 1$ corresponds to a fully polarized nuclear spin state.The quantum numbers j and m_j are those of the total angular momentum and its projection on the z-axis, respectively. The coefficients ϵ_s and $\epsilon_{p_{j,m_j}}$ parametrize the admixture of atomic s and p_{j,m_j} valence electron states, i.e. $|\psi_{\mathrm{el}}\rangle = \sum_{m_j} \epsilon_{s,mj} |s^0\rangle + \sum_{j,m_j} \epsilon_{p_{j,m_j}} |p^0_{j,m_j}\rangle$, and characterize the breaking of parity symmetry by the crystal potential. The atomic matrix element is [1, 169]:

$$\boldsymbol{\mathcal{M}}_{\mathsf{S}:\, j,m_j} = \langle \Omega_s | \hat{\mathbf{r}} | \Omega_{p,j,m_j} \rangle \frac{Z^2}{a_0^4 (\nu_s \nu_{p_j})^{3/2}} \mathcal{R}_j, \tag{4.11}$$

where Ω_i are spherical spinor wavefunctions [170] §35 and $\mathcal{R}_j$ is a relativistic enhancement factor [98], ranging from 1–9 and increasing with the size of the nucleus.

The axion signal from the SM is largest for a heavy, deformed nuclei with a large SM dependence on $\bar{\theta}_a$, a large number density in the crystal n_{S}, and then only within suitable crystals. The ferroaxionic effect is proportional to the dimensionless vector $\epsilon_s \epsilon_p^* \langle \Omega_s | \hat{\mathbf{r}} | \Omega_p \rangle$, whose $\mathcal{O}(1)$ matrix elements are listed in [1, App. A], and can only have nonzero expectation value in the pyroelectric crystal classes [121]. Based on naive dimensional analysis, the wavefunction admixtures $\epsilon_{s,p}$ should also be $\mathcal{O}(1)$ in strong pyroelectrics, but a precise determination requires input from ab initio methods such as density functional theory (DFT) (e.g. [171]).

Magnetic Quadrupole Moment— The effective MQM energy density in Eq. 4.4 is given by [169]:

$$\rho_{\mathsf{M}} = e n_{\mathsf{M}} \frac{\partial \mathsf{M}}{\partial \bar{\theta}_a} t_{fg} A_{fg} \tag{4.12}$$

$$t_{fg} = \frac{1}{4I\,(2I-1)} \left[I_f I_g + I_g I_f - \frac{2}{3} \delta_{fg} I(I+1) \right] \tag{4.13}$$

$$A_{fg} = \frac{Z^2 \alpha}{a_0^3 (\nu_s \nu_{p_J})^{3/2}} \mathcal{C}_J \sum_{m_J} \epsilon_{s,m_J} \epsilon^*_{p_{m_J}} \tag{4.14}$$
$$\langle \Omega_{p_{3/2},m_J} | \sigma_f \hat{r}_g + \sigma_g \hat{r}_f - 2(\boldsymbol{\sigma} \cdot \hat{\boldsymbol{r}}) \hat{r}_g \hat{r}_f | \Omega_{s_{1/2}} \rangle + \text{c.c.}$$

where $\mathcal{C}_J$ is an $\mathcal{O}(1)$ numerical coefficient detailed in App. B.3 and $\boldsymbol{\sigma}$ is the electron spin operator. Only nuclei with spin $I \geq 1$ may exhibit an MQM. The MQM also requires breaking of rotaitonal symmetry, which can be achieved through a nuclear spin polarization, as detailed in appendix B.1.

Since the MQM operator is linear in electron spin it requires magnetic ordering. The first two terms in the second line of eq. 4.14 are linear in the radial vector and are therefore non-zero in a pyroelectric material due to its unique axis of spontaneous polarization. The last term is cubic in the radial vector and is therefore a parity odd, rank three tensor in the electron's position space, which is also symmetric in its indices. These symmetry properties are shared by the piezoelectric tensor of a material, and suggest that the MQM can be non-zero in not only in the pyroelectrics necessary for the SM but also in the broader class of piezoelectric materials (of which pyroelectrics are a subset).

Individual matrix elements without the mixing ϵ_i are give in appendix B.3. Following the same reasoning as the SM, we expect the terms:

$$\epsilon_{s,m_j} \epsilon^*_{p_{m_j}} \langle \Omega_{p_{3/2},m_j} | \sigma_f \hat{r}_g + \sigma_g \hat{r}_f - 2(\boldsymbol{\sigma} \cdot \hat{\boldsymbol{r}}) \hat{r}_f \hat{r}_g | \Omega_{s_{1/2}} \rangle$$

to be no larger than $\mathcal{O}(1)$.

4.2 Setup

The envisioned experimental setup could be somewhat similar to that proposed in Ref. [44] and refined in Ref. [174]. An oblate spheroidal cavity filled with laser-polarized ^{3}He can be used to sense the effective magnetic field sourced by a spin-polarized piezoelectric

	S_{def} ($\overline{\theta}_a\, e\,\mathrm{fm}^3$)	M_{def} ($\overline{\theta}_a\, e\,\mathrm{fm}^2$)
$^{153}_{63}$Eu	0.15 [172]	1.0
$^{235}_{92}$U*	3 [173]	3.1
$^{237}_{93}$Np*	0.75 [172]	1.3

Table 4.1: Estimated Schiff moments and MQMs of deformed (octupole or quadrupole) nuclei. The Schiff moments were calculated in the references given, whereas the MQMs are estimated using the results in chapter 10 of [169] and [112] with pion-nucleon couplings from [103] (see also [1]). * indicates a metastable radioactive nucleus.

source mass doped with heavy nuclei that exhibit a large Schiff moment and/or magnetic quadrupole moment. The spheroidal shape results in a uniform magnetic field inside the sample for samples polarized along one of the principal axes. The source mass generates an axion potential from three distinct mechanisms: (1) its Schiff moment, (2) its nuclear magnetic quadrupole moment, and (3) the dipole-dipole coupling from polarized nuclei resulting from both the gluon and fermion coupling of the axion to matter. The source mass has a flat plate geometry to maximize the amount of material near the NMR sample within the Compton wavelength of the axion. For the search from the Schiff moment or MQM, the nuclear spins of the source mass should be polarized in-plane, whereas to search for the dipole-dipole interaction the source mass should be polarized out of plane, as illustrated in Fig. 4.1.

The spheroidal ^{3}He sample is inside of a quartz sample block that can be coated with a layer of superconducting thin film magnetic shielding as well as additional layers of superconducting foils. The source mass distance to the sample d can be modulated at the nuclear larmor precession frequency to drive coherent precession and Rabi oscillations in the sample. A linear stage can be used to actuate the position of the source mass with respect to the sample block. The precessing transverse magnetization is read out using a SQUID magnetometer.

Ferroaxionic crystals— The ideal material for this setup should contain a high density of heavy nuclei with either large Schiff or magnetic quadrupole moments. In addition, the material should also be magnetic so that the polarized electron spins can be used to transfer their polarization onto the nuclear spins, as detailed in appendix B.2. Potential materials include europium barium titanate $Eu_{0.5}Ba_{0.5}TiO_3$[175], Np_3OF_{12} and $NpIO_5$ [132].

Proposed measurement protocol. The experiment could be performed inside a dilution refrigerator with a large bore and a vector magnet, to facilitate polarizing the source mass either in-plane or out-of-plane. The ^{3}He sample block can be maintained at 4 K, while the source mass and its linear translation stage can be connected to the dilution fridge mixing chamber plate and cooled to 20 mK. After magnetization, the field can ramped down, and at this point the Nb is heated above Tc and re-cooled in zero field to minimize trapped magnetic flux. Laser polarized ^{3}He can be produced at room temperature above the cryostat and pumped into the sample block for the measurements.

4.3 Sensitivity

We assume a source mass plate transverse dimensions of 300 λ and thickness 10 λ for two specific geometries. We expect the sensitivity to be fundamentally limited by quantum spin projection noise in the NMR sample. The minimum transverse magnetic resonant field this setup is sensitive to is given by:

$$B_{\rm min} \approx p^{-1}\sqrt{\frac{2\hbar b}{n_s \mu_{^3{\rm He}} \gamma V T_2}} = 3\times 10^{-19}\ {\rm T}\times \left(\frac{1}{p}\right)\sqrt{\left(\frac{b}{1\ {\rm Hz}}\right)\left(\frac{1\ {\rm mm}^3}{V}\right)\left(\frac{10^{21}\ {\rm cm}^{-3}}{n_s}\right)\left(\frac{1000\ {\rm s}}{T_2}\right)}. \tag{4.15}$$

Here V is the sample volume, γ is the gyromagnetic ratio for ^{3}He $= (2\pi)\times 32.4$ MHz/T, b is the measurement bandwidth, and $\mu_{^3{\rm He}} = -2.12\times\mu_n$ is the ^{3}He nuclear moment, where μ_n is the nuclear Bohr magneton. Figs. 4.2, 4.3 and 4.4 show the expected sensitivity, assuming a ^{3}He sample with T_2=1000 s, and a 1-year integration time. SQUID sensitivity used in figures 4.2 and 4.3 folows the ARIADNE projects in reference [44]: for $\lambda_a < 0.1mm$, the sensitivity is $0.15\frac{fT}{\sqrt{Hz}}\left(\frac{1cm^2}{10^4\lambda_a^2}\right)$, and for $\lambda_a > 0.1mm$, it is $0.15\frac{fT}{\sqrt{Hz}}$.

4.4 Systematics and Noise sources

Several of the systematics and noise sources are in common with those discussed in Refs. [44, 174], except with the additional complication being from the magnetized nature of the source mass. The main systematics and noise sources in the present setup are expected from magnetic gradients and background vibrtaions, magnetic fields that are not

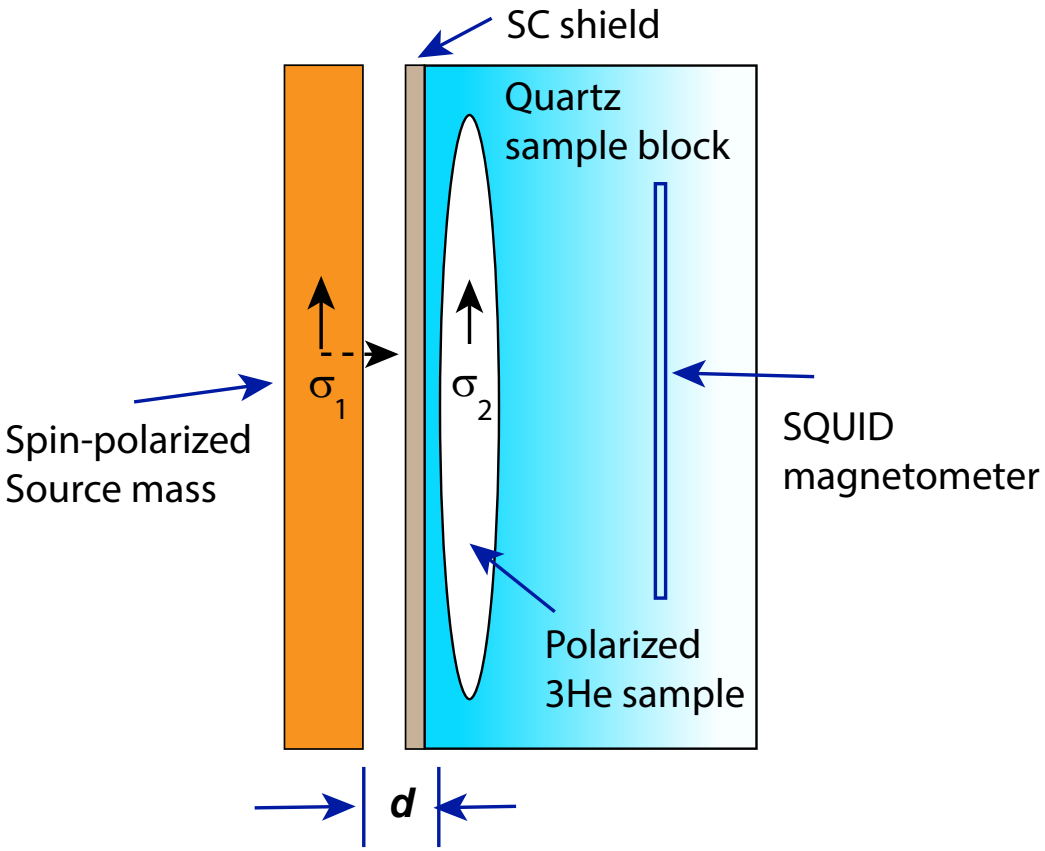

Figure 4.1: Experimental setup. A polarized ^{3}He sample senses the effective magnetic field sourced by a spin-polarized source mass which generates an axion potential from its Schiff moment, its nuclear magnetic quadrupole moment, and the polarized nuclei from both the gluon and fermion coupling of the axion to matter.

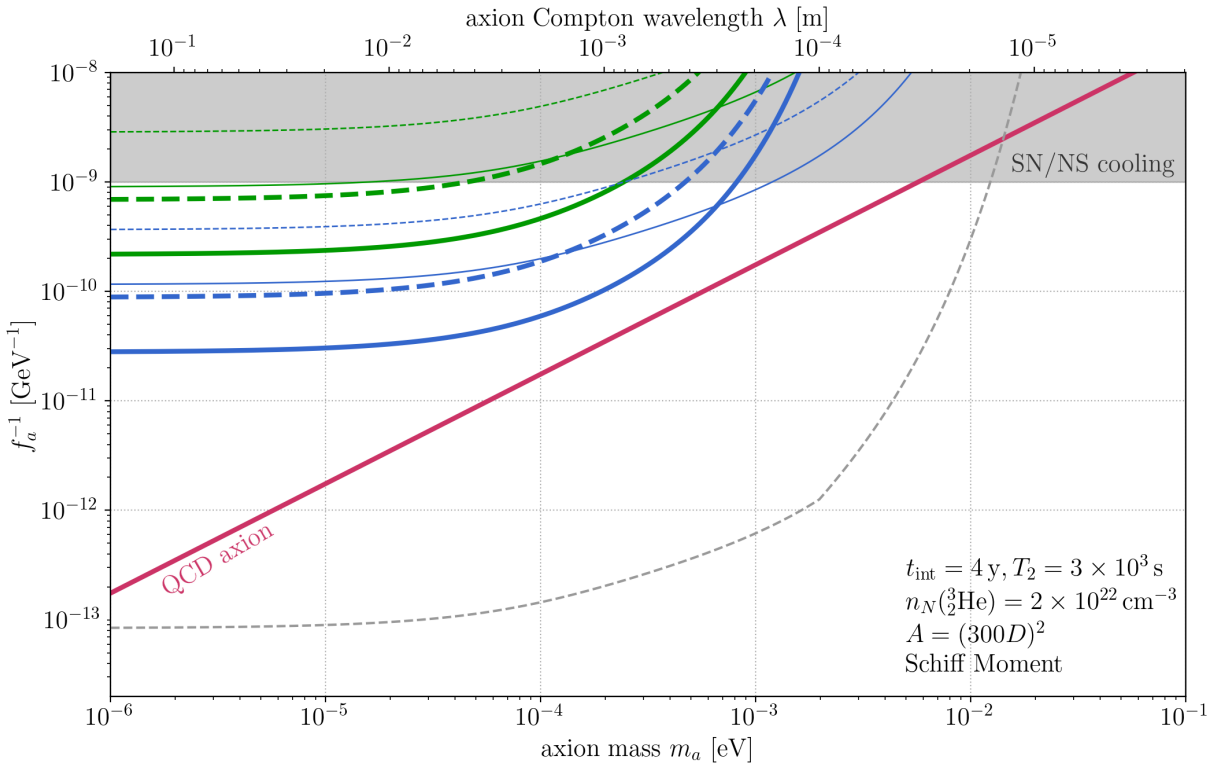

Figure 4.2: Sensitivity to the gluon coupling for a monopole-dipole force generated by the nuclear Schiff moment. The blue (green) curves correspond to the material $NpOF_{12}$ ($Eu_{0.5}Ba_{0.5}TiO_3$). Thick (thin) lines correspond to $D = 1.0$mm (0.15mm). Solid (dashed) lines correspond to c_N for the model-dependent dipole coupling of 1 (0.1). The grey line is the ultimate SQUID sensitivity, whereas the colored lines correspond to a magnetization noise limited setup.

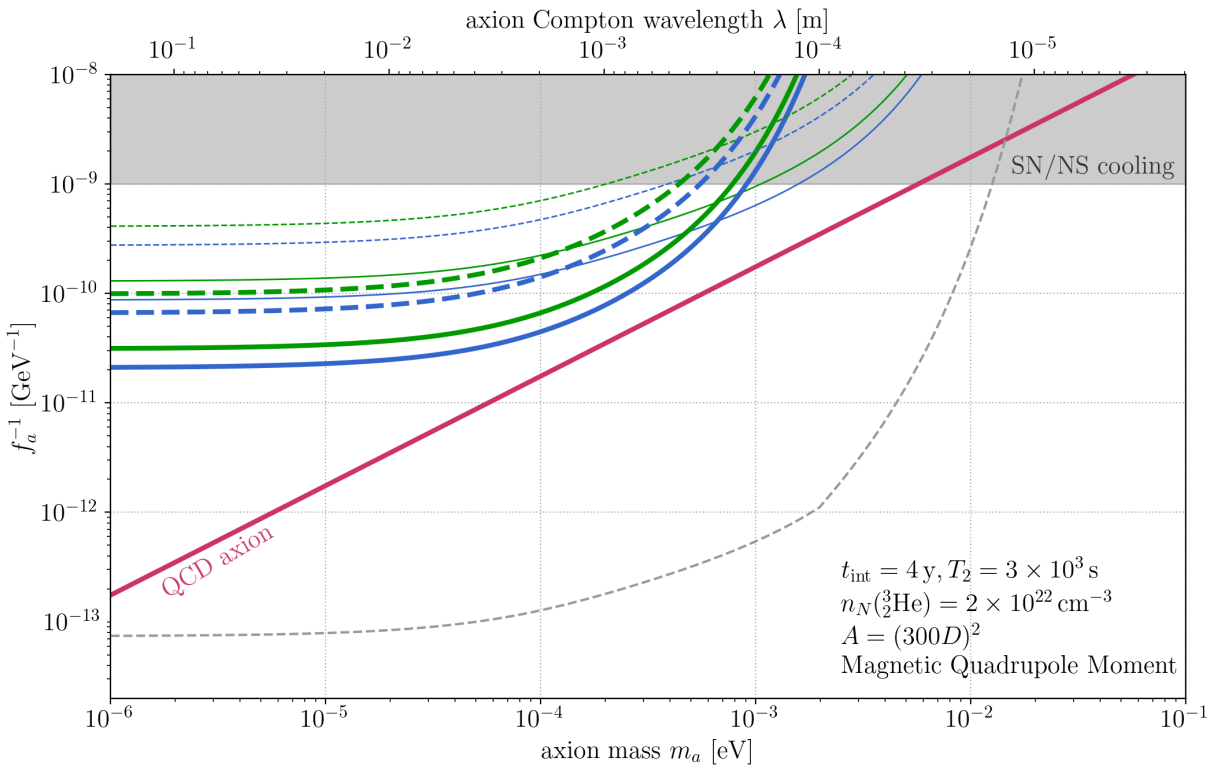

Figure 4.3: Sensitivity to the gluon coupling for a monopole-dipole force generated by the nuclear magnetic quadrupole moment (MQM). Lines correspond to the same setup as fig. 4.2.

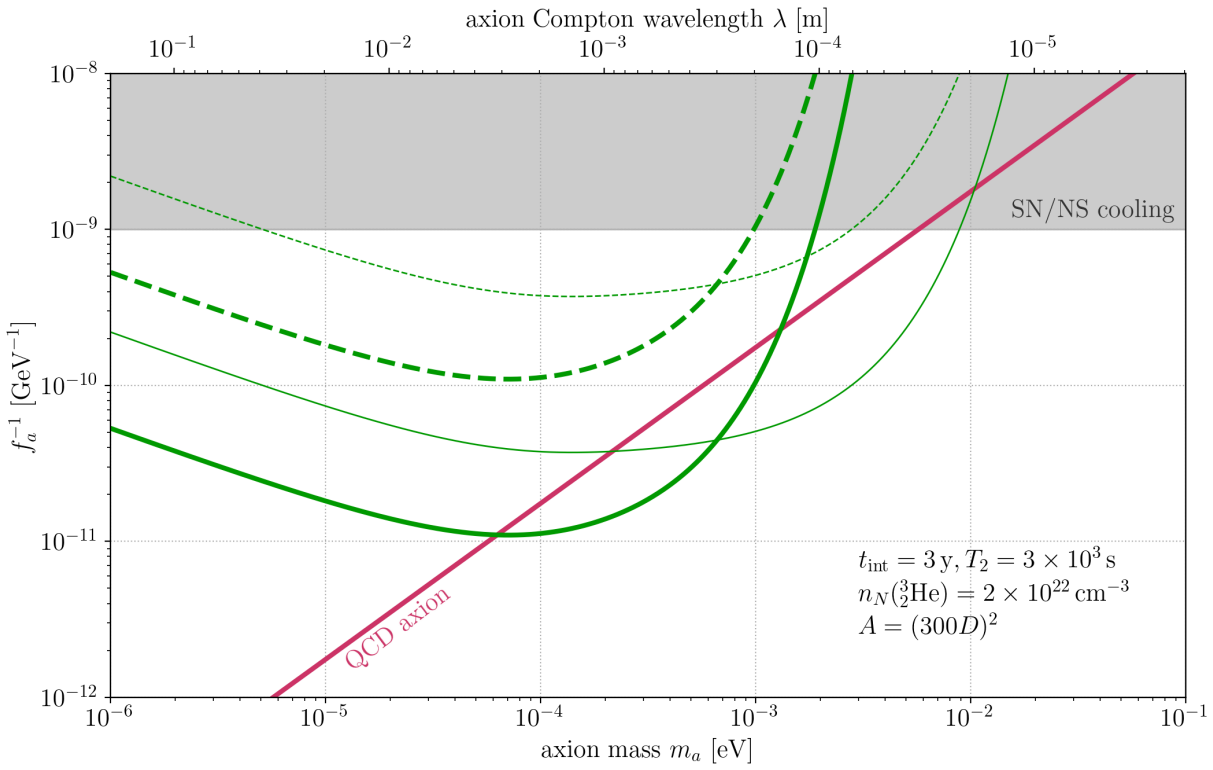

Figure 4.4: Sensitivity to the gluon coupling for a dipole-dipole force, proportional to $1/f_a$, as a function of axion mass m_a. Lines correspond to the same setup as fig. 4.3.

adequately screened by the superconducting shield, and noise due to trapped flux in the superconducting shield. Magnetic gradients within the sample block itself can be reduced using superconducting gradient compensation coils, and the applied magnetic field at the ^{3}He sample can be set using a "D"-shaped half-Helmholtz coil, using the methods described in Ref. [176]. Backgrounds from magnetic impurities, the Barnett effect, are expected to be less significant. Depending on the applied ambient field used to preserve spin polarization during the measurement, effects from the finite magnetic susceptibility of the source mass sample also can be significant.

Fig. 4.5 shows the magnetic field profile extending away from the source mass assuming polarized nuclear spins in the sample with a magnetization of 10^3 A/m. The field at the front surface of the sample chamber is estimated to be of order Guass, so the shielding factor required on the front is approximately 10^{18}. We consider a two-layer superconducting shield, composed of a 1 μm thick Nb film and a 10 μm thick Pb foil. The penetration depth of the foil is approximately 39 nm, which should provide adequate shielding for thickness greater than 2 μm. Although the sample region is enclosed in superconducting shielding, openings are required to facilitate electrical connections to the SQUID readout as well as the current loops for setting the Larmor frequency at the sample and minimizing the gradient of the field, as described in Ref. [176]. To maximally screen the magnetic field of the magnetized source mass from the sample, we consider a single tube opening in the back of the sample chamber. For a tube, the shielding factor depends on the length l and radius a of the tube as $\cosh\left[1.84z/a\right]$ [177].

It is important to also consider the detail for how the wiring for the SQUID magnetometer and gradient compensation coils and "D" shaped Helmholtz coils is connected through the tube opening [176]. For example, as discussed in Ref. [176], if a superconducting wire extends down the length of the shielded tube at the rear of the sample enclosure, due to topological effects of the region not being simply connected, the Meissner screeing effect is severely reduced, and the external magnetic field can penetrate into the sheilded volume. To avoid this, a transition from superconducting to normal metal is needed e.g half way down the length of the tube, as indicated in Ref. [176]. This the effective length of the tube can be conservatively considered as the length of the normal metal portion. From Fig. 4.5, we estimate the magnetic field from the magnetized source mass at the location of the back of the sample block a few cm away to be on the order of 10^{-7} T. We estimate the required aspect ratio of ~ 18 and tube length 90 mm will suffice to achieve the sensitivity shown in Figs. 4.2, 4.3 and 4.4.

Acoustic vibrations. As in the setup used for the ARIADNE experiment [44], acoustic vibrations can cause magnetic field variations due to the image magnetization arising from the Meissner effect in the superconducting shields. For a 0.1 μm wobble in the source

mass stage plate at $\omega_m/2\pi = 10$ Hz, for a suitable size probe we roughly estimate a $\delta_x \sim 2$ nm vibrational amplitude of the sample chamber. The helium gas mixture in our regime has a sound speed of order 300 m/s, so the motion of the gas molecules can follow the displacement of the shield adiabatically for a motion of this amplitude at 10 Hz. We therefore expect no significant magnetic field fluctuations, provided the quartz enclosure containing the sample moves rigidly. We can estimate the degree to which this approximation breaks down by considering the quartz wall thickness, size, and known elastic properties. Assuming $\delta_x = 2$ nm, we find that the relative motion between the sample chamber and the shield coating on the outside surface of the quartz block from elastic deformations is 10^{-17} m. With a gradient of 10^{-5} T/m, this corresponds to a field background of $\sim 10^{-22}$ T. Incoherent background vibration of the source mass stage plate also should remain below 0.1 μm amplitude at 10 Hz, since this would produce magnetic field noise of 5×10^{-19} T/$\sqrt{\text{Hz}}$ at the resonant frequency, which can in principle begin to limit the sensitivity.

4.5 Conclusions

In this work, we have established a new monopole-dipole force mediated by the QCD axion that is generated by a magnetic piezoelectric crystal. This new force could lead to an observable signal in an NMR-like experiment, probing several orders of unexplored parameter space in a range that is complimentary to cavity experiments and astrophysical bounds. The origin of this force is a new effective scalar coupling of the QCD axion that derives from its irreducible, parity and time reversal violating coupling to gluons, together with the large intrinsic parity violation provided by the lattice structure of the piezoelectric crystal, and the time-reversal violation provided by its magnetic ordering. The proposed experimental setup could directly follow the ARIADNE axion experiment, which is currently under construction [78, 174].

Due to Schiff screening, the new scalar coupling presented in this work requires either a nuclear Schiff or magnetic quadrupole moment (Sec. 4.1). While both of these produce a signal of a similar size, the MQM may be favorable since its symmetry properties allow a broader class of materials. Future work will be needed to confirm the ideal material, as well as density functional theory calculations to precisely determine the size of atomic parity violation within the crystal. The large difference between the magnetization noise in the NMR sample and the fundamental SQUID noise limit indicates potential for big improvements in sensitivity, which may be accessed through squeezing procedures.

The setup in this paper will also be sensitive to a dipole-dipole force that could be

produced by either the QCD axion or an axion-like particle (fig. 4.4). Depending on the size of the model dependent dipole coupling coefficient c_N, this force can be either more or less sensitive than the piezoaxionic monopole-dipole force. It should nevertheless be pointed out that the piezoaxionic monopole-dipole force is orders of magnitude bigger than the monopole-dipole force that is sourced by the CP violation of the Standard Model in vacuum. Ultimately, the piezoaxionic force, unlike the dipole-dipole force, would provide conclusive evidence that the mediating particle is indeed the QCD axion of the strong CP problem.

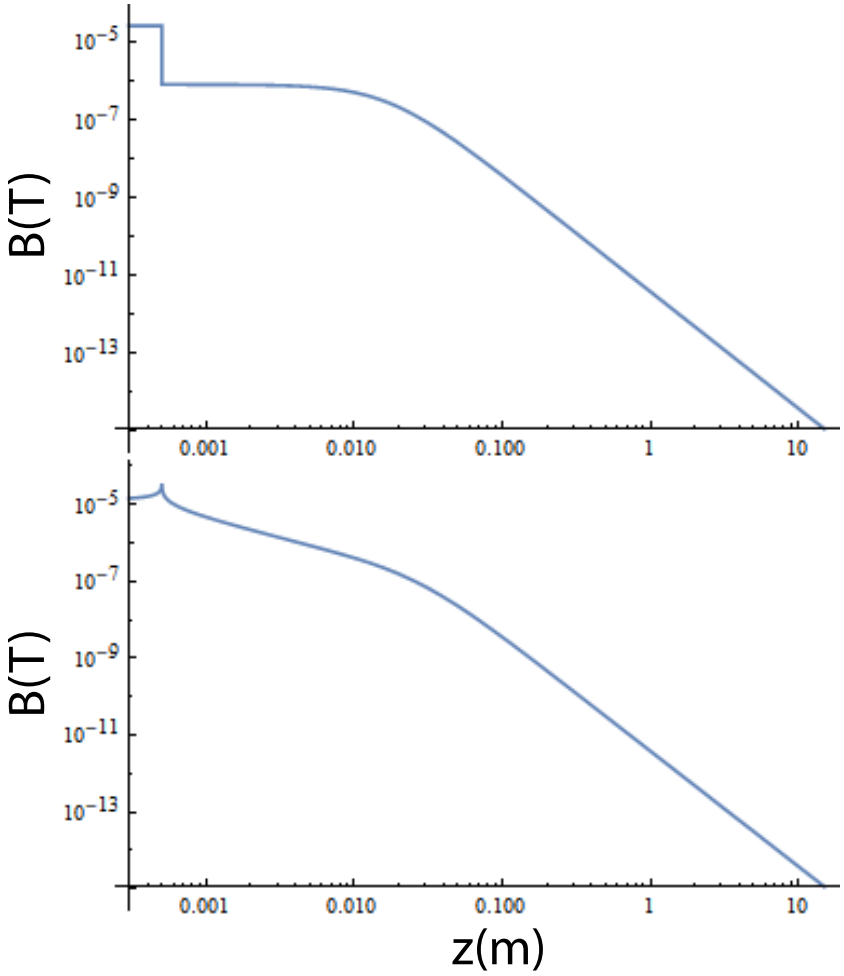

Figure 4.5: (upper) Magnetic field norm along the z-axis of the sample extending away from the source mass center. Parameters chosen as described in text. (lower) as above but from the source mass edge along the y-axis.

Chapter 5

Summary and Outlook

The axion stands out as one of our best motivated targets for new physics beyond the standard model and as a candidate for the dark matter. Its light mass and broad parameter space call for conceptually new experimental approaches. Ongoing efforts are already underway to construct and operate various experiments, each targeting different couplings and mass scales. However, very few of these experiments currently possess the sensitivity required to reach the QCD axion's parameter space. Particularly challenging to probe and therefore underexplored is the axion's defining, model-independent coupling to gluons. This thesis has endeavored to demonstrate how we can use existing experimental technologies and methods to probe the gluon coupling via new precision experimental observables.

A core idea of this thesis is that a piezoelectric crystal provides the key spontaneous breaking of parity symmetry necessary to access parity even observables for the pseudoscalar axion field. The first observable explored in this thesis, the piezoaxionic effect for dark matter, describes how we can leverage piezoelectric crystals to produce an oscillating mechanical strain from a background axion dark matter field. This strain is resonantly enhanced when the natural frequency of the crystal is matched to the mass of the axion. A crucial obstacle to probing the axion's gluon coupling in macroscopic systems is Schiff's theorem, whereby the electric dipole moment of a nucleus is shielded by the surrounding electrons. Schiff's theorem can be violated by incorporating heavy or significantly octupole deformed nuclei, which motivates the specific materials that could be used in this setup to provide the best sensitivity to the axion. The oscillating strain in the material, via the piezoelectric effect, would subsequently generate an alternating current that could be readout via a SQUID. We found the projected sensitivity to the axion to cover the mass range from 10^{-11}eV to 10^{-7}eV. As a benchmark, we also examined this setup's sensitivity

to the model-dependent axion-electron coupling, and found that it had the potential to also reach sensitivities below current bounds from white dwarf cooling.

In the chapter on the piezoaxionic force, we explored how piezoelectric crystals can also act as a source of axions. The core of the idea stems from generating a new effective scalar coupling of the axion to nucleons. Since the coefficient of this scalar operator is P and T odd, it requires a source of P and T breaking external to the SM and the axion field. In previous works in the literature, this symmetry violation was supplied by assuming new fields beyond the standard model in addition to the axion [73]. In this thesis, we proposed generating an effective scalar coupling in-medium using a piezoelectric crystal and polarized spins in the material. This coupling could be used to generate off-shell axions that constitute a new force, with a range determined by the mass of the axion. On the detection side, this force interacts with spins via a pseudoscalar coupling of the axions, and can cause a sample of nuclear spins to precess. By shielding away magnetic fields, we can isolate an anomalous precession generated by the axion. The signal can be resonantly enhanced when we mechanically pulse our source crystal at the natural frequency of the nuclear spins in our detector — the Larmor precession frequency. This setup could be applicable to an axion within the mass range 10^{-5}eV to 10^{-2}eV, and would build on existing experiments looking for forces mediated by axion-like particles [44].

This thesis provides new theoretical frameworks and suggests corresponding experimental setups with projected axion sensitivities. But what are the next steps to discovery? A number of key areas require further investigation: precise determination of nuclear Schiff moments and material couplings, and experimental exploration of suitable materials. The first of these, accurate determination of nuclear Schiff moments, the author is already investigating in collaboration with specialists in nuclear theory and will appear in a future work. Searching for ideal materials could entail a mixture of experimental and computational investigation. While some material properties such as piezoelectric coefficients can be predicted using ab initio computational techniques like Density Functional Theory (DFT), other properties will need dedicated experimental investigation, such the mechanical quality factors of materials at cryogenic temperatures. DFT could also be essential in precisely determining the mixing of opposite parity electron wave functions in the vicinity of nuclei, designated $\epsilon_{s,p}$ in this thesis, which is required to understand the couplings of the axion induced Schiff moment to the material strain or scalar nucleon coupling.

One of the biggest challenges in building an axion detector is scanning the axion's mass across multiple orders of magnitude. The currently allowed parameter space for the axion is vast, and covering it all with sufficient sensitivity within a reasonable time frame is a formidable task. Indeed, most proposed axion experiments would have remarkable sensitivity on resonance if we knew precisely which axion mass to target from the outset.

Finding optimal scanning strategies is therefore an important task, especially for the dark matter experiment proposed in this thesis. If one could find a way to mechanically scan by changing the resonant frequency of the crystal continuously, it could make a huge impact on the total parameter space we could probe with such an experiment. An idea for the future could be to consider different geometries, such as different shaped cuts of crystals or systems where the boundary conditions, i.e., the electrodes, could be continuously varied to probe a greater number of resonances within the same setup.

What lies ahead? The concepts explored here should inspire us to pursue further regions of the axion's parameter space, and our various experimental directions and approaches beyond this thesis should be seen as complementary to one another. The search for the axion challenges us to showcase our ingenuity and creativity. Rather than reaching for ever higher energies, it asks us to meticulously test the fundamental laws of nature with utmost precision. One can only imagine how marvelous it will be if we discover new physical principles beyond the standard model, or perhaps even dark matter, in the next few decades within a single laboratory.

References

[1] Asimina Arvanitaki, Amalia Madden, and Ken Van Tilburg. Piezoaxionic effect. *Phys. Rev. D*, 109(7):072009, 2024.

[2] Georges Aad et al. Observation of a new particle in the search for the Standard Model Higgs boson with the ATLAS detector at the LHC. *Phys. Lett. B*, 716:1–29, 2012.

[3] Serguei Chatrchyan et al. Observation of a New Boson at a Mass of 125 GeV with the CMS Experiment at the LHC. *Phys. Lett. B*, 716:30–61, 2012.

[4] X. Fan, T. G. Myers, B. A. D. Sukra, and G. Gabrielse. Measurement of the Electron Magnetic Moment. *Phys. Rev. Lett.*, 130(7):071801, 2023.

[5] Csaba Csáki, Salvator Lombardo, and Ofri Telem. *TASI Lectures on Non-supersymmetric BSM Models*, pages 501–570. WSP, 2018.

[6] Stephen P. Martin. A Supersymmetry primer. *Adv. Ser. Direct. High Energy Phys.*, 18:1–98, 1998.

[7] Dietrich Bödeker and Wilfried Buchmüller. Baryogenesis from the weak scale to the grand unification scale. *Rev. Mod. Phys.*, 93:035004, Aug 2021.

[8] André de Gouvêa. Neutrino Mass Models. *Ann. Rev. Nucl. Part. Sci.*, 66:197–217, 2016.

[9] Yuval Grossman and Philip Tanedo. Just a Taste: Lectures on Flavor Physics. In *Theoretical Advanced Study Institute in Elementary Particle Physics: Anticipating the Next Discoveries in Particle Physics*, pages 109–295, 2018.

[10] Steven Weinberg. The cosmological constant problem. *Rev. Mod. Phys.*, 61:1–23, Jan 1989.

[11] Michael J. Mortonson, David H. Weinberg, and Martin White. Dark Energy: A Short Review. 12 2013.

[12] Frank Wilczek. Problem of Strong P and T Invariance in the Presence of Instantons. *Phys. Rev. Lett.*, 40:279–282, 1978.

[13] Steven Weinberg. A New Light Boson? *Phys. Rev. Lett.*, 40:223–226, 1978.

[14] R. D. Peccei and Helen R. Quinn. CP Conservation in the Presence of Instantons. *Phys. Rev. Lett.*, 38:1440–1443, 1977.

[15] Michael Dine, Willy Fischler, and Mark Srednicki. A Simple Solution to the Strong CP Problem with a Harmless Axion. *Phys. Lett. B*, 104:199–202, 1981.

[16] Mariangela Lisanti. Lectures on Dark Matter Physics. In *Theoretical Advanced Study Institute in Elementary Particle Physics: New Frontiers in Fields and Strings*, pages 399–446, 2017.

[17] Gerard 't Hooft. Symmetry Breaking Through Bell-Jackiw Anomalies. *Phys. Rev. Lett.*, 37:8–11, 1976.

[18] Curtis G. Callan, Jr., R. F. Dashen, and David J. Gross. The Structure of the Gauge Theory Vacuum. *Phys. Lett. B*, 63:334–340, 1976.

[19] R. Jackiw and C. Rebbi. Vacuum Periodicity in a Yang-Mills Quantum Theory. *Phys. Rev. Lett.*, 37:172–175, 1976.

[20] C. Abel et al. Measurement of the Permanent Electric Dipole Moment of the Neutron. *Phys. Rev. Lett.*, 124(8):081803, 2020.

[21] J. H. Christenson, J. W. Cronin, V. L. Fitch, and R. Turlay. Evidence for the 2π Decay of the K_2^0 Meson. *Phys. Rev. Lett.*, 13:138–140, 1964.

[22] V. Agrawal, Stephen M. Barr, John F. Donoghue, and D. Seckel. Viable range of the mass scale of the standard model. *Phys. Rev. D*, 57:5480–5492, 1998.

[23] F. Zwicky. Die Rotverschiebung von extragalaktischen Nebeln. *Helv. Phys. Acta*, 6:110–127, 1933.

[24] Annamaria Borriello and Paolo Salucci. The Dark matter distribution in disk galaxies. *Mon. Not. Roy. Astron. Soc.*, 323:285, 2001.

[25] Henk Hoekstra, Howard Yee, and Mike Gladders. Current status of weak gravitational lensing. *New Astron. Rev.*, 46:767–781, 2002.

[26] R. Benton Metcalf, Leonidas A. Moustakas, Andrew J. Bunker, and Ian R. Parry. Spectroscopic gravitational lensing and limits on the dark matter substructure in Q2237+0305. *Astrophys. J.*, 607:43–59, 2004.

[27] N. Aghanim et al. Planck 2018 results. VI. Cosmological parameters. *Astron. Astrophys.*, 641:A6, 2020. [Erratum: Astron.Astrophys. 652, C4 (2021)].

[28] S. Tremaine and J. E. Gunn. Dynamical Role of Light Neutral Leptons in Cosmology. *Phys. Rev. Lett.*, 42:407–410, 1979.

[29] Simon D. M. White, C. S. Frenk, and M. Davis. Clustering in a Neutrino Dominated Universe. *Astrophys. J. Lett.*, 274:L1–L5, 1983.

[30] M. Milgrom. A Modification of the Newtonian dynamics as a possible alternative to the hidden mass hypothesis. *Astrophys. J.*, 270:365–370, 1983.

[31] Jacob D. Bekenstein. Relativistic gravitation theory for the MOND paradigm. *Phys. Rev. D*, 70:083509, 2004. [Erratum: Phys.Rev.D 71, 069901 (2005)].

[32] Douglas Clowe, Marusa Bradac, Anthony H. Gonzalez, Maxim Markevitch, Scott W. Randall, Christine Jones, and Dennis Zaritsky. A direct empirical proof of the existence of dark matter. *Astrophys. J. Lett.*, 648:L109–L113, 2006.

[33] Cumrun Vafa and Edward Witten. Parity Conservation in QCD. *Phys. Rev. Lett.*, 53:535, 1984.

[34] Asimina Arvanitaki, Savas Dimopoulos, Sergei Dubovsky, Nemanja Kaloper, and John March-Russell. String Axiverse. *Phys. Rev. D*, 81:123530, 2010.

[35] John Preskill, Mark B. Wise, and Frank Wilczek. Cosmology of the Invisible Axion. *Phys. Lett. B*, 120:127–132, 1983.

[36] Laurence F Abbott and P Sikivie. A cosmological bound on the invisible axion. *Physics Letters B*, 120(1-3):133–136, 1983.

[37] Michael Dine and Willy Fischler. The Not So Harmless Axion. *Phys. Lett. B*, 120:137–141, 1983.

[38] Giovanni Grilli Di Cortona, Edward Hardy, Javier Pardo Vega, and Giovanni Villadoro. The qcd axion, precisely. *Journal of High Energy Physics*, 2016(1):1–37, 2016.

[39] Georg G. Raffelt. Astrophysical axion bounds. *Lect. Notes Phys.*, 741:51–71, 2008.

[40] C. Bartram et al. Search for Invisible Axion Dark Matter in the 3.3–4.2 μeV Mass Range. *Phys. Rev. Lett.*, 127(26):261803, 2021.

[41] Masha Baryakhtar, Marios Galanis, Robert Lasenby, and Olivier Simon. Black hole superradiance of self-interacting scalar fields. *Phys. Rev. D*, 103(9):095019, 2021.

[42] Neal Dalal and Andrey Kravtsov. Excluding fuzzy dark matter with sizes and stellar kinematics of ultrafaint dwarf galaxies. *Phys. Rev. D*, 106(6):063517, 2022.

[43] Antonio Branca, Michele Bonaldi, Massimo Cerdonio, Livia Conti, Paolo Falferi, Francesco Marin, Renato Mezzena, Antonello Ortolan, Giovanni A Prodi, Luca Taffarello, et al. Search for an ultralight scalar dark matter candidate with the auriga detector. *Physical review letters*, 118(2):021302, 2017.

[44] Asimina Arvanitaki and Andrew A. Geraci. Resonantly Detecting Axion-Mediated Forces with Nuclear Magnetic Resonance. *Phys. Rev. Lett.*, 113(16):161801, 2014.

[45] Valery A. Rubakov and Dmitry S. Gorbunov. *Introduction to the Theory of the Early Universe: Hot big bang theory*. World Scientific, Singapore, 2017.

[46] Anson Hook. TASI Lectures on the Strong CP Problem and Axions. *PoS*, TASI2018:004, 2019.

[47] Igor García Irastorza. An introduction to axions and their detection. *SciPost Phys. Lect. Notes*, page 45, 2022.

[48] Benjamin R. Safdi. TASI Lectures on the Particle Physics and Astrophysics of Dark Matter. *PoS*, TASI2022:009, 2024.

[49] Andreas Pargner. *Phenomenology of Axion Dark Matter*. PhD thesis, KIT, Karlsruhe, IKP, 2 2019.

[50] R. J. Crewther, P. Di Vecchia, G. Veneziano, and Edward Witten. Chiral Estimate of the Electric Dipole Moment of the Neutron in Quantum Chromodynamics. *Phys. Lett. B*, 88:123, 1979. [Erratum: Phys.Lett.B 91, 487 (1980)].

[51] A. R. Zhitnitsky. On Possible Suppression of the Axion Hadron Interactions. (In Russian). *Sov. J. Nucl. Phys.*, 31:260, 1980.

[52] Jihn E. Kim. Weak Interaction Singlet and Strong CP Invariance. *Phys. Rev. Lett.*, 43:103, 1979.

[53] Mikhail A. Shifman, A. I. Vainshtein, and Valentin I. Zakharov. Can Confinement Ensure Natural CP Invariance of Strong Interactions? *Nucl. Phys. B*, 166:493–506, 1980.

[54] Luca Di Luzio, Maurizio Giannotti, Enrico Nardi, and Luca Visinelli. The landscape of QCD axion models. *Phys. Rept.*, 870:1–117, 2020.

[55] P.A. Zyla et al. Review of Particle Physics. *PTEP*, 2020(8):083C01, 2020.

[56] David JE Marsh. Axion cosmology. *Physics Reports*, 643:1–79, 2016.

[57] Eleonora Di Valentino, Elena Giusarma, Massimiliano Lattanzi, Olga Mena, Alessandro Melchiorri, and Joseph Silk. Cosmological Axion and neutrino mass constraints from Planck 2015 temperature and polarization data. *Phys. Lett. B*, 752:182–185, 2016.

[58] Asimina Arvanitaki, Savas Dimopoulos, Marios Galanis, Luis Lehner, Jedidiah O. Thompson, and Ken Van Tilburg. Large-misalignment mechanism for the formation of compact axion structures: Signatures from the QCD axion to fuzzy dark matter. *Phys. Rev. D*, 101(8):083014, 2020.

[59] Junwu Huang, Amalia Madden, Davide Racco, and Mario Reig. Maximal axion misalignment from a minimal model. *JHEP*, 10:143, 2020.

[60] David J. Gross, Robert D. Pisarski, and Laurence G. Yaffe. QCD and Instantons at Finite Temperature. *Rev. Mod. Phys.*, 53:43, 1981.

[61] George Lazarides, Robert K. Schaefer, D. Seckel, and Q. Shafi. Dilution of Cosmological Axions by Entropy Production. *Nucl. Phys. B*, 346:193–212, 1990.

[62] Max Tegmark, Anthony Aguirre, Martin Rees, and Frank Wilczek. Dimensionless constants, cosmology and other dark matters. *Phys. Rev. D*, 73:023505, 2006.

[63] R. L. Workman and Others. Review of Particle Physics. *PTEP*, 2022:083C01, 2022.

[64] T. W. B. Kibble. Some Implications of a Cosmological Phase Transition. *Phys. Rept.*, 67:183, 1980.

[65] Marco Gorghetto, Edward Hardy, and Giovanni Villadoro. More axions from strings. *SciPost Phys.*, 10(2):050, 2021.

[66] Ciaran O'Hare. cajohare/axionlimits: Axionlimits. https://cajohare.github.io/AxionLimits/, July 2020.

[67] Maxim Pospelov and Adam Ritz. Electric dipole moments as probes of new physics. *Annals Phys.*, 318:119–169, 2005.

[68] Derek F. Jackson Kimball et al. Overview of the Cosmic Axion Spin Precession Experiment (CASPEr). *Springer Proc. Phys.*, 245:105–121, 2020.

[69] Alex I. Braginski and John Clarke. *Applications of SQUIDS and SQUID systems.* WILEY-VCH, 2006.

[70] Anson Hook and Junwu Huang. Probing axions with neutron star inspirals and other stellar processes. *Journal of High Energy Physics*, 2018(6):1–22, 2018.

[71] P. Sikivie. Experimental tests of the "invisible" axion. *Phys. Rev. Lett.*, 51:1415–1417, Oct 1983.

[72] S. Asztalos, E. Daw, H. Peng, L. J Rosenberg, C. Hagmann, D. Kinion, W. Stoeffl, K. van Bibber, P. Sikivie, N. S. Sullivan, D. B. Tanner, F. Nezrick, M. S. Turner, D. M. Moltz, J. Powell, M.-O. André, J. Clarke, M. Mück, and Richard F. Bradley. Large-scale microwave cavity search for dark-matter axions. *Phys. Rev. D*, 64:092003, Oct 2001.

[73] Shohei Okawa, Maxim Pospelov, and Adam Ritz. Long-range axion forces and hadronic CP violation. *Phys. Rev. D*, 105(7):075003, 2022.

[74] M. Pospelov. CP odd interaction of axion with matter. *Phys. Rev. D*, 58:097703, 1998.

[75] A. A. Geraci et al. Progress on the ARIADNE axion experiment. *Springer Proc. Phys.*, 211:151–161, 2018.

[76] JE Moody and Frank Wilczek. New macroscopic forces? *Physical Review D*, 30(1):130, 1984.

[77] Georg Raffelt. Limits on a *cp*-violating scalar axion-nucleon interaction. *Phys. Rev. D*, 86:015001, Jul 2012.

[78] Chloe Lohmeyer et al. Source Mass Characterization in the ARIADNE Axion Experiment. *Springer Proc. Phys.*, 245:71–81, 2020.

[79] Lippmann, G. Principe de la conservation de l'électricité, ou second principe de la théorie des phénomènes électriques. *J. Phys. Theor. Appl.*, 10(1):381–394, 1881.

[80] J. Curie and P. Curie. Contractions et dilatations produites par des tensions dans les cristaux hémièdres à faces inclinées. *C R Acad Sci Gen*, 93:1137–1140, 01 1881.

[81] J. Curie and P. Curie. Développement, par pression, de l'électricité polaire dans les cristaux hémièdres à faces inclinées. *C R Acad Sci Gen*, 91:294–295, 01 1880.

[82] J. Curie and P. Curie. Sur l'électricité polaire dans les cristaux hémièdres à faces inclinées. *C R Acad Sci Gen*, 91:383–386, 01 1880.

[83] J. Weber. Detection and Generation of Gravitational Waves. *Phys. Rev.*, 117:306–313, 1960.

[84] J. Weber. Gravitational Radiation. *Phys. Rev. Lett.*, 18(13):498–501, 1967.

[85] Odylio Denys Aguiar. The Past, Present and Future of the Resonant-Mass Gravitational Wave Detectors. *Res. Astron. Astrophys.*, 11:1–42, 2011.

[86] P. Astone et al. Results of the IGEC-2 search for gravitational wave bursts during 2005. *Phys. Rev. D*, 76:102001, 2007.

[87] Asimina Arvanitaki, Savas Dimopoulos, and Ken Van Tilburg. Sound of dark matter: searching for light scalars with resonant-mass detectors. *Physical review letters*, 116(3):031102, 2016.

[88] Antonio Branca et al. Search for an Ultralight Scalar Dark Matter Candidate with the AURIGA Detector. *Phys. Rev. Lett.*, 118(2):021302, 2017.

[89] Peter W. Graham and Surjeet Rajendran. New Observables for Direct Detection of Axion Dark Matter. *Phys. Rev. D*, 88:035023, 2013.

[90] SK Lamoreaux. Solid-state systems for the electron electric dipole moment and other fundamental measurements. *Physical Review A*, 66(2):022109, 2002.

[91] TN Mukhamedjanov and OP Sushkov. Suggested search for pb 207 nuclear schiff moment in pb ti o 3 ferroelectric. *Physical Review A*, 72(3):034501, 2005.

[92] D Budker, SK Lamoreaux, AO Sushkov, and OP Sushkov. Sensitivity of condensed-matter p-and t-violation experiments. *Physical Review A*, 73(2):022107, 2006.

[93] Alexander O Sushkov, S Eckel, and SK Lamoreaux. Prospects for an electron electric-dipole-moment search with ferroelectric (eu, ba) tio 3 ceramics. *Physical Review A*, 81(2):022104, 2010.

[94] KZ Rushchanskii, S Kamba, V Goian, P Vaněk, M Savinov, J Prokleška, D Nuzhnyy, K Knížek, F Laufek, S Eckel, et al. A multiferroic material to search for the permanent electric dipole moment of the electron. *Nature materials*, 9(8):649–654, 2010.

[95] Dmitry Budker, Peter W Graham, Micah Ledbetter, Surjeet Rajendran, and Alexander O Sushkov. Proposal for a cosmic axion spin precession experiment (casper). *Physical Review X*, 4(2):021030, 2014.

[96] L. I. Schiff. Measurability of Nuclear Electric Dipole Moments. *Physical Review*, 132(5):2194–2200, December 1963.

[97] T. E. Chupp, P. Fierlinger, M. J. Ramsey-Musolf, and J. T. Singh. Electric dipole moments of atoms, molecules, nuclei, and particles. *Rev. Mod. Phys.*, 91:015001, Jan 2019.

[98] I.B. Khriplovich and S.K. Lamoreaux. *CP violation without strangeness: Electric dipole moments of particles, atoms, and molecules*. Springer Science & Business Media, 1997.

[99] Jonathan Engel, Michael J. Ramsey-Musolf, and U. van Kolck. Electric dipole moments of nucleons, nuclei, and atoms: The standard model and beyond. *Progress in Particle and Nuclear Physics*, 71:21–74, 2013. Fundamental Symmetries in the Era of the LHC.

[100] O P Sushkov, V V Flambaum, and I B Khriplovich. Possibility of investigating p- and t-odd nuclear forces in atomic and molecular experiments. *Sov. Phys. - JETP (Engl. Transl.); (United States)*, 60:5, 11 1984.

[101] W. C. Haxton and E. M. Henley. Enhanced t-nonconserving nuclear moments. *Phys. Rev. Lett.*, 51:1937–1940, Nov 1983.

[102] A. Griffiths and P. Vogel. One-body parity and time reversal violating potentials. *Phys. Rev. C*, 43:2844–2848, Jun 1991.

[103] J. de Vries, E. Epelbaum, L. Girlanda, A. Gnech, E. Mereghetti, and M. Viviani. Parity- and time-reversal-violating nuclear forces. 1 2020.

[104] Peter Herczeg. Time reversal violation in nuclear processes. *Symmetries and Fundamental Interactions in Nuclei*, page 89–125, 1995.

[105] I. S. Towner and A. C. Hayes. P, T violating nuclear matrix elements in the one meson exchange approximation. *Phys. Rev. C*, 49:2391–2397, 1994.

[106] V. V. Flambaum, I. B. Khriplovich, and O. P. Sushkov. On the P and T Nonconserving Nuclear Moments. *Nucl. Phys. A*, 449:750–760, 1986.

[107] P. A. Butler. Octupole collectivity in nuclei. *J. Phys. G*, 43(7):073002, 2016.

[108] Kenneth S Krane. *Introductory nuclear physics*. Wiley, New York, NY, 1988.

[109] PA Butler. Pear-shaped atomic nuclei. *Proceedings of the Royal Society A*, 476(2239):20200202, 2020.

[110] Yuchen Cao, Sylvester E Agbemava, Anatoli V Afanasjev, Witold Nazarewicz, Erik Olsen, et al. Landscape of pear-shaped even-even nuclei. *Physical Review C*, 102(2):024311, 2020.

[111] V. Spevak, N. Auerbach, and V. V. Flambaum. Enhanced T odd P odd electromagnetic moments in reflection asymmetric nuclei. *Phys. Rev. C*, 56:1357–1369, 1997.

[112] J. Engel, James Lewis Friar, and A. C. Hayes. Nuclear octupole correlations and the enhancement of atomic time reversal violation. *Phys. Rev. C*, 61:035502, 2000.

[113] P. Möller, A.J. Sierk, T. Ichikawa, and H. Sagawa. Nuclear ground-state masses and deformations: Frdm(2012). *Atomic Data and Nuclear Data Tables*, 109-110:1–204, 2016.

[114] Shuichiro Ebata and Takashi Nakatsukasa. Octupole deformation in the nuclear chart based on the 3D Skyrme Hartree Fock plus BCS model. *Phys. Scripta*, 92(6):064005, 2017.

[115] W Nazarewicz, P Olanders, I Ragnarsson, J Dudek, GA Leander, P Möller, and E Ruchowsa. Analysis of octupole instability in medium-mass and heavy nuclei. *Nuclear Physics A*, 429(2):269–295, 1984.

[116] National nuclear data center, https://www.nndc.bnl.gov/nudat2/, current.

[117] V. V. Flambaum and H. Feldmeier. Enhanced nuclear schiff moment in stable and metastable nuclei. *Phys. Rev. C*, 101:015502, Jan 2020.

[118] T KIBÉDI and R.H SPEAR. Reduced electric-octupole transition probabilities, an update. *Atomic Data and Nuclear Data Tables*, 80(1):35–82, 2002.

[119] E.M. Lifshitz and L.P. Pitaevskij. *Relativistic quantum theory*. Number v. 2 in Landau, Lev D.: Course of theoretical physics. Pergamon, 1974.

[120] H.F. Tiersten. *Linear Piezoelectric Plate Vibrations: Elements of the Linear Theory of Piezoelectricity and the Vibrations Piezoelectric Plates*. Springer US, 1969.

[121] John Frederick Nye et al. *Physical properties of crystals: their representation by tensors and matrices*. Oxford university press, 1985.

[122] J. Yang. *An Introduction to the Theory of Piezoelectricity*. Kluwer Academic Publishers, 2005.

[123] Don A Berlincourt, Daniel R Curran, Hans Jaffe, et al. Piezoelectric and piezomagnetic materials and their function in transducers. *Physical Acoustics: Principles and Methods*, 1(Part A):202–204, 1964.

[124] W. C. Griffith, M. D. Swallows, T. H. Loftus, M. V. Romalis, B. R. Heckel, and E. N. Fortson. Improved limit on the permanent electric dipole moment of ^{199}Hg. *Phys. Rev. Lett.*, 102:101601, Mar 2009.

[125] Charles P Slichter. *Principles of magnetic resonance*. Springer, 2011.

[126] Serge Galliou, Maxim Goryachev, Philippe Abbé, Xavier Vacheret, Michael E. Tobar, and Roger Bourquin. Quality factor measurements of various types of quartz crystal resonators operating near 4k. *IEEE Transactions on Ultrasonics, Ferroelectrics, and Frequency Control*, 63(7):975–980, 2016.

[127] J. Tichỳ, J. Erhart, E. Kittinger, and J. Prívratská. *Fundamentals of Piezoelectric Sensorics: Mechanical, Dielectric, and Thermodynamical Properties of Piezoelectric Materials*. SpringerLink: Springer e-Books. Springer Berlin Heidelberg, 2010.

[128] Jir. Zelenka. *Piezoelectric resonators and their applications*. Studies in electrical and electronic engineering, 24. Elsevier, Amsterdam, 1986.

[129] Maxim Goryachev, Daniel L. Creedon, Eugene N. Ivanov, Serge Galliou, Roger Bourquin, and Michael E. Tobar. Extremely low-loss acoustic phonons in a quartz bulk acoustic wave resonator at millikelvin temperature. *Applied Physics Letters*, 100(24):243504, 2012.

[130] F. Acernese et al. Gravitational wave burst search in the Virgo C7 data. *Class. Quant. Grav.*, 26:085009, 2009.

[131] Maxim Goryachev, Daniel L. Creedon, Eugene N. Ivanov, Serge Galliou, Roger Bourquin, and Michael E. Tobar. Extremely Low-Loss Acoustic Phonons in a Quartz Bulk Acoustic Wave Resonator at Millikelvin Temperature. *Appl. Phys. Lett.*, 100:243504, 2012.

[132] Anubhav Jain, Shyue Ping Ong, Geoffroy Hautier, Wei Chen, William Davidson Richards, Stephen Dacek, Shreyas Cholia, Dan Gunter, David Skinner, Gerbrand Ceder, and Kristin a. Persson. The Materials Project: A materials genome approach to accelerating materials innovation. *APL Materials*, 1(1):011002, 2013.

[133] Salzenstein, Patrice. Recent progress in the performances of ultrastable quartz resonators and oscillators. *Int. J. Simul. Multisci. Des. Optim.*, 7:A8, 2016.

[134] Maxim Goryachev. *Bulk acoustic wave resonators and oscillators at liquid helium temperatures*. Theses, Université de Franche-Comté, November 2011.

[135] IEEE Standard. Ieee standard on piezoelectricity. *ANSI/IEEE Std 176-1987*, 1988.

[136] Saptarshi Chaudhuri, Peter W Graham, Kent Irwin, Jeremy Mardon, Surjeet Rajendran, and Yue Zhao. Radio for hidden-photon dark matter detection. *Physical Review D*, 92(7):075012, 2015.

[137] Yonatan Kahn, Benjamin R Safdi, and Jesse Thaler. Broadband and resonant approaches to axion dark matter detection. *Physical review letters*, 117(14):141801, 2016.

[138] Jonathan L Ouellet, Chiara P Salemi, Joshua W Foster, Reyco Henning, Zachary Bogorad, Janet M Conrad, Joseph A Formaggio, Yonatan Kahn, Joe Minervini, Alexey Radovinsky, et al. Design and implementation of the abracadabra-10 cm axion dark matter search. *Physical Review D*, 99(5):052012, 2019.

[139] M. Goryachev. Bulk acoustic wave resonators and oscillators at liquid helium temperatures. 2011.

[140] Claude Hilbert and John Clarke. Measurements of the dynamic input impedance of a dc squid. *Journal of low temperature physics*, 61(3):237–262, 1985.

[141] Saptarshi Chaudhuri, Kent Irwin, Peter W Graham, and Jeremy Mardon. Optimal impedance matching and quantum limits of electromagnetic axion and hidden-photon dark matter searches. *arXiv preprint arXiv:1803.01627*, 2018.

[142] Paolo Falferi, Michele Bonaldi, M Cerdonio, R Mezzena, GA Prodi, A Vinante, and S Vitale. 10h superconducting quantum interference device amplifier for acoustic gravitational wave detectors. *Applied Physics Letters*, 93(17):172506, 2008.

[143] Stephen E. Kuenstner et al. Quantum metrology of low frequency electromagnetic modes with frequency upconverters. 10 2022.

[144] Claudia D Tesche and John Clarke. Dc squid: Noise and optimization. *Journal of Low Temperature Physics*, 29(3):301–331, 1977.

[145] Morgan W. Mitchell and Silvana Palacios Alvarez. Colloquium: Quantum limits to the energy resolution of magnetic field sensors. *Rev. Mod. Phys.*, 92:021001, Apr 2020.

[146] R Khatiwada, L Dennis, R Kendrick, M Khosravi, M Peters, E Smith, and W M Snow. Materials with low dc magnetic susceptibility for sensitive magnetic measurements. *Measurement Science and Technology*, 27(2):025902, Dec 2015.

[147] F D Smith. The magnetostriction constant for alternating magnetic fields. *Proceedings of the Physical Society*, 42(3):181–191, apr 1930.

[148] Peter R Saulson. *Fundamentals of interferometric gravitational wave detectors*. World Scientific, 1994.

[149] Michele Bignotto, Marta Bonaldi, Massimo Cerdonio, Livia Conti, Francesco Penasa, Giovanni Prodi, Gabriele Soranzo, L. Taffarello, and Jean-Pierre Zendri. New suspension system for the gravitational wave bar detector auriga. *Review of Scientific Instruments - REV SCI INSTR*, 76, 08 2005.

[150] Man-Sung Yim. Influence of fuel design and reactor operation on spent fuel management. *International Conference on The Management of Spent Fuel from Nuclear Power Reactors*, 2015.

[151] K. Uhlig and W. Hehn. 3he4he dilution refrigerator precooled by gifford-mcmahon refrigerator. *Cryogenics*, 37(5):279–282, 1997.

[152] Aaron D O'Connell, Max Hofheinz, Markus Ansmann, Radoslaw C Bialczak, Mike Lenander, Erik Lucero, Matthew Neeley, Daniel Sank, H Wang, Ms Weides, et al. Quantum ground state and single-phonon control of a mechanical resonator. *Nature*, 464(7289):697–703, 2010.

[153] Kfir Blum, Raffaele Tito D'Agnolo, Mariangela Lisanti, and Benjamin R Safdi. Constraining axion dark matter with big bang nucleosynthesis. *Physics Letters B*, 737:30–33, 2014.

[154] Reuven Balkin, Javi Serra, Konstantin Springmann, Stefan Stelzl, and Andreas Weiler. White dwarfs as a probe of light QCD axions. 11 2022.

[155] Jun Zhang, Zhenwei Lyu, Junwu Huang, Matthew C Johnson, Laura Sagunski, Mairi Sakellariadou, and Huan Yang. First constraints on light axions from the binary neutron star gravitational wave event gw170817. *arXiv preprint arXiv:2105.13963*, 2021.

[156] Asimina Arvanitaki and Sergei Dubovsky. Exploring the String Axiverse with Precision Black Hole Physics. *Phys. Rev. D*, 83:044026, 2011.

[157] Christopher Abel, Nicholas J Ayres, Giles Ban, Georg Bison, Kazimierz Bodek, V Bondar, Manfred Daum, Malcolm Fairbairn, Victor V Flambaum, Peter Geltenbort, et al. Search for axionlike dark matter through nuclear spin precession in electric and magnetic fields. *Physical Review X*, 7(4):041034, 2017.

[158] Seung Pyo Chang, Selçuk Hacıömeroğlu, On Kim, Soohyung Lee, Seongtae Park, and Yannis K Semertzidis. Axionlike dark matter search using the storage ring edm method. *Physical Review D*, 99(8):083002, 2019.

[159] Deniz Aybas, Janos Adam, Emmy Blumenthal, Alexander V Gramolin, Dorian Johnson, Annalies Kleyheeg, Samer Afach, John W Blanchard, Gary P Centers, Antoine Garcon, et al. Search for axionlike dark matter using solid-state nuclear magnetic resonance. *Physical Review Letters*, 126(14):141802, 2021.

[160] Chiara P Salemi, Joshua W Foster, Jonathan L Ouellet, Andrew Gavin, Kaliroe MW Pappas, Sabrina Cheng, Kate A Richardson, Reyco Henning, Yonatan Kahn, Rachel Nguyen, et al. The search for low-mass axion dark matter with abracadabra-10cm. *arXiv preprint arXiv:2102.06722*, 2021.

[161] Alexander V Gramolin, Deniz Aybas, Dorian Johnson, Janos Adam, and Alexander O Sushkov. Search for axion-like dark matter with ferromagnets. *Nature Physics*, 17(1):79–84, 2021.

[162] Zhongyue Zhang, Oindrila Ghosh, and Dieter Horns. Wisplc: Search for dark matter with lc circuit, 2021.

[163] Jonathan L Ouellet, Chiara P Salemi, Joshua W Foster, Reyco Henning, Zachary Bogorad, Janet M Conrad, Joseph A Formaggio, Yonatan Kahn, Joe Minervini, Alexey Radovinsky, et al. First results from abracadabra-10 cm: A search for sub-μ ev axion dark matter. *Physical review letters*, 122(12):121802, 2019.

[164] S Chaudhuri et al. Dmradio-gut: Probing gut-scale qcd axion dark matter. Snowmass, 2021.

[165] R. Barbieri, C. Braggio, G. Carugno, C.S. Gallo, A. Lombardi, A. Ortolan, R. Pengo, G. Ruoso, and C.C. Speake. Searching for galactic axions through magnetized media: The quax proposal. *Physics of the Dark Universe*, 15:135–141, 2017.

[166] MM Miller Bertolami, Brenda E Melendez, Leandro G Althaus, and Jordi Isern. Revisiting the axion bounds from the galactic white dwarf luminosity function. *Journal of Cosmology and Astroparticle Physics*, 2014(10):069, 2014.

[167] Dmitry Budker, Peter W. Graham, Micah Ledbetter, Surjeet Rajendran, and Alex Sushkov. Proposal for a Cosmic Axion Spin Precession Experiment (CASPEr). *Phys. Rev. X*, 4(2):021030, 2014.

[168] Howard Georgi and Lisa Randall. Flavor Conserving CP Violation in Invisible Axion Models. *Nucl. Phys. B*, 276:241–252, 1986.

[169] I. B. Khriplovich and S. K. Lamoreaux. *CP violation without strangeness: Electric dipole moments of particles, atoms, and molecules*. 1997.

[170] V. B. Berestetskii, E. M. Lifshitz, and L. P. Pitaevskii. *QUANTUM ELECTRODYNAMICS*, volume 4 of *Course of Theoretical Physics*. Pergamon Press, Oxford, 1982.

[171] L. V. Skripnikov and A. V. Titov. LCAO-based theoretical study of PbTiO3 crystal to search for parity and time reversal violating interaction in solids. *The Journal of Chemical Physics*, 145(5):054115, 08 2016.

[172] Oleg P. Sushkov. Schiff moments of deformed nuclei. 7 2023.

[173] V. V. Flambaum and H. Feldmeier. Enhanced nuclear Schiff moment in stable and metastable nuclei. *Phys. Rev. C*, 101(1):015502, 2020.

[174] AA Geraci, H Fosbinder-Elkins, C Lohmeyer, J Dargert, M Cunningham, M Harkness, E Levenson-Falk, S Mumford, A Kapitulnik, A Arvanitaki, et al. Progress on the ariadne axion experiment. *arXiv preprint arXiv:1710.05413*, 2017.

[175] D. L. Janes, R. E. Bodnar, and A. L. Taylor. Europium barium titanate—A magnetic ferroelectric compound. *Journal of Applied Physics*, 49(3):1452–1454, 08 2008.

[176] H Fosbinder-Elkins, Y Kim, J Dargert, M Harkness, A A Geraci, E Levenson-Falk, S Mumford, A Fang, A Kapitulnik, A Matlashov, D Kim, Y Shin, Y K Semertzidis, Y-H Lee, N Aggarwal, C Lohmeyer, A Reid, J Shortino, I Lee, J C Long, C-Y Liu, and W Snow. A method for controlling the magnetic field near a superconducting boundary in the ariadne axion experiment. *Quantum Science and Technology*, 7(1):014002, jan 2022.

[177] J. R. Claycomb and J. H. Miller. Superconducting magnetic shields for squid applications. *Review of Scientific Instruments*, 70(12):4562–4568, 1999.

[178] Peter Svrcek and Edward Witten. Axions in string theory. *Journal of High Energy Physics*, 2006(06):051–051, jun 2006.

[179] D. L. Janes, R. E. Bodnar, and A. L. Taylor. Europium barium titanate—A magnetic ferroelectric compound. *Journal of Applied Physics*, 49(3):1452–1454, 08 2008.

[180] J. A. Stone and W. L. Pillinger. Nuclear moment ratios in ^{237}Np from mössbaur spectra. *Phys. Rev.*, 165:1319–1326, Jan 1968.

[181] S. G. Zemlyanoi, D. V. Karaivanov, Yu. P. Gangrsky, K. P. Marinova, B. N. Markov, and J. Badamsambuu. Hyperfine splitting constants in the optical transition $\boldsymbol{{{4{f}^{7}} {6{s}^{2}} \;{^{8}{\rm s}_{7/2}} \to {4{f}^{7}} {6{s}6{p}}\; {^{6}{\rm p}_{5/2}} \ {\rm of} \ {^{151-155}{\rm eu}}}$isotopes and hyperfine anomaly. *Hyperfine Interactions*, 196(1):107–113, 2010.

[182] V. V. Flambaum, I. B. Khriplovich, and O. P. Sushkov. On the Possibility to Study P Odd and T Odd Nuclear Forces in Atomic and Molecular Experiments. *Sov. Phys. JETP*, 60:873, 1984.

[183] O P Sushkov, V V Flambaum, and I B Khriplovich. Possibility of investigating p- and t-odd nuclear forces in atomic and molecular experiments. *Sov. Phys. - JETP (Engl. Transl.);*, 1984.

[184] V. V. Flambaum and A. J. Mansour. Enhanced magnetic quadrupole moments in nuclei with octupole deformation and their CP-violating effects in molecules. *Phys. Rev. C*, 105(6):065503, 2022.

[185] L. M. Kovba and A. N. Golubenko Golubenko. Lithium uranate (V) LiUO3", doi ="https://doi.org/10.1007/BF00748866. *Journal of Structural Chemistry*, 1(3):367–370, 1960.

[186] L.D. Landau, J.S. Bell, M.J. Kearsley, L.P. Pitaevskii, E.M. Lifshitz, and J.B. Sykes. *Electrodynamics of Continuous Media*. COURSE OF THEORETICAL PHYSICS. Elsevier Science, 2013.

[187] Gabriel Murphy, Brendan J. Kennedy, Bernt Johannessen, Justin A. Kimpton, Maxim Avdeev, Christopher S. Griffith, Gordon J. Thorogood, and Zhaoming Zhang. Structural studies of the rhombohedral and orthorhombic monouranates. *Journal of Solid State Chemistry*, 237:86–92, 2016.

[188] Cory M. Read, Daniel E. Bugaris, and Hans-Conrad zur Loye. Single crystal growth and structural characterization of four complex uranium oxides. *Solid State Sciences*, 17:40–45, 2013.

[189] D. Drung, C. Abmann, J. Beyer, A. Kirste, M. Peters, F. Ruede, and Th. Schurig. Highly sensitive and easy-to-use squid sensors. *IEEE Transactions on Applied Superconductivity*, 17(2):699–704, 2007.

[190] Jan-Hendrik Storm, Oliver Kieler, and Rainer Körber. Towards Ultrasensitive SQUIDs Based on Submicrometer-Sized Josephson Junctions. *IEEE Trans. Appl. Supercond.*, 30(7):1600705, 2020. [Erratum: IEEE Trans.Appl.Supercond. 30, 9700602 (2020)].

[191] N.W. Ashcroft and N.D. Mermin. *Solid State Physics*. Cengage Learning, 2011.

[192] Ctgs and cngs blanks and wafers. http://www.axtal.com/English/Products/PiezoelectricCrystals/CTGSandCNGSBlanksWafers/. Accessed: 2020-06-5.

[193] A. Ballato. Modeling piezoelectric and piezomagnetic devices and structures via equivalent networks. *IEEE Transactions on Ultrasonics, Ferroelectrics, and Frequency Control*, 48(5):1189–1240, 2001.

[194] A. Ballato. *Basic Material Quartz and Related Innovations*, pages 9–35. Springer Berlin Heidelberg, Berlin, Heidelberg, 2008.

[195] Yuchen Cao, S. E. Agbemava, A. V. Afanasjev, W. Nazarewicz, and E. Olsen. Landscape of pear-shaped even-even nuclei. *Phys. Rev. C*, 102:024311, Aug 2020.

[196] L.D. Landau and E.M. Lifshitz. Chapter ii - electrostatics of dielectrics. In *Electrodynamics of Continuous Media (Second Edition)*, volume 8 of *Course of Theoretical Physics*, pages 34–85. Pergamon, Amsterdam, second edition edition, 1984.

[197] J. Yang. *Analysis of Piezoelectric Devices*. World Scientific, 2006.

[198] R. Machleidt and D. R. Entem. Chiral effective field theory and nuclear forces. *Phys. Rept.*, 503:1–75, 2011.

[199] A. Sotnikov, E. Smirnova, H. Schmidt, M. Weihnacht, J. Götze, and S. Sakharov. Langasite family crystals as promising materials for microacoustic devices at cryogenic temperatures. In *2015 Joint Conference of the IEEE International Frequency Control Symposium the European Frequency and Time Forum*, pages 106–110, 2015.

[200] Fapeng Yu, Xiulan Duan, Shujun Zhang, Qingming Lu, and Xian Zhao. Rare-earth calcium oxyborate piezoelectric crystals reca4o(bo3)3: Growth and piezoelectric characterizations. *Crystals*, 4(3):241–261, 2014.

[201] W. Zhang, Z. P. Li, S. Q. Zhang, and J. Meng. Octupole degree of freedom for the critical-point candidate nucleus ^{152}Sm in a reflection-asymmetric relativistic mean-field approach. *Phys. Rev. C*, 81:034302, Mar 2010.

[202] C. B. Adams et al. Axion Dark Matter. In *Snowmass 2021*, 3 2022.

[203] Peter W. Graham, Igor G. Irastorza, Steven K. Lamoreaux, Axel Lindner, and Karl A. van Bibber. Experimental Searches for the Axion and Axion-Like Particles. *Ann. Rev. Nucl. Part. Sci.*, 65:485–514, 2015.

[204] Anson Hook and Junwu Huang. Probing axions with neutron star inspirals and other stellar processes. *JHEP*, 06:036, 2018.

[205] R. D. Peccei. The Strong CP problem and axions. *Lect. Notes Phys.*, 741:3–17, 2008.

[206] Asimina Arvanitaki, Savas Dimopoulos, and Ken Van Tilburg. Resonant absorption of bosonic dark matter in molecules. *Phys. Rev. X*, 8(4):041001, 2018.

[207] Ia B Zel'dovich. Electromagnetic interaction with parity violation. *Soviet Phys. JETP*, 6, 6 1958.

[208] Y. V. Stadnik and V. V. Flambaum. Axion-induced effects in atoms, molecules, and nuclei: Parity nonconservation, anapole moments, electric dipole moments, and spin-gravity and spin-axion momentum couplings. *Phys. Rev. D*, 89(4):043522, 2014.

[209] V. V. Flambaum and I. B. Khriplovich. P Odd Nuclear Forces as a Source of Parity Nonconservation in Atoms. *Sov. Phys. JETP*, 52:835, 1980.

[210] V.V. Flambaum, I.B. Khriplovich, and O.P. Sushkov. Nuclear anapole moments. *Physics Letters B*, 146(6):367–369, 1984.

[211] Stefano Baroni, Stefano de Gironcoli, Andrea Dal Corso, and Paolo Giannozzi. Phonons and related crystal properties from density-functional perturbation theory. *Rev. Mod. Phys.*, 73:515–562, Jul 2001.

[212] Stefano de Gironcoli, Stefano Baroni, and Raffaele Resta. Piezoelectric properties of iii-v semiconductors from first-principles linear-response theory. *Phys. Rev. Lett.*, 62:2853–2856, Jun 1989.

APPENDICES

Appendix A

Appendices for the Piezoaxionic Effect

A.1 Atomic Matrix Elements

In this appendix, we elaborate on the calculation of the atomic matrix elements used in Sec. 3.1.2. Symmetry dictates that to produce an expectation value for a P-even observable such as an energy shift or mechanical stress, ones requires an even number of P-violating perturbations. In other words, we know that a perturbation to an atomic orbital induced by a P-violating potential from a nuclear Schiff moment, e.g. H_{S}, is not sufficient on its own to produce a P-even effect at linear order by symmetry. The second P-violating perturbation is sourced by the potential of the piezoelectric crystal lattice, V_{crys}. We assume V_{crys} constitutes only a small correction to the atomic potential, such as in the tight-binding model for insulating materials [191].

For specificity, let us suppose that the ground-state wavefunction is $|s^0\rangle$, a mixed s-wave state with $j = 1/2$ and equal admixtures of $m_j = \pm 1/2$, perturbed by the crystal potential as:

$$|\widetilde{s}\rangle = \mathcal{C}\left(|s^0\rangle + \sum_{j,m_j} |p^0_{j,m_j}\rangle \frac{\langle p^0_{j,m_j}| V_{\text{crys}} |s^0\rangle}{E^0_s - E^0_{p_{j,m_j}}}\right) \tag{A.1}$$

$$\equiv \epsilon_s |s^0\rangle + \sum_{j,m_j} \epsilon_{p_{j,m_j}} |p^0_{j,m_j}\rangle\,, \tag{A.2}$$

with $\mathcal{C} = 1 - \sum_{j,m_j} \left| \langle p^0_{j,m_j}| V_{\text{crys}} |s^0\rangle \right|^2/(E^0_s - E^0_{p_{j,m_j}})^2$. The superscript ^{0} denotes an unperturbed atomic wavefunction, and $\{j, m_j\}$ indicate the relativistic orbitals of the atomic p-level, i.e. $(j = 1/2, m_j = 1/2, -1/2)$ and $(j = 3/2, m_j = 3/2, 1/2, -1/2, -3/2)$. In practice, one can perform the above and following calculations for the $m_j = +1/2$ admixture of the $|s^0\rangle$ ground state, and then average the final result with the same for the $m_j = -1/2$ admixture.

The ϵ coefficients can be read off from matching Eqs. A.1 and A.2. They can in principle be computed *ab initio* within the framework of DFT, but care must be taken to compute atomic orbital projection coefficients in the presence of many valence electrons, and to ensure that the variation (with external strain or electric field/displacement) of these coefficients respects the point group symmetries of the crystal. This technically difficult calculation is left to future work, and instead we will use order-of-magnitude estimates based on experimentally measured quantities in Sec. 3.1.3.

We can now consider the leading-order energy shift when the atomic wavefunctions are perturbed by both the Schiff and crystal potentials as:

$$\langle \widetilde{s}|H_{\mathsf{S}}|\widetilde{s}\rangle = \sum_{j,m_j} \epsilon_s \epsilon^*_{p_{j,m_j}} \langle s^0| H_{\mathsf{S}} |p^0_{j,m_j}\rangle + \text{c.c.}, \tag{A.3}$$

which directly leads to Eqs. 3.32 and 4.11 in the main text. The angular parts of the matrix elements between the spinor spherical harmonics Ω_{l,j,m_j} in Eq. 4.11 are:

$$\langle \Omega_{s,\frac{1}{2},+\frac{1}{2}}| \hat{\mathbf{r}} |\Omega_{p,\frac{1}{2},+\frac{1}{2}}\rangle = -\frac{1}{3}\hat{\mathbf{z}}, \tag{A.4}$$

$$\langle \Omega_{s,\frac{1}{2},+\frac{1}{2}}| \hat{\mathbf{r}} |\Omega_{p,\frac{1}{2},-\frac{1}{2}}\rangle = -\frac{1}{3}\hat{\mathbf{x}} + \frac{i}{3}\hat{\mathbf{y}}, \tag{A.5}$$

$$\langle \Omega_{s,\frac{1}{2},+\frac{1}{2}}| \hat{\mathbf{r}} |\Omega_{p,\frac{3}{2},+\frac{3}{2}}\rangle = -\frac{1}{\sqrt{6}}\hat{\mathbf{x}} - \frac{i}{\sqrt{6}}\hat{\mathbf{y}}, \tag{A.6}$$

$$\langle \Omega_{s,\frac{1}{2},+\frac{1}{2}}| \hat{\mathbf{r}} |\Omega_{p,\frac{3}{2},+\frac{1}{2}}\rangle = +\frac{\sqrt{2}}{3}\hat{\mathbf{z}}, \tag{A.7}$$

$$\langle \Omega_{s,\frac{1}{2},+\frac{1}{2}}| \hat{\mathbf{r}} |\Omega_{p,\frac{3}{2},-\frac{1}{2}}\rangle = +\frac{1}{3\sqrt{2}}\hat{\mathbf{x}} - \frac{i}{3\sqrt{2}}\hat{\mathbf{y}}; \tag{A.8}$$

and similarly for the $l = 0, m_j = -1/2$ admixture:

$$\langle \Omega_{s,\frac{1}{2},-\frac{1}{2}} | \, \hat{\mathbf{r}} \, | \Omega_{p,\frac{1}{2},+\frac{1}{2}} \rangle = -\frac{1}{3}\hat{\mathbf{x}} - \frac{i}{3}\hat{\mathbf{y}}, \tag{A.9}$$

$$\langle \Omega_{s,\frac{1}{2},-\frac{1}{2}} | \, \hat{\mathbf{r}} \, | \Omega_{p,\frac{1}{2},-\frac{1}{2}} \rangle = +\frac{1}{3}\hat{\mathbf{z}}, \tag{A.10}$$

$$\langle \Omega_{s,\frac{1}{2},-\frac{1}{2}} | \, \hat{\mathbf{r}} \, | \Omega_{p,\frac{3}{2},+\frac{1}{2}} \rangle = -\frac{1}{3\sqrt{2}}\hat{\mathbf{x}} - \frac{i}{3\sqrt{2}}\hat{\mathbf{y}}. \tag{A.11}$$

$$\langle \Omega_{s,\frac{1}{2},-\frac{1}{2}} | \, \hat{\mathbf{r}} \, | \Omega_{p,\frac{3}{2},-\frac{1}{2}} \rangle = +\frac{\sqrt{2}}{3}\hat{\mathbf{z}}, \tag{A.12}$$

$$\langle \Omega_{s,\frac{1}{2},-\frac{1}{2}} | \, \hat{\mathbf{r}} \, | \Omega_{p,\frac{3}{2},-\frac{3}{2}} \rangle = +\frac{1}{\sqrt{6}}\hat{\mathbf{x}} - \frac{i}{\sqrt{6}}\hat{\mathbf{y}}, \tag{A.13}$$

Transitions with $|\Delta j| \geq 2$ or $|\Delta m_j| \geq 2$ are forbidden by selection rules.

A.2 Long-wavelength Reduction

In this appendix, we derive Eq. 3.38 as the long-wavelength description of the crystal, reduced from the full energy functional that includes short-wavelength degrees of freedom, which are "integrated out". We also derive how the piezoaxionic tensor ξ and the axioelectric tensor ζ relate to wavefunction coefficients that can be computed within DFT and to the atomic matrix elements of Sec. 3.1.2. Our treatment of the short-wavelength modes is based on Refs. [120, 211, 212].

Denote the position of atom $I = (l, s)$ by

$$R^I_\alpha \equiv R^l_\alpha + \tau^s_\alpha + u^{ls}_\alpha, \tag{A.14}$$

where $\mathbf{R}^l$ is the position of the lth unit cell in the Bravais lattice, $\boldsymbol{\tau}^s$ is the relative position of the sth atom within the unit cell, and $\mathbf{u}^{ls}$ is the out-of-equilibrium deviation. In what follows, vector indices will be $\{\alpha, \beta, \gamma, \dots\}$ subscripts running over the 3 spatial directions, unit cell labels $\{l, m\}$ superscripts running over N unit cells with volume V_c, and atomic labels within the unit cell $\{s, t\}$ superscripts.

We can express the total internal energy density around equilibrium to quadratic order in deviations, namely a homogeneous strain $S_{\alpha\beta}$ and electric displacement vector D^α as

well as the individual atomic displacements u_α^{ls}, as:

$$\begin{aligned} U = & \\ & + \frac{1}{2} c^0_{\alpha\beta,\gamma\delta} S_{\alpha\beta} S_{\gamma\delta} - h^0_{\alpha,\gamma\delta} D_\alpha S_{\gamma\delta} + \frac{1}{2} \beta^\infty_{\alpha\beta} D_\alpha D_\beta \\ & + \frac{1}{2NV_c} \sum_{lm,st} C^{ls,mt}_{\alpha\beta} u^{ls}_\alpha u^{mt}_\beta \\ & - \frac{e}{NV_c} \sum_{l,s} Z^s_{\alpha\beta} u^{ls}_\alpha D_\beta + \frac{1}{NV_c} \sum_{l,s} G^s_{\alpha,\gamma\delta} u^{ls}_\alpha S_{\gamma\delta} \\ & - \zeta^0_{\alpha\beta} \hat{I}_\alpha \overline{\theta}_a D_\beta - \sum_s \xi^{0,s}_{\alpha,\gamma\delta} \hat{I}^s_\alpha \overline{\theta}_a S_{\gamma\delta} \\ & - \frac{e}{NV_c} \sum_{l,s} W^s_{\alpha\beta} u^{ls}_\alpha \hat{I}^s_\beta \overline{\theta}_a . \end{aligned} \tag{A.15}$$

In the first two lines of the above equation, we have defined the bare elastic tensor $c^0_{\alpha\beta,\gamma\delta}$, the bare piezoelectric tensor $h^0_{\alpha,\gamma\delta}$, the bare dielectric impermittivity tensor $\beta^\infty_{\alpha\beta}$, the interatomic force matrix $C^{ls,mt}_{\alpha\beta}$, the effective charge matrix $Z^{\alpha\beta}_s$, the internal strain tensor $G^s_{\alpha,\gamma\delta}$, and homogeneous electric displacement vector D_β (inhomogeneous vector field contributions are absorbed into C). Finally, ξ^0 and ζ^0 are the bare piezoaxionic and electroaxionic tensors of Eqs. 3.43 and 3.44, respectively, while the effective "axionic charge tensor" $W^s_{\alpha\beta}$ is given by:

$$W^s_{\alpha\beta} = 4\pi e \frac{\mathrm{d}\mathsf{S}}{\mathrm{d}\overline{\theta}} \frac{\partial}{\partial u^{ls}_\alpha} \sum_{j,m_j} \left[\epsilon_s \epsilon^*_{p_{j,m_j}} \mathcal{M}_{j,m_j,\beta} + \text{c.c.} \right] .$$

We can write Eq. A.15 in a more compact matrix form:

$$\begin{aligned} U = & \\ & + \frac{1}{2} \mathbf{S}^\intercal \mathbf{c}^0 \mathbf{S} - \mathbf{D}^\intercal \mathbf{h}^0 \mathbf{S} + \frac{1}{2} \mathbf{D}^\intercal \boldsymbol{\beta}^\infty \mathbf{D} - \hat{\mathbf{I}}^\intercal \overline{\theta}_a \boldsymbol{\xi}^0 \mathbf{S} - \hat{\mathbf{I}}^\intercal \overline{\theta}_a \boldsymbol{\zeta}^0 \mathbf{D} \\ & + \frac{1}{NV_c} \left\{ \frac{1}{2} \mathbf{u}^\intercal \mathbf{C} \mathbf{u} - e \mathbf{u}^\intercal \mathbf{Z} \mathbf{D} + \mathbf{u}^\intercal \mathbf{G} \mathbf{S} - e \mathbf{u}^\intercal \mathbf{W} \hat{\mathbf{I}} \overline{\theta}_a \right\} , \end{aligned} \tag{A.16}$$

with bold type indicating matrix form of the tensors, and index contractions understood through tensor ordering and the transpose $^\intercal$.

We are interested in long-wavelength modes of strain $\mathbf{S}$ and electric displacement vector $\mathbf{D}$, with short-wavelength atomic displacements $\mathbf{u}$ integrated out. These "short modes"

can be integrated out by requiring that the force on each atom vanishes:

$$0 = \frac{\partial U}{\partial \mathbf{u}} \quad \Rightarrow \quad \mathbf{u} = \mathbf{C}^{-1}\left[e\mathbf{Z}\mathbf{D} - \mathbf{G}\mathbf{S} + e\mathbf{W}\hat{\mathbf{I}}\overline{\theta}_a\right]. \tag{A.17}$$

Insertion of this solution back into Eq. A.16 yields:

$$\begin{aligned} U = & \\ & + \frac{1}{2}\mathbf{S}^\intercal \mathbf{c}^D \mathbf{S} - \mathbf{D}^\intercal \mathbf{h}\mathbf{S} + \frac{1}{2}\mathbf{D}^\intercal \boldsymbol{\beta}^S \mathbf{D} - \hat{\mathbf{I}}^\intercal \overline{\theta}_a \boldsymbol{\xi}\mathbf{S} - \hat{\mathbf{I}}^\intercal \overline{\theta}_a \boldsymbol{\zeta}\mathbf{D}, \end{aligned} \tag{A.18}$$

which is identical to Eq. 3.38 in the main text, with the effective crystal tensors given by:

$$\mathbf{c}^D = \mathbf{c}^0 - \frac{\mathbf{G}^\intercal \mathbf{C}^{-1}\mathbf{G}}{NV_c}, \tag{A.19}$$

$$\boldsymbol{\beta}^S = \boldsymbol{\beta}^\infty - e^2\frac{\mathbf{Z}^\intercal \mathbf{C}^{-1}\mathbf{Z}}{NV_c}, \tag{A.20}$$

$$\mathbf{h} = \mathbf{h}^0 - e\frac{\mathbf{Z}^\intercal \mathbf{C}^{-1}\mathbf{G}}{NV_c}, \tag{A.21}$$

$$\boldsymbol{\xi} = \boldsymbol{\xi}^0 - e\frac{\mathbf{W}^\intercal \mathbf{C}^{-1}\mathbf{G}}{NV_c}, \tag{A.22}$$

$$\boldsymbol{\zeta} = \boldsymbol{\zeta}^0 + e^2\frac{\mathbf{W}^\intercal \mathbf{C}^{-1}\mathbf{Z}}{NV_c}. \tag{A.23}$$

$\boldsymbol{\xi}$ and $\boldsymbol{\zeta}$ are the piezoaxionic and electroaxionic effective tensors after integrating out the high-wavenumber modes. This procedure is analogous to the well-known correspondence for the standard crystal tensors $\mathbf{c}^D$, $\boldsymbol{\beta}^S$, and $\mathbf{h}$ to their bare counterparts $\mathbf{c}^0$, $\boldsymbol{\beta}^\infty$, and $\mathbf{h}^0$.

In much of the main text, we follow Voigt notation to describe the constitutive equations and dynamics implied by Eq. A.18, for clarity, and consistency with literature on piezoelectric crystals. The Voigt prescription reduces the order of symmetric tensors by removing repeated components; for instance, it reduces all 3×3 symmetric tensors to 6 dimensional vectors. The strain tensor is given by:

$$S_{\alpha\beta} = \begin{pmatrix} S_{xx} & S_{xy} & S_{xz} \\ S_{xy} & S_{yy} & S_{yz} \\ S_{xz} & S_{yz} & S_{zz} \end{pmatrix}, \tag{A.24}$$

and is therefore simplified to the 6-dimensional vector:

$$S_i = (S_{xx}, S_{yy}, S_{zz}, S_{yz}, S_{xz}, S_{xy}) \tag{A.25}$$

$$= (S_1, S_2, S_3, S_4, S_5, S_6), \tag{A.26}$$

such that the scalar product is preserved, i.e.:

$$\sum_{\alpha,\beta} S_{\alpha\beta} S_{\alpha\beta} = \sum_{i} S_i S_i. \tag{A.27}$$

Vectors (1-tensors) such as D_β still have 3 components, while 4-tensors and 3-tensors reduce to 6×6 and 6×3 "2-tensors" (in the Voigt convention), respectively. It is now straightforward to rewrite the constitutive Eqs. (3.40), and (3.39) in Voigt notation as Eqs. (3.42) and (3.41) in Sec. 3.1.3, for example.

A.3 Piezoelectric Equivalent Circuit Components

To separate the immittance of the piezoelectric crystal into constituent electrical components, we make use of the power series [193]:

$$\tan x = \sum_{j=1}^{\infty} \frac{8x}{(2j-1)^2\pi^2 - 4x^2}. \tag{A.28}$$

Each subsequent term in the expansion corresponds to an overtone of the mechanical resonance. In the vicinity of the fundamental resonance, we can approximate the immittance by the first term in the series. For modes whose electric field is along the direction of acoustic wave propagation, e.g. Eq. 3.56 this gives an expression for the impedance of the form:

$$Z = \frac{1}{i\omega C_c}\left(1 - k^2 \frac{8}{\pi^2 - 4(\omega\ell/2v)^2}\right). \tag{A.29}$$

Equation A.29 is equivalent to the following electrical components, arranged as in Fig. 3.3

$$C_m = \frac{8C_c k^2}{\pi^2 - 8k^2}, \tag{A.30}$$

$$L_m = \frac{\ell^2}{8C_c\, k^2 v^2}. \tag{A.31}$$

To take into account mechanical losses, we add a resistor to the circuit whose value is set by the mechanical quality factor Q_m of the crystal:

$$R_m = \frac{\pi\,\ell}{8\,C_c\,k^2\,v}\frac{1}{Q_m}. \tag{A.32}$$

We reiterate that we do not use the circuit elements of Eqs. A.30–A.32 in the analysis in the main text—we use the exact expression of Eq. 3.56 with imaginary crystal tensors. They are shown here to illustrate that near any mechanical resonance frequency, the behavior of the crystal can be accurately described by "standard" circuit elements.

In App. A.4, we include additional modes that could be used in our setup. For modes such as the whose electric field is in the perpendicular direction to the acoustic excitation, using Eq. A.28 gives an admittance of the form:

$$Y = \frac{1}{Z} = i\omega C_c \left(1 + K^2 \frac{8}{\pi^2 - 4(\omega\ell/2v)^2}\right). \tag{A.33}$$

The equivalent circuit components are given by:

$$C_m = \frac{8C_c K^2}{\pi^2}, \tag{A.34}$$

$$L_m = \frac{\ell^2}{8C_c\, K^2 v^2}, \tag{A.35}$$

$$R_m = \frac{\pi\,\ell}{8\,C_c\,K^2\,v}\frac{1}{Q_m}. \tag{A.36}$$

A.4 More Modes

In the main text (Sec. 3.2), we introduced the thickness expander mode, which is well understood and known to possess high mechanical quality factors in cryogenically cooled quartz and similar materials [126, 134]. Here we present two more modes that could be relevant for our setup. These have been constructed with the symmetry group of quartz, 32, in mind, but can be easily adapted to crystals of other symmetry groups. Much of the analysis in this appendix is based on the modes presented in [123].

First, we give an example of a length expander mode, which could be useful at low frequencies. Since the mechanical resonance frequency of this mode is set by the (longer) length dimension of a crystal bar rather than the thickness dimension of a thin plate, it could probe lower frequencies using a crystal of similar size compared to a thickness mode. The length expander mode, however, typically has a lower mechanical Q-factor than the thickness mode [128].

The second mode we include in this appendix is a thickness mode of a thin plate with a lateral electric field. Like the thickness mode in the main text, the acoustic excitations

propagate in the thickness direction of the crystal, i.e. the shortest dimension of the thin plate, but the electrodes are now placed on the minor faces so that the direction of electrical excitation is perpendicular to the thickness direction instead of parallel. This mode is less well explored experimentally but has some theoretically promising features: the axion induced voltage is integrated over the length of the plate rather than the thickness direction, which could increase the signal size by around an order of magnitude, while in principle having similar mechanical losses to the standard thickness mode. In addition, the electromechanical resonance frequency of the crystal coincides with the resonant frequency of the signal, unlike in the parallel field case where the signal frequency coincides with antiresonance, which could also improve the sensitivity of the setup and make frequency scanning simpler.

Another useful measure for comparing the potential effectiveness of different modes is the electromechanical coupling factor k, which expresses the proportion of electrical energy that can be converted into mechanical energy by the crystal, or vice versa, and can be seen as a measure of the strength of electro-elastic interactions of a given mode [123]. High coupling factors suggest a larger piezoaxionic signal due to efficient conversion of mechanical energy, and can also be seen directly from Eq. A.32 to lower the mechanical losses of the system. We will see that the new modes here have coupling factors that are comparable to the original length expander mode, which has $k \sim 0.09$ for quartz with parameters as given in [197].

We focus on longitudinal modes rather than shear modes since these develop larger quality factors at very low temperatures [129, 139]. Nevertheless, we briefly mention here that one of the most commonly used modes in quartz is the thickness shear mode, which has the largest coupling factor $k \sim 0.14$. To obtain analogous expressions for V_a, Z_{crys}, and Q for the thickness shear mode, a similar analysis to Sec. 3.2 applies if ones takes the thickness, wavenumber, and electric field to be aligned in the 2-direction ($\ell_2 \ll \ell_1, \ell_3$, $\mathbf{k} \propto \hat{\mathbf{x}}_2$, and $\mathbf{E} \propto \hat{\mathbf{x}}_2$), and the displacement in the 1-direction ($\mathbf{u} \propto \hat{\mathbf{x}}_1$). The constitutive equations then take the same form as Eqs. 3.52,3.53 with the replacements: $T_1 \to T_6$, $S_1 \to S_6$, $E_1 \to E_2$, $D_1 \to D_2$, $\hat{I}_1 \to \hat{I}_2$, $c_{11}^D \to c_{66}^D$, $h_{11} \to h_{26}$, $\beta_{11}^S \to \beta_{22}^S$, $\xi_{11} \to \xi_{62}$, and $\zeta_{11} \to \zeta_{22}$.

Length expander mode in bar with the axion-induced electric field parallel to length

Consider a narrow bar with its length along the x_1-direction, and cross-sectional dimensions that are small compared to its length: $\ell_2, \ell_3 < \ell_1$. The electrodes are placed on the faces normal to the x_1-direction. Like with the thickness modes, $D_2 = D_3 = 0$ and D_1 is spatially

uniform. Negligible cross-sectional dimensions gives only $T_1 \neq 0$. We therefore choose D and T as independent variables, which suggests using the following alternative form of the constitutive equations [123]:

$$S_1 = +s_{11}^D T_1 + g_{11} D_1 + \xi'_{11} \hat{I}_1 \overline{\theta}_a, \tag{A.37}$$

$$E_1 = -g_{11} T_1 + \beta_{11}^T D_1 - \zeta_{11}^T \hat{I}_1 \overline{\theta}_a. \tag{A.38}$$

We see that the nuclear spins should be polarized in the x_1 direction. The matrices of proportionality constants, written in terms of those contained in the internal energy of Eq. A.16, are given by:

$$\mathbf{s}^D = (\mathbf{c}^D)^{-1}, \tag{A.39}$$

$$\mathbf{g} = \mathbf{h}\,\mathbf{s}^D, \tag{A.40}$$

$$\boldsymbol{\beta}^T = \boldsymbol{\beta}^S - \mathbf{h}\,\mathbf{s}^D\,\mathbf{h}^\intercal, \tag{A.41}$$

$$\boldsymbol{\xi}' = \mathbf{s}^D\,\boldsymbol{\xi}, \tag{A.42}$$

$$\boldsymbol{\zeta}^T = \boldsymbol{\zeta} + \mathbf{h}\,\mathbf{s}^D\,\boldsymbol{\xi}; \tag{A.43}$$

where superscripts ^{T} and ^{D} denote tensors defined at constant stress or electric displacement (and superscript $^\intercal$ once again denotes a transpose).

The equation of motion for this mode is $\rho \ddot{u}_1 = \partial_1 T_1 = \partial_1^2 u_1 / s_{11}^D$. The solution to this equation that also satisfies the boundary conditions at the free surfaces $T_1 = 0$ at $x_1 = (0, \ell_1)$ is:

$$u_1 = \frac{g_{11} D_1 + \xi'_{11} \hat{I}_1 \overline{\theta}_a}{\omega / v^D} \times \left[\sin \frac{\omega x_1}{v^D} - \tan \frac{\omega \ell_1}{2 v^D} \cos \frac{\omega x_1}{v^D} \right], \tag{A.44}$$

with $v_b^D = \sqrt{\frac{1}{\rho s_{11}^D}}$ the crystal sound speed for a bar with constant-D conditions. Above, the quantities u_1, D_1, and $\hat{I}_1$ are again assumed to be oscillatory with angular frequency ω.

Rearranging the constitutive equation for the component E_1 in terms of S_1 gives:

$$E_1 = -\frac{g_{11}}{s_{11}^D} S_1 + \left(\frac{g_{11}^2}{s_{11}^D} + \beta_{11}^T \right) D_1 + \left(\frac{g_{11} \xi'_{11}}{s_{11}^D} + \zeta_{11}^T \right) \hat{I}_1 \overline{\theta}_a, \tag{A.45}$$

which can be integrated over the length of the crystal to find the voltage across the electrodes like for the thickness modes:

$$V = \int_0^{\ell_1} \mathrm{d}x_1 \, E_1 = ZI + V_a, \tag{A.46}$$

$$V_a = -\left[\frac{g_{11}\xi_{11}^{'}}{s_{11}^D}\frac{2v^D}{\omega}\tan\frac{\omega\ell_1}{2v^D} - \ell_1\left(\frac{g_{11}\xi_{11}^{'}}{s_{11}^D} + \zeta_{11}^T\right)\right]\hat{I}_1\overline{\theta}_a, \tag{A.47}$$

$$Z = \frac{1}{i\omega C_c}\left[1 - k^2\frac{2v^D}{\omega\ell_1}\tan\frac{\omega\ell_1}{2v^D}\right], \tag{A.48}$$

$$C_c = \frac{\ell_2\ell_3}{\ell_1}\left(\frac{g_{11}^2}{s_{11}^D} + \beta_{11}^T\right)^{-1}, \tag{A.49}$$

$$k = \frac{g_{11}}{\sqrt{g_{11}^2 + \beta_{11}^T s_{11}^D}}. \tag{A.50}$$

For quartz, the coupling factor k of this mode is ~ 0.10, which is comparable to the thickness expander mode in the main text.

Thickness expander mode with axion-induced electric field perpendicular to thickness

Like in Sec. 3.2, we will again take the piezoelectric crystal to be a rectangular prism with side lengths ℓ_i of high aspect ratio (thin plate): $\ell_2 \ll \ell_1, \ell_3$. Notice this time we have oriented the crystal slightly differently, with l_2 rather than l_1 being the thickness dimension. The faces with electrodes are normal to the x_1-direction, which leads to the boundary condition that on the faces with electrodes $E_2 = E_3 = 0$. The surfaces with electrodes are also equipotential surfaces, meaning that E_1 is independent of x_2, i.e. $\partial E_1/\partial x_2 = 0$ The plate is considered to be laterally clamped, so that only $S_2 \neq 0$, with the other 5 strains vanishing identically. On the free surfaces at $x_2 = (0, l_2)$, the stress $T_2 = 0$. These conditions suggest that the independent variables are chosen to be S and E, which leads to the constitutive equations:

$$T_2 = +c_{22}^E S_2 - e_{12}E_1 - \xi_{21}^E\hat{I}_1\overline{\theta}_a, \tag{A.51}$$

$$D_1 = +e_{12}S_2 + \epsilon_{11}^S E_1 - \zeta_{11}^{'}\hat{I}_1\overline{\theta}_a. \tag{A.52}$$

The nuclear spins are polarized in the x_1 direction. The Voigt matrices of proportionality constants are given by:

$$\mathbf{c}^E = \mathbf{c}^D - \mathbf{h}^\intercal \boldsymbol{\epsilon}^S \mathbf{h}, \tag{A.53}$$

$$\boldsymbol{\epsilon}^S = (\boldsymbol{\beta}^S)^{-1}, \tag{A.54}$$

$$\mathbf{e} = \boldsymbol{\epsilon}^S \mathbf{h}, \tag{A.55}$$

$$\boldsymbol{\xi}^E = \boldsymbol{\xi} + \mathbf{h}^\intercal \boldsymbol{\epsilon}^S \boldsymbol{\zeta}, \tag{A.56}$$

$$\boldsymbol{\zeta'} = \boldsymbol{\epsilon}^S \boldsymbol{\zeta}. \tag{A.57}$$

The wave equation for this mode is $\rho \ddot{u}_2 = \partial_2 T_2 = c_{22}\, \partial_2^2 u_2$. As usual, we take harmonic factors to be implicit. The solution to the wave equation that satisfies the boundary conditions listed above is given by

$$u_2 = \frac{e_{12} E_1 + \xi_{21}^E \hat{I}_1 \overline{\theta}_a}{c_{22}^E \omega / v^E} \times \left[\sin \frac{\omega x_2}{v^E} - \tan \frac{\omega \ell_2}{2 v^E} \cos \frac{\omega x_2}{v^E} \right], \tag{A.58}$$

with $v^E = \sqrt{\frac{c_{22}^E}{\rho}}$ the crystal sound speed for a bar with constant-E conditions.

We can now find the current in the piezoelectric by integrating the time derivative of the electric displacement over its thickness:

$$I = \ell_3 \int_0^{\ell_2} \dot{D}_1 \, \mathrm{d}x_2, \tag{A.59}$$

while the voltage across the electrodes is given by the integral over its length:

$$V = \int_0^{\ell_1} E_1 \, \mathrm{d}x_1, \tag{A.60}$$

this gives the results:

$$I = \frac{V}{Z} + I_a, \tag{A.61}$$

$$I_a = i\omega\ell_3 \left[\frac{e_{12}\,\xi^E_{21}}{c^E_{22}} \frac{2v^E}{\omega} \tan\frac{\omega\, l_2}{2v^E} - \zeta'_{11} l_2 \right] \hat{I}_1 \overline{\theta}_a, \tag{A.62}$$

$$\frac{1}{Z} = i\omega C_c \left[1 + k^2 \frac{2v^E}{\omega\ell_2} \tan\frac{\omega\ell_2}{2v^E} \right], \tag{A.63}$$

$$C_c = \frac{\ell_2\ell_3}{\ell_1} \varepsilon^S_{11}, \tag{A.64}$$

$$k = \frac{e_{12}}{\sqrt{c^E_{22}\epsilon^S_{11}}}; \tag{A.65}$$

where we see that the axion signal enters as a current source in parallel with the crystal. The coupling factor k in quartz is almost identical to the other thickness expander mode, with both having $k \sim 0.09$ for quartz parameters. Converting to an equivalent voltage source gives:

$$\begin{aligned} V_a = I_a Z = \frac{\ell_1}{\epsilon^S_{11}} \left\{ 1 + k^2 \frac{2v^E}{\omega\ell_2} \tan\frac{\omega\,\ell_2}{2v^E} \right\}^{-1} \\ \times \left[\frac{e_{12}\,\xi^E_{21}}{c^E_{22}} \frac{2v^E}{\omega\ell_2} \tan\frac{\omega\,\ell_2}{2v^E} - \zeta'_{11} \right] \hat{I}_1 \overline{\theta}_a. \end{aligned} \tag{A.66}$$

At the mechanical resonance frequency of the plate, $f = \frac{2v^E}{l_2}$, the admittance $1/Z$ diverges, implying that the plate is also at electromechanical resonance (assuming it is not yet loaded by external electrical components). The equivalent circuit components can be found using Eqs. A.34, A.35 and A.36.

The additional modes presented in this appendix suggest that by changing the orientation of the crystal, the direction of nuclear spin polarization and the placement of electrodes, one could improve the frequency range and sensitivity of the experiment when subject to limitations in number of crystals and their size. A full optimization analysis including a larger variety of crystal modes such as these will be left to future work.

Appendix B

Appendices for the Piezoaxionic Force

B.1 MQM and Rotational Invariance

The MQM of a nucleus is proportional to the tensor:

$$t_{fg} = \frac{1}{4I\,(2I-1)}\left[I_f I_g + I_g I_f - \frac{2}{3}\delta_{fg} I(I+1)\right] \tag{B.1}$$

Where I of any general dimension is given by:

$$(I_x)_{ab} = \frac{\hbar}{2}\left(\delta_{a,b+1} + \delta_{a+1,b}\right)\sqrt{(I+1)(a+b-1) - ab} \tag{B.2}$$

$$(I_y)_{ab} = \frac{i\,\hbar}{2}\left(\delta_{a,b+1} - \delta_{a+1,b}\right)\sqrt{(I+1)(a+b-1) - ab} \tag{B.3}$$

$$(I_z)_{ab} = \hbar(I+1-a)\delta_{a,b} \tag{B.4}$$

For an ensemble of spins:

$$\langle t_{fg}\rangle = \mathrm{tr}(\rho\, t_{fg}) = \rho_{ab}(t_{fg})_{ba} \tag{B.5}$$

where ρ is the density matrix describing the ensemble of nuclear spins. When the spins are unpolarized, the density matrix is given by:

$$\rho_{ab} = \delta_{ab}\frac{1}{2I+1} \tag{B.6}$$

so we find

$$\langle t_{fg} \rangle = \frac{1}{2I+1}(t_{fg})_{aa} \tag{B.7}$$

By rotational symmetry, we can see immediately that $\langle t_{fg} \rangle = 0$ for $f \neq g$. We will now examine the diagonal elements $f = g$. Using eq. B.4:

$$(I_z)_{ab}(I_z)_{ba} = \sum_{a=1}^{2I+1}(I+1-a)^2 \tag{B.8}$$

so we find

$$\langle I_z\, I_z \rangle = \frac{I(I+1)}{3} = \langle I_x\, I_x \rangle = \langle I_y\, I_y \rangle \tag{B.9}$$

where the second and third equalities follow from rotational invariance. We can then see for diagonal elements, $\langle t_{fg} \rangle = 0$ once again. This suggests that we need a breaking of rotational invariance in the ground state of our nuclei, which will be supplied by polarizing the nuclear spins.

B.2 Nuclear Spin Polarization Via Hyperfine Interactions

Nuclear spin polarization in equilibrium at temperature T and an external magnetic field $\mathbf{B}_0$:

$$\langle \hat{\mathbf{I}} \rangle = \hat{\mathbf{B}}_0 \tanh\left[\frac{\mu B_0}{T}\right]. \tag{B.10}$$

For $\mu = \mu_N$ (nuclear magneton), $B_0 = 10\,\mathrm{T}$, and $T = 10\,\mathrm{mK}$, we have $\mu B_0/T \approx 0.366$. In a magnetic material with polarizable electron spins, however, the effective magnetic field at the nucleus may be increased due to hyperfine interactions, allowing for $\mathcal{O}(1)$ nuclear polarization at higher temperatures, i.e. $\langle H_{hf} \rangle = -\mu \cdot \mathbf{B}_{int}$, where

$$\begin{aligned}\langle \alpha\, J\, I\, F\, M | H_{hf} | \alpha'\, J\, I\, F\, M \rangle &= \frac{1}{2} A\, K \\ &+ B \frac{\frac{3}{4}K(K+1) - I(I+1)J(J+1)}{I(2I-1)J(2J-1)}\end{aligned} \tag{B.11}$$

$$K = F(F+1) - J(J+1) - I(I+1) \tag{B.12}$$

and $\mathbf{J} = \mathbf{L} + \mathbf{S}$ is electron angular momentum, $\mathbf{F} = \mathbf{I} + \mathbf{J}$ is the total angular momentum of the atom, A is the magnetic hyperfine structure constant, and B is the electric quadupole constant.

For the isotope Eu-153, the expected hyperfine energy splittings are of the order of $\Delta E_{hf} \approx 10^{-6}$eV for the first excited $^6P_{5/2}$ state, corresponding to a temperature of 0.01K [181]. For Np-237, $\Delta E_{hf} \approx 10^{-5}$eV, meaning that temperatures as high as 0.1eV should suffice for $\mathcal{O}(1)$ nuclear spin polarizations [180].

For Np-237, this higher temperature has the added advantage that it is at the threshold temperature before which the setup will become too heated by the radiation emitted. A dilution refrigerator's cooling power depends on the target temperature T and the ^3He flow rate $\dot{n}$ [151]:

$$\dot{Q} \approx 8.4\,\mu\text{W} \left(\frac{\dot{n}}{10^{-3}\,\text{mol/s}}\right)\left(\frac{T}{10\,\text{mK}}\right)^2. \tag{B.13}$$

The decay heating power of $^{235}_{92}U$ is approximately $60\,\mu$W/kg [150] and for $^{237}_{93}Np$ is 0.02 W/kg. For the maximum volume of material considered here, $(300mm)^2 \times 0.5cm$, this limits the two materials listed here containing $^{237}_{93}Np$, with densities around $6.5g/cm^3$, to a minimum temperature of around $0.1K$.

B.3 Magnetic Quadrupole Moment Matrix Elements

The derivation of the MQM operator is detailed in references [169, 183]. The coefficient of the MQM operator in eq. 4.14 is given explicitly by:

$$\mathcal{C}_j = \frac{96(\kappa_1+\kappa_2-2)\text{sgn}(\kappa_1)\text{sgn}(\kappa_2)(\sin(\pi(\gamma_1-\gamma_2)))}{\pi\prod_{i=-2}^{2}((\gamma_1-\gamma_2-i)(\gamma_1-\gamma_2+i))} \tag{B.14}$$

$$\gamma = \sqrt{(j+1/2)^2 - Z^2\alpha^2} \tag{B.15}$$

$$\kappa = (l-j)(2j-1) \tag{B.16}$$

where j, l and total and orbital angular momentum respectively, and the indices $1, 2$ refer to the two states in the matrix element of eq. 4.14. The individual matrix elements of $\langle\Omega_{p_{3/2,m_j}}|\sigma_m\hat{r}_k + \sigma_k\hat{r}_m - 2(\boldsymbol{\sigma}\cdot\hat{\boldsymbol{r}})\hat{r}_k\hat{r}_m|\Omega_{s_{1/2}}\rangle$ are:
$m_{j,s} = +1/2, m_{j,p} = +3/2$:

$$\begin{pmatrix} 0 & 0 & -\frac{\sqrt{\frac{3}{2}}}{5} \\ 0 & 0 & -\frac{1}{5}i\sqrt{\frac{3}{2}} \\ -\frac{\sqrt{\frac{3}{2}}}{5} & -\frac{1}{5}i\sqrt{\frac{3}{2}} & 0 \end{pmatrix} \tag{B.17}$$

$m_{j,s} = +1/2, m_{j,p} = +1/2$:

$$\begin{pmatrix} -\frac{\sqrt{2}}{5} & 0 & 0 \\ 0 & -\frac{\sqrt{2}}{5} & 0 \\ 0 & 0 & \frac{2\sqrt{2}}{5} \end{pmatrix} \tag{B.18}$$

$m_{j,s} = +1/2, m_{j,p} = -1/2$:

$$\begin{pmatrix} 0 & 0 & \frac{3}{5\sqrt{2}} \\ 0 & 0 & -\frac{3i}{5\sqrt{2}} \\ \frac{3}{5\sqrt{2}} & -\frac{3i}{5\sqrt{2}} & 0 \end{pmatrix} \tag{B.19}$$

$m_{j,s} = +1/2, m_{j,p} = -3/2$:

$$\begin{pmatrix} \frac{\sqrt{6}}{5} & -\frac{1}{5}\left(i\sqrt{6}\right) & 0 \\ -\frac{1}{5}\left(i\sqrt{6}\right) & -\frac{\sqrt{6}}{5} & 0 \\ 0 & 0 & 0 \end{pmatrix} \tag{B.20}$$

$m_{j,s} = -1/2, m_{j,p} = +3/2$:

$$\begin{pmatrix} -\frac{\sqrt{6}}{5} & -\frac{1}{5}\left(i\sqrt{6}\right) & 0 \\ -\frac{1}{5}\left(i\sqrt{6}\right) & \frac{\sqrt{6}}{5} & 0 \\ 0 & 0 & 0 \end{pmatrix} \tag{B.21}$$

$m_{j,s} = -1/2, m_{j,p} = +1/2$:

$$\begin{pmatrix} 0 & 0 & \frac{3}{5\sqrt{2}} \\ 0 & 0 & \frac{3i}{5\sqrt{2}} \\ \frac{3}{5\sqrt{2}} & \frac{3i}{5\sqrt{2}} & 0 \end{pmatrix} \tag{B.22}$$

$m_{j,s} = -1/2, m_{j,p} = -1/2$:

$$\begin{pmatrix} \frac{\sqrt{2}}{5} & 0 & 0 \\ 0 & \frac{\sqrt{2}}{5} & 0 \\ 0 & 0 & -\frac{1}{5}\left(2\sqrt{2}\right) \end{pmatrix} \tag{B.23}$$

$m_{j,s} = -1/2, m_{j,p} = -3/2$:

$$\begin{pmatrix} 0 & 0 & -\frac{\sqrt{\frac{3}{2}}}{5} \\ 0 & 0 & \frac{1}{5}i\sqrt{\frac{3}{2}} \\ -\frac{\sqrt{\frac{3}{2}}}{5} & \frac{1}{5}i\sqrt{\frac{3}{2}} & 0 \end{pmatrix} \tag{B.24}$$